AD-752 231

PROTOTYPE MOVING BASE GRAVITY GRADIOMETER

Charles B. Ames, et al

Hughes Research Laboratory

Prepared for:

Air Force Cambridge Research Laboratories
Advanced Research Projects Agency

August 1972

DISCLAIMER NOTICE

THIS DOCUMENT IS THE BEST QUALITY AVAILABLE.

COPY FURNISHED CONTAINED A SIGNIFICANT NUMBER OF PAGES WHICH DO NOT REPRODUCE LEGIBLY.

PROTOTYPE MOVING BASE GRAVITY GRADIOMETER

C. B. AMES, R. L. FORWARD, P. M. LA HUE,
R. W. PETERSON, A. J. ROBINSON, and D. W. ROUSE

HUGHES RESEARCH LABORATORIES
3011 MALIBU CANYON ROAD
MALIBU, CALIFORNIA 90265

SEMIANNUAL TECHNICAL REPORT 1
CONTRACT F19628-72-C-0222
PROJECT CODE P1F10

AUGUST 1972

CONTRACT MONITOR: BELA SZABO
TERRESTRIAL SCIENCES LABORATORY

Approved for public release;
distribution unlimited.

Sponsored by
ADVANCED RESEARCH PROJECTS AGENCY
ARPA ORDER 1838

Monitored by
AIR FORCE CAMBRIDGE RESEARCH LABORATORIES
AIR FORCE SYSTEMS COMMAND
UNITED STATES AIR FORCE
BEDFORD, MASSACHUSETTS 01730

DOCUMENT CONTROL DATA - R&D

(Security classification of title, body of abstract and indexing annotation must be entered when the overall report is classified)

1. ORIGINATING ACTIVITY *(Corporate author)*
Hughes Research Laboratories
3011 Malibu Canyon Road
Malibu, CA 90265

2a. REPORT SECURITY CLASSIFICATION
Unclassified

2b. GROUP
N/A

3. REPORT TITLE
PROTOTYPE MOVING BASE GRAVITY GRADIOMETER

4. DESCRIPTIVE NOTES *(Type of report and inclusive dates)*
Scientific Interim

5. AUTHOR(S) *(First name, middle initial, last name)*
Charles B. Ames, Robert L. Forward, Philip M. LaHue, Robert W. Peterson, Adrian J. Robinson, and David W. Rouse

6. REPORT DATE
August 1972

7a. TOTAL NO. OF PAGES
~~192~~ 194

7b. NO. OF REFS
8

8a. CONTRACT OR GRANT NO.
F19628-72-C-0222

b. PROJECT, TASK, WORK UNIT NOS.
1838-00 n/a

c. DOD ELEMENT
62701D

d. DOD SUBELEMENT
n/a

Details of illustrations in this document may be better studied on microfiche.

9a. ORIGINATOR'S REPORT NUMBER(S)
Semiannual Technical Report 1

9b. OTHER REPORT NO(S) *(Any other numbers that may be assigned this report)*
AFCRL-72-0535

10. DISTRIBUTION STATEMENT
Approved for public release; distribution unlimited.

11. SUPPLEMENTARY NOTES
This research was supported by the Defense Advanced Research Projects Agency.

12. SPONSORING MILITARY ACTIVITY
Air Force Cambridge Research Laboratories (LW)
L.G. Hanscom Field
Bedford, Massachusetts 01730

13. ABSTRACT

This report covers the technical studies accomplished during the first six months of this contract to design and develop a prototype moving base gravity gradiometer. The scope of work is limited to establishing the instrument and system design parameters during the time period covered by this report. Thus, this report presents analytical and theoretical studies. Almost no laboratory experiments have been conducted with the Hughes hard hearing sensor during this reporting period.

Because of the complex and interactive nature of the many tasks required, and because this report covers a specific time span, it is necessary to regard many of the findings as tentative, thus they are open to revision as the study proceeds.

The study has resulted in an evolution of the sensor baseline configuration from that postulated in September 1971. This report presents preliminary designs, and summarizes advantages and disadvantages for three sensor vibration isolation concepts: (1) rotating floated spherical sensor, (2) two-axis mechanical gimbal ring sensor mount, and (3) two axis air pad gimbal mount. A summary of tentative sensor parameters is presented.

The report presents in detail, a system error budget that indicates errors reflected at the individual sensor output as well as at the individual gradient tensor element. Derivations of sensor error mechanisms are presented. Errors due to rotational field effects, arm mass unbalance and magnetic field interactions are derived. Design concepts and parameters for the various subsystems are presented. Sensor arm mass and inertia balance are discussed as are estimates for the sensor translational and angular vibration environment.

The spin bearing performance characteristics, error mechanism and requirements are presented. Lastly, efforts to find and select suitable materials are documented.

DD FORM 1 NOV 65 1473

I-A

14. KEY WORDS	LINK A		LINK B		LINK C	
	ROLE	WT	ROLE	WT	ROLE	WT
Gravity gradiometer						
Gravitational mass sensor						
Gravitational gradient sensor						
Gravity mapping						
Mass detection						
Navigation						
Inertial guidance						
Airborne gradiometer						
Vertical deflection						
Motion isolation and stabilization						

AFCRL-72-0535

PROTOTYPE MOVING BASE GRAVITY GRADIOMETER

by

Charles B. Ames
Robert L. Forward
Philip M. LaHue
Robert W. Peterson
Adrian J. Robinson
David W. Rouse

HUGHES RESEARCH LABORATORIES
a division of hughes aircraft company
Malibu, California 90265

Contract F19628-72-C-0222
Project 1838
Task 183800

Semiannual Technical Report

August 1972

Contract Monitor: Bela Szabo
Terrestrial Sciences Laboratory

Approved for public release; distribution unlimited.

Sponsored by
Advanced Research Projects Agency
ARPA Order 1838

Monitored by
Air Force Cambridge Research Laboratories
Air Force Systems Command
United States Air Force
Bedford, Massachusetts 01730

I-C

ARPA Order No. 1838

Program Code No. 1F10

Contractor: Hughes Aircraft Company

Effective Date of Contract: 1 Feb. 1972

Contract No. F19628-72-C-0222

Principal Investigator and Phone No.
Dr. Robert L. Forward, (213)456-6411

AFCRL Project Scientist and Phone No.
Mr. Bela Szabo, (617)861-3654

Contract Expiration Date: 31 January 1974

TABLE OF CONTENTS

I INTRODUCTION 1

II SUMMARY 3

III TECHNICAL FINDINGS AND ACCOMPLISHMENTS 7

A. Error Budget 7

1. Outline For RGG System Error Budget 7

2. RGG Coordinate Definitions 17

B. Error Mechanism Derivations 21

1. Thermal Noise Fluctuations in the Rotating Gravity Gradiometer 22

2. Covariance Functions of the Rotational Field Errors of the RGG 38

3. RGG Errors Due to Transverse Differential Arm Mass Unbalance 47

4. RGG Errors Due to Paramagnetic Materials 56

C. Design Concepts and Parameters 67

1. Selection of ω_o and Q For the RGG 68

2. RGG Sensor Electronics 85

3. Sensor Arm Mass-Unbalance and Inertia-Unbalance Mechanical Adjustment 91

4. Vibrational Motion Environment Estimates 102

5. Preliminary Gradiometer Designs 109

6. Isoelasticity of Spherical Gimbal Support with Hydrostatic Bearing Pads 129

7. Spin Bearing Requirements 135

a. Gradient Errors Due to Sum-Mode Mismatch 136

b. Torque Variation With Eccentricity in Fluid Journal Bearings 142

c. Phase Errors Due to Spin Bearing Disturbance Torques 146

d. Spin Bearing Procurement Specification 149

8. RGG Baseline Parameters 165

D. Materials Selection 168

1. Material Characteristics (Preliminary) 169

2. Paramagnetic and Diamagnetic Material Tests 184

REFERENCES 189

LIST OF ILLUSTRATIONS

FIGURE		PAGE
1	System Breakdown Structure	8
2	Signal Processing Model Block Diagram	25
3	Rotating Gravity Gradiometer Simplified Model	26
4	Signal Process Model With $n_T(t)$ as Input Torque Noise Spectrum	30
5(a)	Torque Noise Spectrum	32
5(b)	Carrier Filter Output Spectrum	32
5(c)	Demodulator Output Spectrum	32
6	Spectrum of Eq. (16)	53
7	Spectrum Shift Due to Demodulation Processes	53
8	Narrowed Bandwidth	53
9	Electronic Circuit Schematic Diagram	86
10	Acceleration-Power Spectra	106
11	Angular Rate Power Spectrum	107
12	Configuration "A"	121
13	Configuration "B"	122
14	Configuration "C"	126
15	Anelastic-Elastic Limit	174

SECTION I

INTRODUCTION

This report covers the primary technical work completed during the first six months of the subject contract to design and develop a prototype moving base gravity gradiometer. The scope of work during this time period, and for the remaining time during Phase One, is limited to establishing the instrument and system design parameters. As such the nature of this work is restricted primarily to analytical and theoretical studies. The Phase One conclusions will be documented in the R&D Design Evaluation Report and presented at a Design Review.

This first six months has seen many positive accomplishments. The most significant findings are documented on the following pages of this report. Because of the complex and interactive nature of the many tasks required under this contract, and because this report covers a specific time span, it is necessary to regard some of the findings as being less than absolute, thus open to revision as the Phase One study proceeds. The progress has been in general accordance with the original management and technical plan. The only significant deviation from the September 1971 Proposal has been in the mix between analytical and laboratory work; there have been almost no laboratory experiments conducted with the original hard-bearing sensor during this reporting period. This decision results from desires expressed by the AFCRL Contract Monitor and from a reestablishment of task priorities due to funding, personnel and time limitations.

Significant technical progress and accomplishments toward finalization of the design of a prototype moving base rotating gravity gradiometer (RGG) have been achieved, most of which are documented on the following pages.

SECTION II

SUMMARY

During the first six months of work under the contract, HRL has conducted analyses, studies, and originated several preliminary designs. There has been an evolution of baseline sensor configurations beginning with the spherical floated sensor concept presented in our September 1971 proposal. We have conducted individual error analyses and have started on a comprehensive error budget. We have selected many of the basic design parameters for the subsystems of the gradient tensor sensing system. The principal technical findings and accomplishments are described briefly in this summary. Detailed discussions of each topic follow in the body of this report (Section III), entitled "Technical Findings and Accomplishments."

Section III-A presents a complete, consistent and organized system error budget, including a listing of all known error excitation sources and error mechanisms. This detail is necessary for a system as complex and difficult as the moving base gravity gradiometer. This section provides a tabular format which indicates errors reflected at the individual sensor output as well as at the individual gradient tensor element. Due to the comprehensive nature of this task, the table is not yet completed, however many errors of individual subsystems have been estimated and appear in other sections of this report. In addition, Section III-A2 presents RGG coordinate definitions which will be adopted for all system error analyses, budgeting and system design.

Derivations of particular sensor error mechanisms are presented in Section III-B. The thermal noise derivation (III-B1) corrects an error in our previously reported work. The new thermal noise analysis has a direct impact on the basic sensor arm size requirement. Our previous analysis indicated for a sufficiently small thermal noise contribution (1/3 E.U.), that a sensor arm inertia of 18,600 gm-cm^2 was required. The corrected result indicates a requirement of

35,610 gm-cm^2. Assuming similar arm geometry and material densities, this reflects in an arm size increase of 13.8 percent.

A derivation of the errors due to rotational field effects (III-B2) illustrates the importance of considering correlations between angular rate about orthogonal axes. This results in adding considerable complexity in computation of estimates of errors caused by sensor case angular disturbances.

Errors due to arm mass-unbalance are derived (III-B3) as well as the sensor error sensitivity caused by interaction of the Earth's magnetic field with paramagnetic materials in the sensor arms (III-B4).

Design concepts and parameters for the various subsystems are presented in Section III-C. First is a description of the rationale used to select the nominal design values for the sensor resonant frequency (ω_o) and mechanical amplification at resonance (Q) (III-C1). Selection of these basic sensor parameters along with a thermal noise design limit of 1/3 E.U. also defines the minimum sensor arm inertia, hence its minimum size. With the above selection of basic sensor design parameters completed, many parameters of the other subsystems are then bounded. For example, the design requirements of the RGG electronic circuits presented in the next section (III-C2) were heavily influenced by the basic sensor parameter selection.

The next section (III-C3) is a discussion of the sensor arm mass and inertia balance problem. Values of arm mass and moment of inertia balance which are felt to be practically achievable in the laboratory and maintainable in operational usages are shown. The change of balance resulting from the sensor being spun-up are estimated and it is shown that these changes are within the balance adjustment range of our proposed mercury balance tubes. The resultant sensor mass unbalance error sensitivity to vibrations at one and three-times spin frequency is shown to produce errors sufficiently below the required error budget limit for the anticipated sensor vibration environment.

Estimates for the sensor translational and angular vibration environment are discussed in the next section (III-C4). These estimates assume the carrying vehicle to be a KC-135 aircraft operated during times when the flight condition is no more severe than a "mild

turbulence" condition. Vibration power spectral densities are estimated for the aircraft, the base of the inertial platform, and the stable element of the inertial platform. To generate these estimates, preliminary performance parameters of both the vibration isolation mount and the inertial platform were needed. To determine the performance parameters of each of these subsystems, some preliminary design concepts for each subsystem were generated. Results of the vibration estimates reveal that the translational vibration environment of the stable element of the inertial platform is sufficiently small such that, with the arm mass balance capability we expect to achieve, the system performance goal can easily be met. The results also indicate that if the sensor were hard-mounted to the platform stable element, the rotational field error would be approximately 2-1/2 EU, one sigma. Since 2-1/2 EU exceeds our budgeted allocation for this error, two alternatives can be considered. One alternative is to add an additional stage of angular isolation between the platform's stable element and the sensor. Several sensor angular isolation support systems have been considered and some preliminary designs are presented in Section III-C5. The second alternative is to reduce the angular vibration levels of the platform stable element. The primary cause of the 2-1/2 EU error is due to the assumed platform gimbal bearing friction. The friction level was based on the use of conventional ball-type platform gimbal bearings. One method of reducing this friction level would be to use hydrostatic air bearings instead of ball bearings.

In the next section (III-C5) preliminary designs are shown for each of the following sensor angular vibration isolation concepts:

1. Rotating floated spherical sensor.
2. Two axis mechanical gimbal ring sensor mount.
3. Two axis air pad gimbal mount.

The basic sensor size shown for each of these preliminary design sketches was approximately the same. The comparison table, contained in this section, summarizes the advantages and disadvantages

of each concept. System No. 3 above, appears the most favorable of the three at this time. Section III-C6 presents a proof that only four air gimbal pads, located at the intersection of the corners of a circumscribed equilateral tetrahedron, provide an isoelastic suspension system.

Section III-C7 deals with the characteristics, requirements, and error mechanisms which affect the sensor spin-bearing performance. Included is the current spin-bearing procurement specification. Most of these analyses are equally applicable in bounding the rotor spin motor and its servo loop performance.

The last topic of Section C (III-C8) is a summary of the presently conceived RGG baseline sensor parameters. The values shown are not necessarily final firm values but large deviations are not expected during the remaining Phase I design effort.

Section D summarizes our efforts in finding and selecting suitable materials for constructing the gradiometer. Because of the dual requirements for use of materials which are both highly mechanically stable and highly non-magnetic, considerable effort was required to discover and locate sources of supply for some of these materials. It is important to note that many materials usually considered to be non-magnetic have completely intolerable magnetic permeabilities for this application.

These technical findings and accomplishments cover the work that has been completed on the moving base RGG to this date. A number of similar studies and designs are in progress and their results will be included in the final report on Phase I.

SECTION III

TECHNICAL FINDINGS AND ACCOMPLISHMENTS

The following sections treat various aspects of the moving base rotating gravity gradiometer design problem. Appropriate sections are generally grouped together, but due to the complexity and interrelations of the problems, some sections discuss several subjects.

A. ERROR BUDGET

1. Outline for RGG System Error Budget

2. RGG Coordinate Definitions

These sections provide a coordinated and systematic approach to the RGG error analysis and error budget.

1. Outline for RGG System Error Budget

This section presents an outline and format for the RGG System Error Budget. It was prepared both to aid in organizing the error analysis and to illustrate an orderly method of presenting the results.

The error budget is organized by hardware element; i. e., it groups error contributions by hardware element. This grouping was chosen — as opposed to grouping by error type, error excitation source, or error mechanism — so that performance requirements for any given hardware element can easily be gleaned from the summary table.

Figure 1 illustrates the system breakdown structure for a typical operational gradient tensor measuring system. It consists of four major systems:

- Vibration Isolation, Alignment and Leveling System (VIALS). This system, consisting of two major subsystems, provides a certain amount of translational vibration isolation, serves as an attitude reference and attenuates angular rate inputs to the gradiometers.

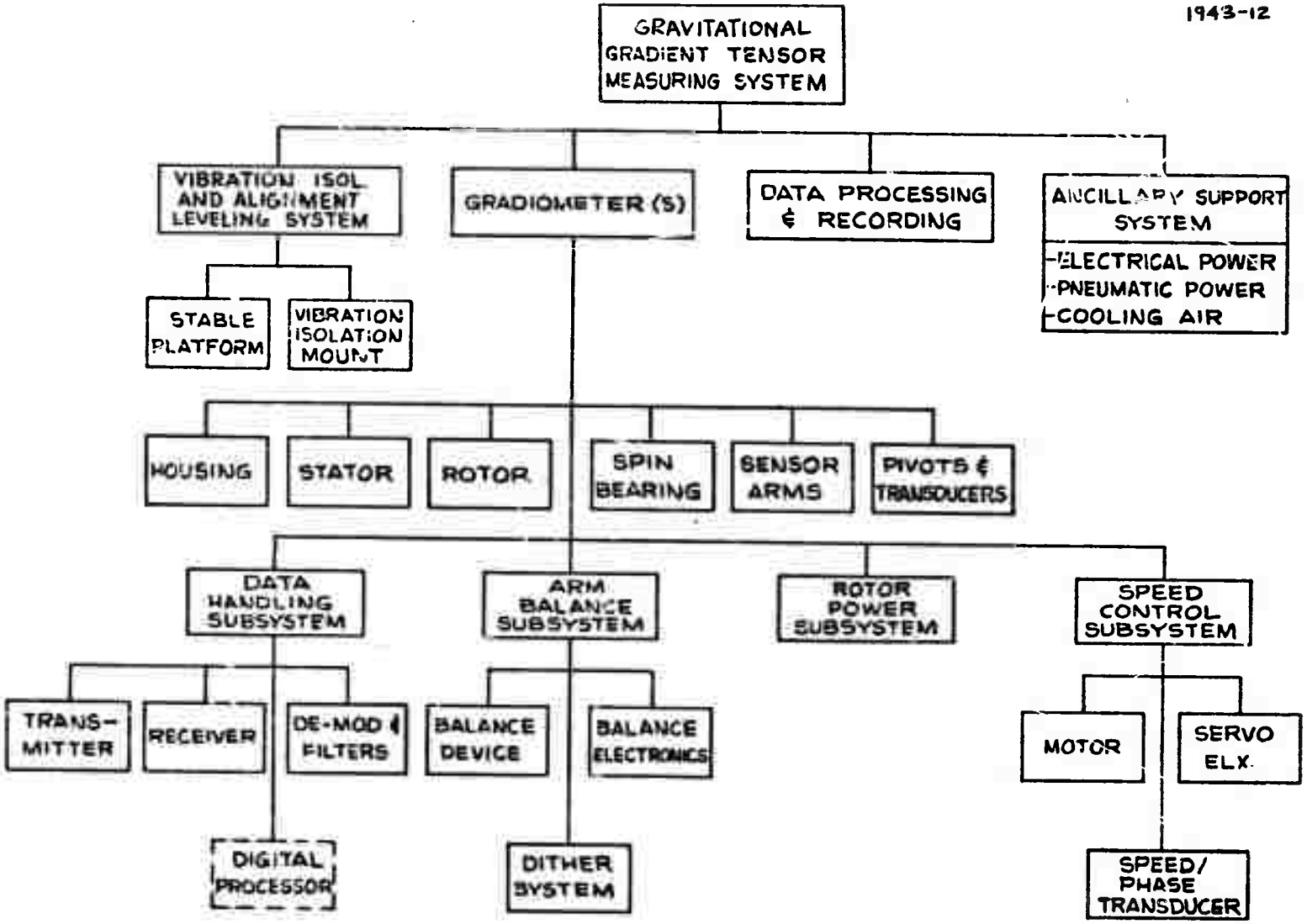

Fig. 1. System Breakdown Structure.

- Gradiometer(s). This system is comprised of three identical rotating gravity gradiometers. The hardware elements comprising each gradiometer are detailed in the figure and the term "gradiometer" as used here is intended to include all of the hardware elements to be developed under the AFCRL RGG contract. The output of the gradiometer will consist of the demodulated and filtered, in-phase (I), and quadrature-phase (Q) sensor signals in digital form.

- Data Processing and Recording System. This system can only be defined after a specific application is selected. Typically, it would consist of a digital central processor, I/O, and recording system. Its functions would include combining the outputs of the three gradiometers to form the gradient tensor elements, compensating for mass proximity effects, performing coordinate rotations of the gradient tensor, computing deflection of the vertical, recording gradient data, etc. We are planning to study the data smoothing and combining of the three gradiometer outputs during Phase II.

- Ancillary Support System. This system will consist of electrical and pneumatic power supplies, special air conditioning equipment and the like necessary to support the rest of the systems.

a. Summary Table Explanation

The proposed method of presenting the error analysis is illustrated in Table I, "RGG System Error Summary." Explanation of the table is as follows. A single error process is represented by one horizontal line entry in the table. As an example of one error process, for the specified contributing subsystem (e.g., spin bearing) the error excitation source (e.g., translational vibration at spin frequency) acts thru the error mechanism (e.g., spin bearing variation in torque with load acts thru sum-mode mismatch) to produce an error. This error is then classified as to error type (e.g., a bias shift). Each error process is evaluated for either a vertical or horizontal spin-axis sensor orientation and the error in amplitude and/or phase at the gradiometer output is evaluated. Further, the reflection of this error process at the appropriate tensor element(s) is also evaluated.

The following sections list in detail the specific error types, error excitation sources, and error mechanisms.

Table I. RGG System Error Summary

CONTRIBUTING SUBSYSTEM	EXCITATION SOURCE		ERROR MECHANISM		ERROR TYPE	ERROR AT SENSOR OUTPUT				ERROR AT TENSOR ELEMENT			
	TYPE	MAGNITUDE	DESCRIPTION	DESIGN VALUE		HORIZ. S.A.		VERTICAL S.A.		DIAGONAL		OFF-DIAGONAL	
						AMPL. E.U.	PHASE DEG.	AMPL. E.U.	PHASE DEG.	Γ_{xx} or Γ_{yy} E.U.	Γ_{zz} E.U.	Γ_{xy} E.U	Γ_{xz} or Γ_{yz} E.U

T723

b. Error Types

We are concerned with the following types of error as they affect the accuracy of measurement of each of the elements of the mass attraction gravity gradient tensor:

- Initial Bias (compensatable)
- Shift of Bias from Initial Value (uncompensatable)
- Noise (i.e., random variation about bias)
- Scale Factor Stability
- Scale Factor Linearity

Both of these to include resultant effect in output in the presence of the Earth's nominal gravity gradients.

c. Error Excitation Sources

The following fifteen excitation sources hopefully represent all of those sources which can possibly cause errors in gradient tensor output:

(1) Translational Acceleration

- Steady DC
- Transient changes in DC
- Vibration (initial or changes from initial levels)
- Self-induced vibration

(2) Angular Rates and Accelerations

- Steady DC
- Transient changes in DC
- Vibration and changes from those existing at time of calibration
- Self-induced vibration

(3) Temperature – (Nominal operating temperature results in thermal noise effects)

(4) Temperature Variation

(5) Ambient Pressure

(6) Ambient Humidity

(7) Magnetic Fields

(8) Electric Fields

(9) Acoustic Disturbance

(10) Angular Orientation

(11) Mass Proximity Noise

(12) Prime Power Variations

(13) Time Standard Variations

(14) Component Inherent Characteristics

(15) Material Stability – This will include stability of dimensional properties as well as other parameter changes (e.g., transistor β's, Youngs modulus, damping coefficient, etc.) resulting from creep, aging, crystal growth, temperature cycling, etc.

d. Error Mechanisms

(1) Translational Acceleration Sensitivity

- Differential arm mass unbalance
- Arm CG offset along spin axis
- Transducer sensitivity to a_x, a_y, a_z
  - Gage compression-tension sensitivity
  - Compression induced torsion
  - etc.
  - etc.
  - Pivot anisoelasticity
- Arm anisoelasticity
- Rotor Mass Unbalance

- Spin bearing torque variations
- Spin motor torque variations
- Speed control servo pickoff
- Sum-mode excited phase or bias shift error
- Power input/output capacitor(s) torque variation
- Signal processing and data recording
- Speed control servo

(2) Angular Acceleration Sensitivity

- Rotational field error
- Arm center of mass offset
- Spin axis torque variation
- Signal processing and data recording

(3) Thermal Noise – (Sensitivity to nominal operating temperature)

- Sensor arm/damping
- Transducer
- Transducer amplifier

(4) Temperature Variation – (Sensitivity to variations in operating temperature)

- Arm differential mass unbalance shift
- Arm inertia balance shift } sum-mode mismatch factor
- Spring rate balance shift }
- Arm inertia shift } resonant frequency shift
- Spring rate shift }
- Arm anisoelasticity shift
- Transducer gain or phase shift
- Difference mode damping shift

- Electronic subsystems bias, gain, and phase shifts
  - Frequency reference oscillator
  - Sensor amplifier
  - FM modulator and transmitter
  - FM receiver and demodulator
  - Digital data processors
  - DC data processors
  - Speed control servo
    - servo electronics
    - phase/speed reference subsystem

(5) Ambient Pressure Variations

- Effect on air bearing running torque
- Effect on sensor operating temperature

(6) Humidity Variations

(7) Electromagnetic Effects

- Platform torquer interactions
- Earth's field induced torque variation due to:
  - changing orientation in field
  - field magnitude variation over earth
- Interactions from other vehicle sources

(8) Electrostatic Effects

- Torque variations in power input/output capacitors
- Charge build up on rotor

(9) Acoustic Effects

- Acoustically transmitted vibration input to sensor case
- Acoustic excitation of differential arm torques

(10) Angular Orientation Errors

Sensor

- Phase changes after initial phase calibration
- Spin axis alignment

VIALS

- Platform initial alignment (vertical and azimuth)
- Platform drift uncertainty (vertical and azimuth)

(11) Mass Proximity Noise

- Gimbal motion
- Vehicle consumables
- Vehicle orientation
- Vehicle borne mass motion
  - Crew
  - Fuel slosh
- External masses
  - Displaced air/water density variation
  - Sea wave motion
  - Other vehicle proximity (in van testing)

(12) Prime Power Variations

Prime Electric Power

- Speed control servo
- Digital data processors
- DC data processors

Air Bearing Supply (if used)

- Sensor temperature
- Spin bearing torque
- Speed control servo

(13) Time Standard Variations

- Over-all sensor phase and amplitude

(14) Component Inherent Characteristics

- Sensor Q variation with amplitude
- Sensor resonant frequency variation with amplitude
- Transducer nonlinearities
- Transducer amplifier nonlinearities, amplitude and phase distortion
- Transducer amplifier frequency response
- FM converter nonlinearity, distortion, and stability
- FM converter resolution limit
- FM transmitter nonlinearity, distortion and stability
- FM receiver nonlinearity, distortion and stability
- FM to digital conversion

- FM to analog conversion
- Digital data processing accuracy
- Analog data processing accuracy
- Digital data recording accuracy
- Analog data recording accuracy

(15) Materials Stability

Same considerations as (4).

2. RGG Coordinate Definitions

In order to properly coordinate and make use of the results of error analysis in the design, testing, evaluation, and operational phases of the RGG development program, it is necessary to establish standard definitions for many of the RGG parameters. This section establishes such standards for the definitions of reference coordinates for the RGG rotor and stator assemblies. It is recommended that this general subject of standardization be considered with regard to all of the important parameters of the RGG as the program develops.

a. Rotor Assembly Reference Frame

It is proposed that the RAR frame be defined to coincide with the nominal principal axes of inertia of the arms with the polar axis ($\bar{k}$) taken positive in the nominal direction of the spin vector. Further, when viewing the RGG with the polar axis ($\bar{k}$) pointing "up", designate the "upper" or outside arm as No. 1 and the "lower" or inside arm as No. 2. Designate the axis of minimum principal inertia of arm No. 1 as $\bar{i}$ and that of arm No. 2 as $\bar{j}$ in a right-handed sense on $\bar{k}$. Define the principal inertias of each arm as A, B, and C, as follows:

A = Minimum Transverse arm inertia

B = Maximum Transverse arm inertia

C = Polar Inertia

Based on these definitions, the inertial tensors of each arm are stated as eqs. (1) and (2).

$$\bar{\bar{\Phi}}_1 \triangleq \overline{ii}\, A_1 + \overline{jj}\, B_1 + \overline{kk}\, C_1 \tag{1}$$

$$\bar{\bar{\Phi}}_2 \triangleq \overline{ii}\, B_2 + \overline{jj}\, A_2 + \overline{kk}\, C_2 \tag{2}$$

Because of the symmetry of the arms, these definitions do not specify a unique direction for the transverse principal axes of each arm. This choice must be made at the assembly of the rotor; however, it is recommended that some scheme be devised to allow disassembly and reassembly of the rotor to the identical reference in order to provide as much continuity as possible for the instrument parameters that have been determined on the basis of the initially selected reference.

b. Stator Assembly Reference Frame

It is proposed that the SAR frame be defined such that its polar axis ($\bar{z}$) coincides with the nominal spin axis of the rotor and is positive in the direction of the spin vector. Further, it proposed that the transverse axes ($\overline{xy}$) of the SAR frame be right-handed on $\bar{z}$ and that coincidence of the RAR frame ($\overline{ijk}$) with the SAR frame ($\overline{xyz}$) be designated as the mechanical phase reference of the rotor with respect to the stator. This last definition provides the basis for describing the RAR unit vectors ($\overline{ijk}$) in terms of the SAR unit vectors ($\overline{xyz}$) as shown in eqs. (3), (4) and (5).

$$\bar{i} = \bar{x} \cos \omega_s t + \bar{y} \sin \omega_s t \tag{3}$$

$$\bar{j} = -\bar{x} \sin \omega_s t + \bar{y} \cos \omega_s t \tag{4}$$

$$\bar{k} = \bar{z} \tag{5}$$

c. Definition Consequences

As a consequence of these definitions, the "body torques" of the arms which drive the RGG differential mode will have unique time histories in terms of stator-referenced parameters. For example, let's consider the differential torque due to gravity gradient and rotational field inputs to the RGG. The gravity gradient torque on arm No. 1 about its center of mass is given approximately as eq. (6).

$$\overline{Lg} = \int_m \overline{r} \times \left[\overline{\overline{\Gamma}} \cdot \overline{r} \right] dm \tag{6}$$

The integral is taken over the mass of the arm, and when it is expanded in principal axes of inertia yields eq. (7).

$$\overline{Lg}_1 \cong \overline{i} (C_1 - B_1) \Gamma_{jk} + \overline{j} (A_1 - C_1) \Gamma_{ik} + \overline{k} (B_1 - A_1) \Gamma_{ij} \tag{7}$$

The rotational field input is just the negative of the anisoinertial moment defined by eq. (8).

$$\overline{L}_{w_1} \triangleq -\overline{\omega} \times \left[\overline{\overline{\Phi}}_1 \cdot \overline{\omega} \right] \tag{8}$$

Expansion of eq. (8) in principal axes of inertia yields eq. (9).

$$\overline{L}_{w1} = \overline{i} (B_1 - C_1) \omega_j \omega_k + \overline{j} (C_1 - A_1) \omega_i \omega_k + \overline{k} (A_1 - B_1) \omega_i \omega_j \tag{9}$$

Finally, the gravity gradient and rotational field torques acting on each arm about their polar axes are expressed from eqs. (7) and (9) as eqs. (10) and (11).

$$T_1 \cong (B_1 - A_1) (\Gamma_{ij} - \omega_i \omega_j) \tag{10}$$

$$T_2 \cong (A_2 - B_2) (\Gamma_{ij} - \omega_i \omega_j) \tag{11}$$

The differential torque may be expressed as eq. (12) when the arm transverse inertias are "matched".

$$T_d \cong 2(B-A)\left[\Gamma_{ij} - \omega_i\omega_j\right] \tag{12}$$

Our objective is to express this differential torque in terms of stator coordinates rather than rotor coordinates. This may be accomplished using the coordinate transformation defined by eqs. (3) and (4). The results are stated as eqs. (13), (14), and (15).

$$\Gamma_{ij} = \Gamma_{xy} \cos 2\omega_s t + \frac{1}{2}(\Gamma_{yy} - \Gamma_{xx}) \sin 2\omega_s t \tag{13}$$

$$\omega_i\omega_j = \omega_x\omega_y \cos 2\omega_s t + \frac{1}{2}(\omega_y^2 - \omega_x^2) \sin 2\omega_s t \tag{14}$$

$$T_d = (B-A)\left[2\Gamma_{xy} - 2\omega_x\omega_y\right]\cos 2\omega_s t + (B-A)\left[(\Gamma_{yy} - \Gamma_{xx}) + (\omega_x^2 - \omega_y^2)\right]\sin 2\omega_s t \tag{15}$$

The differential mode torque of eq. (15) is acted on by the RGG carrier filter process to produce the normalized output of eq. (16).

$$2\hat{\Gamma}_{ij} = \left[\frac{\frac{\omega_o^2}{Q}}{S^2 + \frac{\omega_o}{Q}S + \omega_o^2}\right]\left[\frac{T_d}{B-A}\right] \tag{16}$$

where

$$\omega_o \triangleq 2\omega_s$$

The filter action of eq. (16) produces a 90°phase lag at $2\omega_s$ such that when the signals are constant, the resultant output may be stated as eq. (17).

$$2\hat{\Gamma}_{ij} = \left[2\,\Gamma_{xy} - 2\omega_x\omega_y\right] \sin q\omega_s t + \left[(\Gamma_{xx} - \Gamma_{yy}) + (\omega_y^2 - \omega_x^2)\right] \cos 2\omega_s t \qquad (17)$$

Observe the sign reversal that has occurred between eqs. (15) and (17) in the second part of the equation. This result obviously provides the cross-gradient output signal in the "sine" demodulation channel as before; however, the output of the "cosine" demodulation channel differs in sign from previous analyses.

d. Summary and Conclusions

A set of RGG coordinate definitions has been proposed to provide continuity between analytical and experimental data. It is the intent that future error studies adhere rigorously to these definitions in order that consistent statistical correlation is maintained in these studies.

B. ERROR MECHANISM DERIVATIONS

1. Thermal Noise Fluctuations in the Rotating Gravity Gradiometer
2. Covariance Functions of the Rotational Field Error of the RGG
3. RGG Errors Due to Transverse Differential Arm Mass Unbalance
4. RGG Torques Due to Paramagnetic Materials

These sections discuss some of the mechanisms by which errors can be introduced into the gravity gradient tensor elements.

1. Thermal Noise Fluctuations in the Rotating Gravity Gradiometer

a. Introduction

Physical devices whose function is the measurement and/or processing of very weak signals are fundamentally performance - limited by the thermal fluctuations of their dissipative elements. The specific force "signals" which the second order gravity gradiometer must measure are extremely small (of the order of 10^{-12} g per cm with an integration time of the order of ten seconds). For this reason, thermal noise must be treated as a quantitative parameter in the design of such instruments.

b. Brief Conceptual Background of Thermal Noise

Over forty years ago, Nyquist (Ref. 6) presented a quantitative treatment of the thermal fluctuations in linear electrical systems based on the principles of thermodynamics and statistical mechanics. More recently, a general quantitative treatment of "the thermal fluctuations of generalized forces in linear dissipative systems," embodying the Nyquist result as a special case, was given by Callen and Welton (Ref. 7). An important result of this work is the "generalized Nyquist relation" which asserts that "a system with a generalized resistance $R\omega$ exhibits, in equilibrium, a fluctuating force V" whose mean square value is given by (1).

$$< V^2 > \cong \frac{2kT}{\pi} \int_0^\infty R(\omega)\, d\omega \qquad (1)$$

The right side of eq. (1) may be viewed in terms of the integral of a model power spectrum of the generalized force and re-expressed as a "two-sided" integral in terms of the circular rather than the angular frequency as eq. (2).

$$< V^2 > \triangleq \int_{-\infty}^{+\infty} S_v(f)\, df \qquad (2)$$

where

$$S_v(f) \triangleq 2\,kT\,\left|R(f)\right| \qquad (3)$$

This form of the "generalized Nyquist relation" is based on the equipartition law, and its limits of validity are the same as those of the equipartition law, i.e. it is valid when ($kT >> \hbar\nu$).*

Equation (3) may be employed to define the model noise spectra of the basic dissipative elements of electrical and mechanical systems, i.e., electrical resistance and viscous damping, as in eqs. (4) and (5).

$$S_e(f) = 2\,kT\,R \qquad (4)$$

$$S_F(f) = 2\,kT\,D \qquad (5)$$

Thus, the basic electrical and mechanical dissipative elements may be modeled as noise-free components with associated white noise generators of voltage and force (or torque), respectively, having the power spectra of eqs. (4) and (5). These concepts form the basis for the thermal noise analysis of the rotating gravity gradiometer.

c. Analytical Approach

The objective of this analysis is to develop analytical expressions for the thermal noise induced errors of the measured

---

*k 1.38×10^{-16} erg/^{o}K T = Absolute Temperature, ^{o}K

$\hbar$ 6.6×10^{-34} erg-sec ν = Frequency, Hz.

gravity gradient tensor elements in terms of the design parameters of an individual rotating gravity gradiometer.

Measurement of all of the gradient tensor elements requires a set of three rotating gravity gradiometers whose individual output measurements are uniquely combined to yield the prescribed tensor elements. The fact that six measurements are available for the estimation of five independent variables suggests the possibility that this apparent redundancy might be exploited to minimize the total measurement errors of the gradient tensor elements. Although worthy of investigation, this subject is considered beyond the scope of the thermal noise analysis. For the purposes of this analysis, it will be assumed that the three gradiometers are mutually orthogonal and that their output measurements are conventionally combined to obtain the tensor elements. This process provides the necessary "link" in this analysis between the thermal noise errors of the individual instruments and those of the gradient tensor elements.

The analytical approach consists of developing a signal processing model for a single instrument, deriving the thermal noise errors of this model, and relating these errors to those of the gravity gradient tensor elements.

d. Signal Processing Model

In order to consider two independent noise sources with different points of entry into the signal process, it is convenient to investigate this process in two sections: (1) the electromechanical portion associated with generating and transducing the basic signals, and (2) the electronic portion associated with amplification, prefiltering, phase sensitive demodulation, and postfiltering of the basic signals. The two independent noise sources of the model are equivalent torque noise with a white power spectrum of the form of eq. (5) and equivalent voltage noise with a white power spectrum of the form of eq. (4). The reason that these sources are treated separately is that they are filtered by different processes. The equivalent torque noise is filtered

by the electromechanical filter of the sensor while the equivalent voltage noise enters the signal process beyond the electromechanical filter and does not receive the benefit of this filter process. A simplified functional block diagram of the signal processing model is shown as Fig. 2, wherein the points of entry of these independent noise sources are indicated as n_T and n_e.

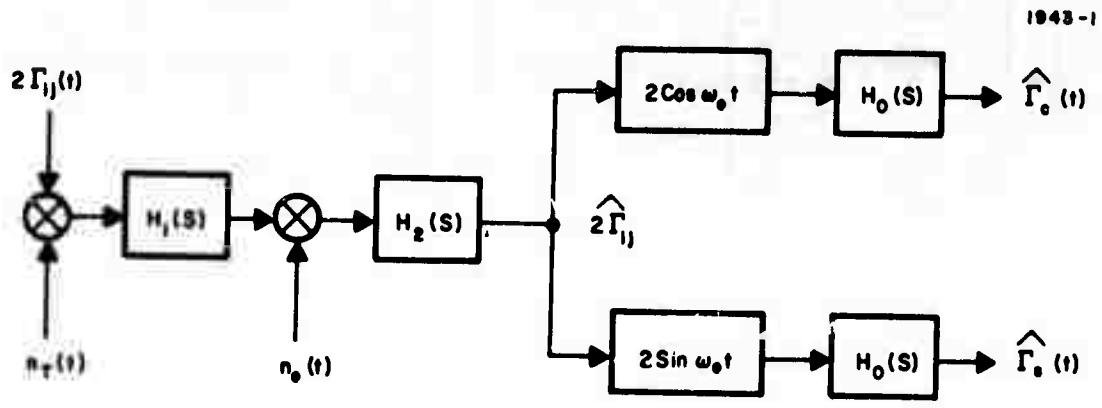

Figure 2. Signal Processing Model Block Diagram

The signal input to the process is the spatially modulated gravity gradient signal ($2\Gamma_{ij}$). The filters $H_1(s)$ and $H_2(s)$ are narrow-band filters centered at the carrier frequency of signal modulation. The first, $H_1(s)$, represents the equivalent electromechanical filter of the sensor, and the second, $H_2(s)$, represents an electronic pre-filter. The filtered carrier signal, $2\hat{\Gamma}_{ij}$, represents the resultant signal plus noise entering the linear demodulators; these are defined by the multipliers, ($2\cos\omega_o t$) and ($2\sin\omega_o t$). In this analysis the demodulation frequency, ω_o, is assumed to coincide with the center frequency of the carrier filters. The post filters, $H_o(s)$, in each channel are low-pass, and the final outputs of signal plus noise are identified symbolically as $\hat{\Gamma}_c(t)$ and $\hat{\Gamma}_s(t)$.

In order to make use of the functional signal processing model of Fig. 2, it is necessary to relate its parameters to those of the physical devices. For this purpose, the simplified model of the rotating gravity gradiometer shown in Fig. 3 will be employed.

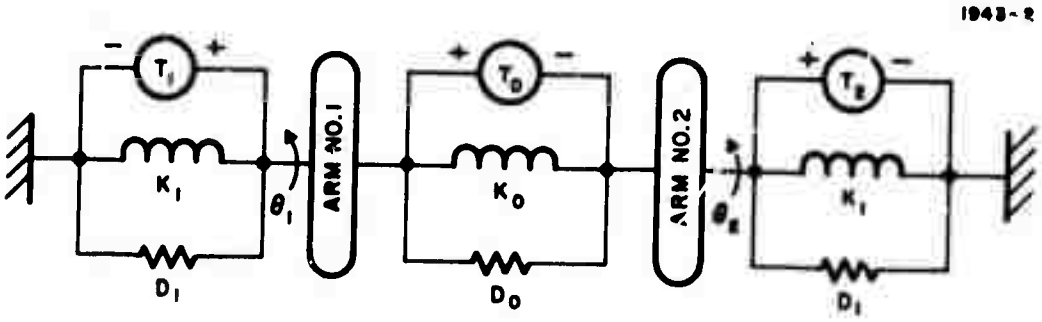

Figure 3. Rotating Gravity Gradiometer Simplified Model.

The system consists of the inertias of the two "arms" of the sensor and the three supporting springs and dampers. In addition, three white noise torque generators (T_o, T_1, T_2) are shown to be associated with the damping elements according to eq. (5). The equation of motion of each arm of the system may be expressed as eqs. (6) and (7) in terms of the principal arm inertias (A,B, C) and the spatially modulated gravity gradient signal Γ_{ij}.

$$C\ddot{\theta}_1 + D_o(\dot{\theta}_1-\ddot{\theta}_2) + K_o(\theta_1-\theta_2) + D_1\dot{\theta}_1 + K_1\theta_1$$

$$= (B-A)\,\Gamma_{ij} + T_o + T_1 \qquad (6)$$

$$C\ddot{\theta}_2 + D_o(\dot{\theta}_2-\ddot{\theta}_1) + K_o(\theta_2-\theta_1) + D_1\dot{\theta}_2 + K_1\theta_2$$

$$= (A-B)\,\Gamma_{ij} - T_o + T_2 \qquad (7)$$

The "differential mode" of this system contains the desired signal information, and its differential equation is obtained by subtracting eq. (7) from (6). The result is shown as eq. (8), where $\theta \triangleq \theta_1 - \theta_2$.

$$C\ddot{\theta} + (2D_o + D_1)\dot{\theta} + (2K_o + K_1)\theta$$

$$= 2(B-A)\Gamma_{ij} + 2T_o + T_1 - T_2 \qquad (8)$$

Equation (8) may be solved for the differential angle θ and then scaled by the factor $\left[C/B-A\right]\left[\omega_o^2/Q_1\right]$ to produce the normalized form of eq. (9).

$$\left(2\hat{\Gamma}_{ij}\right)^* = \left[\frac{\omega_o^2/Q_1}{S^2 + (\omega_o/Q_1)S + \omega_o^2}\right]\left[2\Gamma_{ij} + \frac{2T_o + T_1 - T_2}{\eta C}\right] \qquad (9)$$

where

$$\eta \triangleq (B-A)/C$$

$$\omega_o/Q_1 \triangleq (2D_o + D_1)/C$$

$$\omega_o^2 \triangleq (2K_o + K_1)/C$$

$$(2\hat{\Gamma}_{ij})^* \triangleq \theta\left[\omega_o^2/\eta Q_1\right]$$

Equation (9) is the functional form required for use in the signal processing model of Fig. 2. The appropriate identities are given by eqs. (10) and (11).

$$H_1(S) \triangleq \left[\frac{\omega_o^2/Q_1}{S^2 + \frac{\omega_o}{Q_1}S + \omega_o^2}\right] \tag{10}$$

$$\eta_T \triangleq \left[\frac{2T_o + T_1 - T_2}{\eta C}\right] \tag{11}$$

The power spectral density of η_T may be found from eq. (5) using the assumption that the torque noise sources are statistically independent. Each generator has an associated spectrum $S_{T_i}(f)$ as follows:

$$S_{T_o}(f) = 2kT\, D_o \tag{12}$$

$$S_{T_1}(f) = 2kT\, D_1 \tag{13}$$

$$S_{T_2}(f) = 2kT\, D_1 \tag{14}$$

Because of independence, the white power spectrum of η_T may be expressed as eq. (15) using eq. (11).

$$N_T(o) = \left[\frac{1}{\eta C}\right]^2 \left[4S_{T_o}(f) + S_{T_1}(f) + S_{T_2}(f)\right] \tag{15}$$

Substitution of eqs. (12), (13), (14) into eq. (15) yields eq. (16).

$$N_T(o) = \left[\frac{2kT}{\eta^2 C^2}\right]\left[4D_o + 2D_1\right] \tag{16}$$

Using the definitions following eq. (9), a normalized form of eq. (16) is shown as eq. (17).

$$N_T(o) = \left[\frac{2kT}{C}\right]\left[\frac{2\omega_o}{\eta^2 Q_1}\right] \tag{17}$$

This completes the modelling of the electromechanical part of the signal process.

Modelling of the electrical noise which enters past the electromechanical filter process requires definition of an electrical signal scale factor and an equivalent noise resistance for the specific circuitry involved. No attempt will be made here to investigate the noise characteristics of specific circuits. Rather, the form of the power spectrum of the electrical noise and its associated carrier filter are shown as eqs. (18) and (19).

$$N_e(o) \triangleq K_e^2 \left(2kT R_e\right) \tag{18}$$

$$H_2(S) \triangleq \left[\frac{\left(\frac{\omega_o}{Q_2}\right)S}{S^2 + \frac{\omega_o}{Q_2}S + \omega_o^2}\right] \tag{19}$$

The parameter K_e is the gradient scale factor associated with the electrical node for which R_e is the equivalent noise resistance.

The remaining part of the signal processing model of Fig. 2 requiring definition is the low-pass filter, $H_o(s)$. In this analysis a simple second order filter with equal roots will be assumed as defined by eq. (20).

$$H_o(S) \triangleq \left[\frac{\alpha_o}{S + \alpha_o}\right]^2 \tag{20}$$

e. Instrument Output Noise

The noise variances of the signal output functions, $\hat{\Gamma}_c(t)$ and $\hat{\Gamma}_s(t)$, may be determined from the noise power spectra of these functions. In turn these spectra may be determined on the basis of the signal processing model of Fig. 2. In effect, these spectra are the result of the filter process operating on the white noise input spectra. Simply stated, these variances are proportional to the amplitudes of the white noise spectra and to the equivalent noise bandwidths of the signal processes which act on the spectra as shown by eq. (21).

$$\sigma_c^2 = \sigma_s^2 = 2N_T(o)\,\Delta f_T + 2N_e(o)\,\Delta f_e \qquad (21)$$

The white power spectral amplitudes are defined by eqs. (17) and (18), and the equivalent noise bandwidths, Δf_T and Δf_e, must be evaluated on the basis of the various operations in the signal process model of Fig. 2. Each equivalent noise bandwidth may be determined independently of the other by similar methods.

To illustrate one approach, consider one channel of the signal process model with the normalized white noise torque function, $n_T(t)$, as its input. This is shown as Fig. 4.

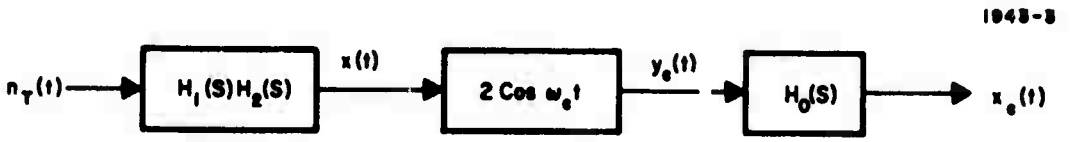

Figure 4. Signal Process Model with $n_T(t)$ as Input.

The spectrum at the output of the carrier filters $H_1(s)\,H_2(s)$, is simply stated as eq. (22).

$$S_x(f) = N_T(o) \left| H_1(S)\, H_2(S) \right|^2_{S = j2\pi f} \tag{22}$$

The spectrum of the output of the demodulation process, $y_c(t)$, may be derived as follows:

$$Y_c(t) \triangleq 2x(t) \cos \omega_o t \tag{23}$$

The autocorrelation function of the demodulator output for a stationary process is just the expectation of eq. (24).

$$R_{y_c}(\tau) = E\left\{ Y_c(t)\, Y_c(t+\tau) \right\} \tag{24}$$

From eq. (23) the desired product may be written as eq. (25).

$$Y_c(t)\, Y_c(t+\tau) = 2x(t)\, x(t+\tau) \left[\cos \omega_o \tau + \cos \omega_o (2t+\tau) \right] \tag{25}$$

Therefore, from eqs. (24) and (25) the autocorrelation of $y_c(t)$ is eq. (26).

$$R_{y_c}(\tau) = 2R_x(\tau) \cos \omega_o \tau \tag{26}$$

The Fourier transform of eq. (26) yields the power spectrum of the demodulator output as eq. (27).

$$S_{y_c}(f) = S_x\left(f + f_o\right) + S_x\left(f - f_o\right) \tag{27}$$

Note that the operation of eq. (27) is merely a frequency shift of the spectrum of the carrier filter output, x(t). This process is illustrated in Fig. 5. Note that the demodulator output spectrum has amplitude

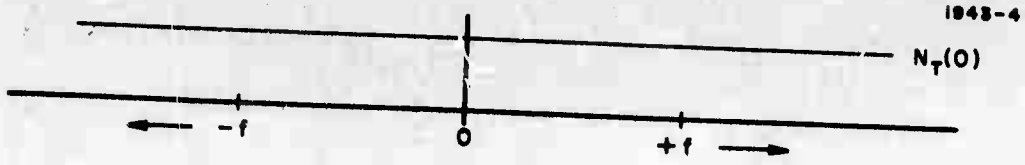

Fig. 5(a). Torque Noise Spectrum.

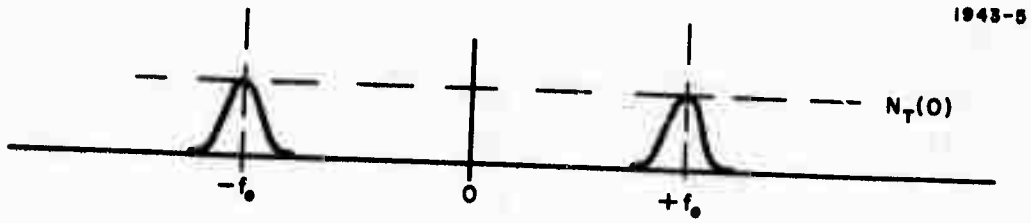

Fig. 5(b). Carrier Filter Output Spectrum.

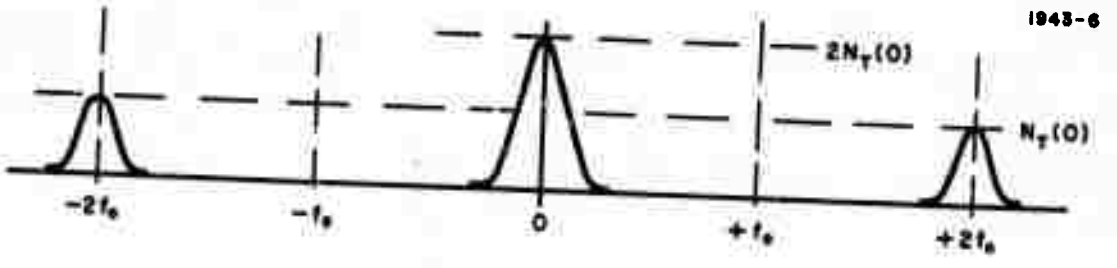

Fig. 5(c). Demodulator Output Spectrum.

$2N_T(o)$ at zero frequency. This is the result of contributions from both $S_x\left(f+f_o\right)$ in the zero frequency region.

The demodulator output is filtered by the low-pass filter, $H_o(s)$. This process removes the second harmonics of the carrier and provides filtering on the low frequency spectrum of the demodulator output. The low frequency part of the demodulator output spectrum may be expressed in terms of an equivalent low pass filter parametrically related to the carrier filters, $H_1(s)$, as in (28).

$$S^{*}_{y_c}(f) \cong 2N_T(o) \left| H_{eq}(j2\pi f) \right|^2 \tag{28}$$

After low pass filtering, the power spectrum of the output function, $x_c(t)$, may be expressed from eqs. (28) as (29).

$$S_{x_c}(f) \cong 2N_T(o) \left| H_{eq}(j2\pi f)\, H_o(j2\pi f) \right|^2 \tag{29}$$

The output variance is obtained by integration of eq. (29) over all frequencies as in eq. (30).

$$G_c^2 \cong 2N_T(o) \int_{-\infty}^{+\infty} \left| H_{eq}(j2\pi f)\, H_o(j2\pi f) \right|^2 df \tag{30}$$

The integral portion of eq. (30) is defined as the equivalent torque noise bandwidth

$$\Delta f_T \triangleq \int_{-\infty}^{+\infty} \left| H_{eq}(j2\pi f)\, H_o(j2\pi f) \right|^2 df \tag{31}$$

Note that the definition of eq. (31) when substituted into eq. (30) yields one part of the assertion of eq. (21). The other channel of the signal process containing the sin $\omega_o t$ demodulation function may be analyzed in the same way to yield the same result as stated by eq. (32).

$$\sigma_s^2 \cong 2N_T(o)\, \Delta f_T \tag{32}$$

The equivalent noise bandwidth (Δf_e) acting on the electrical noise may be computed as in (31) by using the equivalent of $H_2(s)$ rather than the equivalent of $H_1(s)\, H_2(s)$ in the integral.

The equivalent noise bandwidths, Δf_T and Δf_e, may be related to the various filter parameters in terms of the "equivalent integration times" of the filter processes as defined by eqs. (33) and (34).

$$\Delta f_T \triangleq 1/2\tau_T \tag{33}$$

$$\Delta f_e \triangleq 1/2\tau_e \tag{34}$$

To a first approximation, these equivalent integration times may be expressed as the sum of the equivalent time constants of the various filters in the signal process as shown in eqs. (35) and (36).

$$\tau_T \cong \tau_1 + \tau_2 + 2\tau_o \tag{35}$$

$$\tau_e \cong \tau_2 + 2\tau_o \tag{36}$$

where

$$\tau_i \triangleq 2Q_1/\omega_o \quad ; \text{ refer to eq. (10)}$$

$$\tau_z \triangleq 2Q_2/\omega_o \quad ; \text{ refer to eq. (19)}$$

$$\tau_o \triangleq 1/\alpha_o \quad ; \text{ refer to eq. (20)}$$

The instrument output variance defined by eq. (21) may be expressed explicitly as a function of the instrument parameters by using the power spectral amplitudes of eqs. (17) and (18) and the equivalent bandwidth relations of eqs. (33), (34), (35) and (36). This result is stated as eq. (37).

$$\sigma_o^2 = \sigma_s^2 = \left(\frac{2}{\eta}\right)^2\left(\frac{2kT}{C}\right)\left(\frac{1}{\tau_1 t_T}\right) + \left(2kT\right)\left(\frac{k_e^2 R_e}{\tau_e}\right) \qquad (37)$$

The standard deviation of the instrument output functions due to torque noise only is stated as eq. (38).

$$\sigma_T = \frac{2}{\eta}\sqrt{\frac{2kT}{C\tau_1\tau_T}} \qquad (38)$$

f. Gravity Gradient Tensor Noise

To relate the thermal noise errors of the individual instruments of a system to the resultant errors of the individual gravity gradient tensor elements, it is necessary to define the process to be employed for tensor element computation. For this purpose, consider a set of three mutually orthogonal instruments whose spin axes coincide with a measurement reference frame $\overline{(XYZ)}$. The outputs of each instrument contain signal plus noise as follows:

$$\hat{\Gamma}_{cx} = \Gamma_{zz} - \Gamma_{yy} + \eta_{cx} \qquad (39)$$

$$\hat{\Gamma}_{sx} = 2\,\Gamma_{yz} + \eta_{sx} \qquad (40)$$

$$\hat{\Gamma}_{cy} = \Gamma_{xx} - \Gamma_{zz} + \eta_{cy} \qquad (41)$$

$$\hat{\Gamma}_{sy} = 2\,\Gamma_{xz} + \eta_{sy} \qquad (42)$$

$$\hat{\Gamma}_{cz} = \Gamma_{yy} - \Gamma_{xx} + \eta_{cz} \qquad (43)$$

$$\hat{\Gamma}_{sz} = 2\,\Gamma_{xy} + \eta_{sz} \qquad (44)$$

Equations (40), (42), and (44) contain the cross-gradient elements, and these instrument outputs when divided by two yield the measured cross-gradient elements as shown in eqs. (45), (46), and (47).

$$\hat{\Gamma}_{yz} = \Gamma_{yz} + \frac{1}{2}\,\eta_{sx} \tag{45}$$

$$\hat{\Gamma}_{xz} = \Gamma_{xz} + \frac{1}{2}\,\eta_{sy} \tag{46}$$

$$\hat{\Gamma}_{xy} = \Gamma_{xy} + \frac{1}{2}\,\eta_{sz} \tag{47}$$

To obtain the trace elements of the tensor, one must employ eqs. (39), (41), and (43) in pairs and use the relation of eq. (48).

$$\Gamma_{xx} + \Gamma_{yy} + \Gamma_{zz} = 0 \tag{48}$$

For example, substraction of eq. (41) from (39) yields eq. (49).

$$\hat{\Gamma}_{cx} - \hat{\Gamma}_{cy} = 2\,\Gamma_{zz} - (\Gamma_{xx} + \Gamma_{yy}) + \eta_{cx} - \eta_{cy} \tag{49}$$

Substitution of eq. (48) into (49) yields eq. (50).

$$\hat{\Gamma}_{cx} - \hat{\Gamma}_{cy} = 3\,\Gamma_{zz} + \eta_{cy} \tag{50}$$

Division of eq. (50) by three yields one of the measured trace elements as eq. (51).

$$\hat{\Gamma}_{zz} = \Gamma_{zz} + \frac{1}{3}\left[\eta_{cx} - \eta_{cy}\right] \tag{51}$$

The other trace elements may be obtained by a similar process, and the results are stated as eqs. (52) and (53).

$$\hat{\Gamma}_{xx} = \Gamma_{xx} + \frac{1}{3}\left[\eta_{cy} - \eta_{cz}\right] \tag{52}$$

$$\hat{\Gamma}_{yy} = \Gamma_{yy} + \frac{1}{3}\left[\eta_{cz} - \eta_{cx}\right] \tag{53}$$

On the assumption that the thermal noise errors of each instrument have equal variances and are statistically independent, the standard deviations of the tensor element measurements may be written directly from the functional relations of eqs. (45), (46), (47) for the cross-gradient elements and eqs. (51), (52), (53) for the trace elements. These results are stated as (54) for the standard deviation of the cross-gradient elements and as (55) for the trace elements.

$$\sigma_{ij} = \frac{1}{2}\,\sigma_s \tag{54}$$

$$\sigma_{ii} = \frac{\sqrt{2}}{3}\,\sigma_c \tag{55}$$

The standard deviations of the instrument outputs, σ_e and σ_s, are both equal to the square root of eq. (37).

g. Summary and Conclusions

The thermal noise errors of the rotating gravity gradiometer have been analyzed on the basis of the "generalized Nyquist relation" derived by Callen and Welton. A signal processing model was developed for an individual instrument, and its spectral response to both mechanical and electrical thermal noise was analyzed. Expressions for the instrument output variances were developed, and these variances were employed in a model gravity gradient system to obtain the standard deviations of the resultant gravity gradient tensor elements.

A fundamental result of this study is that the instrument output variance due to torque noise is inversely proportional to the product of the sensor's electro-mechanical time constant (τ_1) and the total equivalent time constant of the filter process (τ_T).

2. Convariance Functions of the Rotational Field Errors of the Rotating Gravity Gradiometer

a. Introduction

The second order gradient of the specific force field at a point in a gravity field (as viewed by an observer in a rotating frame of reference) is a linear combination of the second order gradients of the gravity and rotational fields. All so-called gravity gradiometers are actually "specific force" gradiometers; and because of this, the measurements of such instruments are "contaminated" by the inertial augular velocity of their measurement frames of reference. In order to obtain the gravity gradient tensor elements from these measurements, it is necessary to correct the measurements for the rotational field effects. The differences between the actual rotational field gradients and the quantities employed for compensation are defined as the rotational field measurement errors.

The intent of this memorandum is to develop the convariance functions of the rotational field errors at the input to a single rotating gravity gradiometer under the constraint that angular velocities of the RGG are sample functions of wide sense stationary random processes with jointly gaussian probability density functions. In addition a method for determining the variances of the RGG rotational field output errors is presented.

b. RGG Rotational Field Input Errors

From the viewpoint of spectral analysis, the rotational field errors of the RGG are most conveniently treated in the non-spinning, measurement reference frame of the instrument. This approach allows formulation of the equivalent input errors to each channel

of the RGG signal process and determination of the resultant output error based on an equivalent RGG signal process filter operation on each input error.

The RGG rotational field errors are functions of the components of the RGG case referenced inertial angular velocity normal to the RGG spin reference axis. These angular velocity components may be expressed as the sums of a zero-mean random variable and a mean value (in the statistical sense) as eqs. (1) and (2).

$$\omega_x \triangleq X + M_x \tag{1}$$

$$\omega_y \triangleq Y + M_y \tag{2}$$

The "XY" designations refer to the RGG case-reference axes normal to its spin-reference axis.

In this analysis, it will be assumed that the rotational field effects are compensated by functions of the statistical means of the angular velocity components such that the rotational field input errors will be defined for each channel as eqs. (3) and (4).

$$E_c \triangleq (\omega_y^2 - \omega_x^2) + (M_x^2 - M_y^2) \tag{3}$$

$$E_s \triangleq 2\omega_x\omega_y - 2M_xM_y \tag{4}$$

Expansion of eqs. (3) and (4) using (1) and (2) yields (5) and (6).

$$E_c = Y^2 - X^2 + 2\,(M_yY - M_xX) \tag{5}$$

$$E_s = 2XY + 2\,(M_yX + M_xY) \tag{6}$$

These equations are formulated completely in terms of zero-mean random variables with the mean values of the angular velocities serving only as coefficients. The mean values of these input errors are obtained directly from eqs. (5) and (6) as (7) and (8).

$$M_c = E\left[E_c\right] = E\left[Y^2\right] - E\left[X^2\right] \tag{7}$$

$$M_s = E\left[E_s\right] = 2E\left[XY\right] \tag{8}$$

These means may be expressed also in terms of the covariance functions of the random variables evaluated at zero time shift as in eqs. (9) and (10).

$$M_c = C_y(o) - C_x(o) \tag{9}$$

$$M_s = 2\,C_{xy}(o) \tag{10}$$

c. Input Error Covariance Functions

The input error covariance functions may be expressed in terms of their autocorrelation functions and mean values as in Eqs. (11) and (12).

$$C_c(\tau) = R_c(\tau) - M_c^2 \tag{11}$$

$$C_s(\tau) = R_s(\tau) - M_s^2 \tag{12}$$

The input error autocorrelation functions may be expressed in general as the statistical expectations of the time-shifted products of each error function as in eqs. (13) and (14).

$$R_c(t_1, t_2) = E\left[E_c(t_1)\,E_c(t_2)\right] \tag{13}$$

$$R_s(t_1, t_2) = E\left[E_s(t_1)\,E_s(t_2)\right] \tag{14}$$

An expansion of eqs. (13) and (14) based on (5) and (6) will produce a sum of expectations of the products of zero mean random variables in various combinations. In general, the joint probability density function of each of these combinations must be known in order to evaluate all of these expectations. In this analysis all combinations of the zero-mean random variables are assumed to have jointly gaussian probability densities. Within this constraint, we may employ a general expansion formula (Ref. 8) for the expectation of the product of "n" zero-mean, jointly gaussian, real random variables as eqs. (15) and (16).

$$E\left[X_1 X_2 - - - X_{2k}\right] = \sum_{\text{All pairs}} \left\{ \prod_{i \neq j}^{k} E\left[X_i X_j\right] \right\} \tag{15}$$

$$E\left[X_1 X_2 - - - X_{2k+1}\right] = 0 \tag{16}$$

Equation (16) merely states that the expectation of the product of an odd number of random variables is zero. In this analysis, the number of random variables in any product does not exceed four. In this case, eq. (15) (evaluated for k=2) may be expressed as (17).

$$E\left[X_1 X_2 X_3 X_4\right] = E\left[X_1 X_2\right] E\left[X_3 X_4\right] + E\left[X_1 X_3\right] E\left[X_2 X_4\right] + E\left[X_1 X_4\right] E\left[X_2 X_3\right] \tag{17}$$

Equation (17) will be employed in the expansion of (13) and (14) using (5) and (6) in the wide sense stationary case, i.e. $t_1 = t$ and $t_2 \triangleq t + \tau$. The first step in the expansion is shown as (18) and (19).

$$R_c(\tau) = E\left[\left\{Y^2 - X^2 + 2\,(M_y Y - M_x X)\right\}_t \left\{Y^2 - X^2 + 2\,(M_y Y - M_x X)\right\}_{t+\tau}\right] \tag{18}$$

$$R_s(\tau) = E\left[4\left\{XY + M_y X + M_x Y\right\}_t \left\{XY + M_y X + M_x Y\right\}_{t+\tau}\right] \tag{19}$$

The truncated expansions of eqs. (18) and (19) are shown as eqs. (20) and (21) where the expectations of all odd-numbered products have been eliminated on the basis of (16).

$$R_c(\tau) = E\left[\left(Y^2 - X^2\right)_t \left(Y^2 - X^2\right)_{t+\tau}\right] + 4\,E\left[(M_y Y - M_x X)_t\,(M_y Y - M_x X)_{t+\tau}\right] \tag{20}$$

$$R_s(\tau) = 4E\left[\begin{array}{l}\left[(XY)_t\,(XY)_{t+\tau}\right] + M_y^2\left[X_t\,X_{t+\tau}\right] \\ + M_x^2\left[Y_t\,Y_{t+\tau}\right] \\ + M_x M_y\left[X_t\,Y_{t+\tau} + Y_t\,X_{t+\tau}\right]\end{array}\right] \tag{21}$$

Expansion of eqs. (20) and (21), using (17) where applicable, yields eqs. (22) and (23) in convariance notation.

$$R_c(\tau) = 2\left[C_x^2(\tau) + C_y^2(\tau) - C_{xy}^2(\tau) - C_{yx}^2(\tau)\right]$$
$$+ 4\left[M_y^2 C_y(\tau) + M_x^2 C_x(\tau) - M_x M_y \left|C_{xy}(\tau) + C_{yx}(\tau)\right|\right]$$
$$+\left[C_y^2(o) - 2 C_x(o) C_y(o) + C_x^2(o)\right] \qquad (22)$$

$$R_s(\tau) = 4\left[C_x(\tau) C_y(\tau) + C_{xy}(\tau) C_{yx}(\tau)\right]$$
$$+ 4\left[M_y^2 C_x(\tau) + M_x^2 C_y(\tau) + M_x M_y \left|C_{xy}(\tau) + C_{yx}(\tau)\right|\right]$$
$$+ 4 C_{xy}^2(o) \qquad (23)$$

Observe that the last terms of eqs. (22) and (23) are simply the squares of the means given by (9) and (10). Thus, in accordance with (11) and (12, the covariance functions of the input rotational field errors are expressed as eqs. (24) and (25).

$$C_c(\tau) = 2\left[C_x^2(\tau) + C_y^2(\tau) - C_{xy}^2(\tau) - C_{yx}^2(\tau)\right]$$
$$+ 4\left[M_y^2 C_y(\tau) + M_x^2 C_x(\tau) - M_x M_y \left(C_{xy}(\tau) + C_{yx}(\tau)\right)\right] \qquad (24)$$

$$C_s(\tau) = 4\left[C_x(\tau) C_y(\tau) + C_{xy}(\tau) C_{yx}(\tau)\right]$$
$$+ 4\left[M_y^2 C_x(\tau) + M_x^2 C_y(\tau) + M_x M_y \left|C_{xy}(\tau) + C_{yx}(\tau)\right|\right] \qquad (25)$$

d. Output Error Variances

The variances of the rotational field errors at the output of the RGG signal process may be obtained by integration of the output error spectra of each channel of the RGG as defined by eqs. (26) and (27).

$$\sigma^2_{co} = \int_{-\infty}^{+\infty} S_{co}(f)\, df \tag{26}$$

$$\sigma^2_{so} = \int_{-\infty}^{+\infty} S_{so}(f)\, df \tag{27}$$

The output error spectra may be obtained from the input error spectra and the equivalent filter of the signal process as shown in eqs. (28) and (29).

$$S_{co}(f) = \left|H_{eq}(j2\pi f)\right|^2 S_c(f) \tag{28}$$

$$S_{so}(f) = \left|H_{eq}(j2\pi f)\right|^2 S_s(f) \tag{29}$$

The input error spectra may be derived in terms of the angular rate spectra by taking the Fourier transforms of the covariance functions of (24) and (25). The general results of this process are expressed as eqs. (30) and (31) wherein convolution operations on the rate spectra are required for the nonlinear terms in the covariance functions.

$$S_c(f) = 2\left[S_x(f) * S_x(f) + S_y(f) * S_y(f)\right]$$

$$- 2\left[S_{xy}(f) * S_{xy}(f) + S_{yx}(f) * S_{yx}(f)\right]$$

$$+ 4\left[M_y^2 S_y(f) + M_x^2 S_x(f)\right]$$

$$- 4 M_x M_y \left[S_{xy}(f) + S_{yx}(f)\right] \qquad (30)$$

$$S_s(f) = 4\left[S_x(f) * S_y(f) + S_{xy}(f) * S_{yx}(f)\right]$$

$$+ 4\left[M_y^2 S_x(f) + M_x^2 S_y(f)\right]$$

$$+ 4 M_x M_y \left[S_{xy}(f) + S_{yx}(f)\right] \qquad (31)$$

An approximate method of determining the output variances is to replace the output spectra in eqs. (26) and (27) with the input spectra and to restrict the integration to a narrow frequency band centered at zero frequency of width equal to the equivalent bandwidth of the RGG signal process as shown in eqs. (32) and (33).

$$\sigma_c^2 \cong \int_{-\frac{\Delta f}{2}}^{+\frac{\Delta f}{2}} S_c(f)\, df \qquad (32)$$

$$\sigma_s^2 \cong \int_{-\frac{\Delta f}{2}}^{+\frac{\Delta f}{2}} S_s(f)\, df \qquad (33)$$

e. Summary and Conclusions

The covariance functions of the rotational field errors were derived for the case where the random angular rates of the RGG measurement frame have wide sense stationary, jointly gaussian probability density functions. Also a method for determining the variances of the rotational field output errors of each channel of the RGG was presented.

Application of the results of this study presents computational difficulties because of the requirement for spectral convolution of the angular rate spectra and because of the requirement for knowledge of the cross spectra in addition to the co-spectra of the RGG angular rates.

3. RGG Errors Due to Transverse Differential Arm-Mass-Unbalance

The component of mass unbalance of each arm of the RGG normal to its principal torsional axis in the presence of case translational accelerations produces time varying "body torques" about the principal torsional axis of the RGG. The difference of these arm-mass-unbalance "body torques" of the two arms is a driving function of the differential mode of the RGG and, as such, is capable of producing errors in the sensible output of signals of the RGG. The intent of this memorandum is to derive analytical expressions which relate these output errors to the input translational accelerations and to the transverse differential arm-mass-unbalance of the RGG.

a. Brief Descriptions of Arm-Mass-Unbalance Torque

In general, the acceleration induced "body torque" acting about the center support of a body whose center of mass is displaced by $\bar{r}$ from its center of support is given by eq. (1), where $\bar{a}$ is the acceleration of the center of support and m is the mass of the body.

$$\bar{L}_a = m\,\bar{a} \times \bar{r} \tag{1}$$

The "body torque" of each arm of the RGG acting about its principal torsional axis ($\bar{z}$) may be stated from eq. (1) as (2) and (3).

$$T_1 = \bar{z} \cdot \left[m_1\,\bar{a}_1 \times \bar{r}_1\right] \tag{2}$$

$$T_1 = \bar{z} \cdot \left[m_2\,\bar{a}_2 \times \bar{r}_2\right] \tag{3}$$

In the case of pure translational acceleration of the RGG, the "center of support" accelerations are equal, and the effective torque acting on the differential mode of the RGG may be expressed as the difference of eqs. (2) and (3).

To the first order, the RGG arm masses are equal, and the differential mode mass unbalance driving torque may be expressed as eq. (4).

$$T_d = \bar{z} \cdot \left[m \bar{a} \times \bar{h} \right] \tag{4}$$

where $\bar{h} = \bar{r}_1 - \bar{r}_2$

Expansion of eq. (4) in RGG cease-fixed coordinates ($\overline{xyz}$) yields eq. (5).

$$T_d = m (a_x h_y - a_y h_x) \tag{5}$$

The differential arm mass unbalance components, h_x and h_y, are time variable due to the spatial modulation produced by the RGG rotation frequency (ω_s), i. e.

$$h_x (t) = h \cos (\omega_s t + \phi) \tag{6}$$

$$h_y (t) = h \sin (\omega_s t + \phi) \tag{7}$$

where ϕ is the fixed mechanical phase of the differential arm-mass-unbalance vector ($\bar{h}$) relative to the principal axes of the RGG arms.

For analytical convenience here, this mechanical phase will be assumed zero such that eq. (5) may be expressed as eq. (8).

$$T_d \triangleq mh \left[a_x \cos \omega_s t - a_y \sin \omega_s t \right] \tag{8}$$

At this point it is convenient to normalize the error torque of eq. (8) with respect to the input signal ($2\Gamma_{ij}$) of the RGG signal process. This normalized error function is shown as eq. (9), where η is the arm inertial efficiency and C is the principal polar inertia of one arm.

$$\Gamma_d \triangleq \frac{T_d}{\eta C} = \frac{mhg}{\eta C} \left[\frac{a_x}{g} \cos \omega_s t - \frac{a_y}{g} \sin \omega_s t \right] \tag{9}$$

b. Signal Processing

For the purposes of this analysis it is convenient to determine the power spectrum of the normalized error function of eq. (9). This may be accomplished by first deriving its autocorrelation function as defined by eq. (10).

$$R_d(t_1, t_2) = E \left[\left\{ \Gamma_d (t_1) \; \Gamma_d(t_2) \right] \right. \tag{10}$$

Assuming the statistics of the input accelerations are wide sense stationary, the error function autocorrelation may be expressed as eq. (11).

$$R_d(\tau) = \left[\frac{mhg}{\eta C} \right]^2 \left[\begin{array}{l} 1/2 \left\{ R_x(\tau) + R_y(\tau) \right\} \cos \omega_s \tau \\ +1/2 \left\{ R_x(\tau) - R_{yz}(\tau) \right\} \sin \omega_s \tau \end{array} \right] \tag{11}$$

When the input accelerations are uncorrelated, their cross-correlations are zero, and eq. (11) simplifies to eq. (12).

$$R_d(\tau) = 1/2 \left[\frac{mhg}{\eta C}\right]^2 \left[R_x(\tau) + R_y(\tau)\right] \cos \omega_s \tau \qquad (12)$$

The Fourier transform of eq. (12) yields the power spectrum of the error function for the assumed conditions.

$$S_d(f) = 1/2 \left[\frac{mhg}{\eta C}\right]^2 \left[\frac{S_x(f + f_s) + S_x(f - f_s) + S_y(f + f_s) + S_y(f - f_s)}{2}\right] \qquad (13)$$

If we assume that the spectra of the accelerations on each axis are identical, eq. (13) simplifies to eq. (14).

$$S_d(f) = \left[\frac{mhg}{C}\right]^2 \left[\frac{S_a(f + f_s) + S_a(f - f_s)}{2}\right] \qquad (14)$$

Equation (14) shows that the error function spectrum is proportional to the frequency shifted acceleration spectra. This spectrum is filtered by the narrow band process, $H_1(s)$, of the RGG defined by eq. (15).

$$H_1(s) \triangleq \left[\frac{\frac{\omega_o^2}{Q}}{S^2 + \frac{\omega_o}{Q} S + \omega_o^2}\right] \qquad (15)$$

where $\omega_o \triangleq 2\omega_s$

The resultant spectrum after the narrow band filter process is stated as eq. (16).

$$S_e(f) = \left|H_1(j2\pi f)\right|^2 S_d(f) \tag{16}$$

After the narrow band filter process, the filtered error signal is demodulated into two channels by the linear functions, $2\cos\omega_o t$ and $2\sin\omega_o t$, to yield the spectra of eqs. (17) and (18).

$$S_c(f) = \left[S_e(f + f_o) + S_e(f - f_o)\right] \tag{17}$$

$$S_s(f) = \left[S_e(f + f_o) + S_e(f - f_o)\right] \tag{18}$$

After demodulation, the signal in each channel is filtered by the low pass filter, $H_o(s)$, to remove the second harmonics of (f_o). The resultant spectrum of each channel is stated by eq. (19).

$$S_c^*(f) = S_s^*(f) = \left|H_o(j2\,f)\right|^2 \left[S_e(f + f_o) + S_e(f - f_o)\right] \tag{19}$$

The variances of the output errors may be obtained by integration of eq. (19) over all frequencies as in eq. (20).

$$\sigma_c^2 = \sigma_s^2 = \int_{-\infty}^{+\infty} \left|H_o(j2\pi f)\right|^2 \left[S_e(f + f_o) + S_e(f - f_o)\right] df \tag{20}$$

This integral may be evaluated to sufficient accuracy by examining the previously described processes graphically. First consider the spectrum of eq. (16). This is sketched as Fig. 6, and its peak value is determined from eq. (14) as stated in eq. (21).

$$S_e(2f_s) = \left(\frac{mhg}{\eta C}\right)^2 \left[\frac{S_a(3f_s) + S_a(f_s)}{2}\right] \tag{21}$$

The demodulation processes of eqs. (17) and (18) shift the spectrum of Fig. 6 by $\pm f_o$. This result is shown as Fig. 7.

The low pass filter, $H_o(s)$, removes the second harmonics of f_o from the spectrum of Fig. 7 and narrows the bandwidth of the zero frequency centered part as shown in Fig. 8.

The equivalent bandwidth of the spectrum of Fig. 8 is approximately the same as the equivalent noise bandwidth (Δf_{eq}) of the entire signal process. Thus, the output error variances may be stated in terms of an "effective acceleration" variance (σ_a^2) from eq. (21) and Fig. 8 as eq. (22).

$$\sigma_c^2 = \sigma_s^2 \cong \left(\frac{mhg}{\eta C}\right)^2 \sigma_a^2 \tag{22}$$

where $$\sigma_a^2 \triangleq \left[S_a(3f_s) + S_a(f_s)\right] \Delta f_{eq}$$

Care should be observed in evaluating the "effective acceleration" variance to ensure that the "two-sided" magnitudes of the acceleration spectra are used and that these magnitudes are expressed in the units of "g^2/Hz."

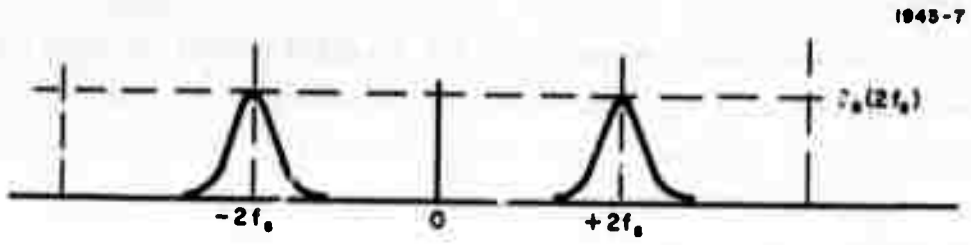

Fig. 6. Spectrum of Eq. (16).

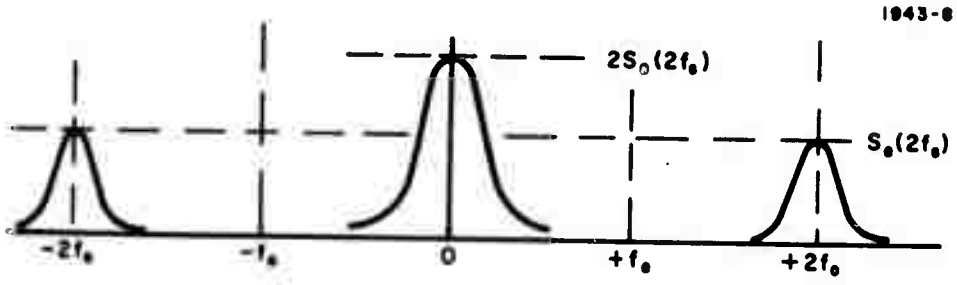

Fig. 7. Spectrum Shift Due to Demodulation Processes.

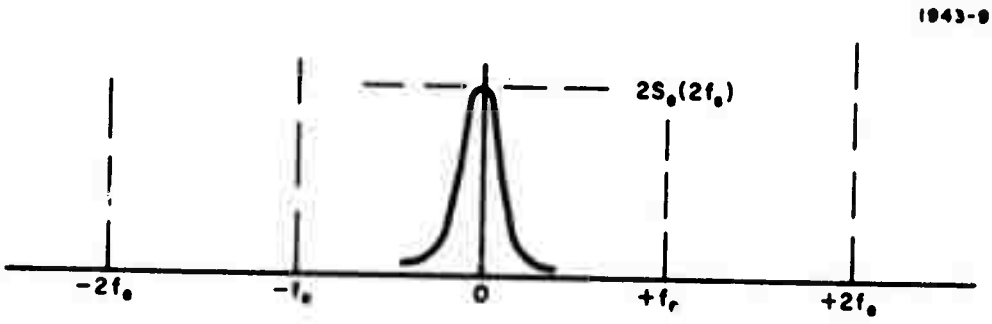

Fig. 8. Narrowed Bandwidth.

The standard deviations of the gradient tensor elements may be determined from eq. (22) with one exception, i. e., the trace elements of the gradient tensor are obtained from pairs of RGG outputs. Common accelerations acting on the mass unbalance of each RGG produce correlated errors in the gradient tensor trace elements depending on the relative mechanical phases of pairs of mass unbalance vectors. The resultant trace element variance may be stated as eq. (23).

$$\sigma_{ii}^2 = 1/9 \left[\frac{mg}{\eta C}\right]^2 \left[h_1^2 + h_2^2 + h_1 h_2 \cos(\phi_2 - \phi_1)\right] \sigma_a^2 \qquad (23)$$

The subscripts are used to denote the parameters of each RGG in a particular pair. The cross-gradient variances are a function of one instrument only, and these variances are defined by eq. (24).

$$\sigma_{ij}^2 = 1/4 \left(\frac{mgh}{\eta C}\right)^2 \sigma_a^2 \qquad (24)$$

To avoid confusion, the variances of all of the gradient tensor elements are expressed as eqs. (25 through (30) using the spin axis coordinate as the parametric identification.

$$\sigma_{xx}^2 = 1/9 \left[\frac{mg\sigma_a}{\eta C}\right]^2 \left[h_y^2 + h_z^2 + h_y h_z \cos(\phi_y - \phi_z)\right] \qquad (25)$$

$$\sigma_{yy}^2 = 1/9 \left[\frac{mg\sigma_a}{\eta C}\right]^2 \left[h_x^2 + h_z^2 + h_x h_z \cos(\phi_x - \phi_z)\right] \qquad (26)$$

$$\sigma_{zz}^2 = 1/9 \left[\frac{mg\sigma_a}{\eta C}\right]^2 \left[h_x^2 + h_y^2 + h_x h_y \cos(\phi_x - \phi_y)\right] \qquad (27)$$

$$\sigma_{xy}^2 = 1/4 \left[\frac{mg\sigma_a}{\eta C}\right]^2 \left[h_z^2\right] \quad (28)$$

$$\sigma_{xz}^2 = 1/4 \left[\frac{mg\sigma_a}{\eta C}\right]^2 \left[h_y^2\right] \quad (29)$$

$$\sigma_{yz}^2 = 1/4 \left[\frac{mg\sigma_a}{\eta C}\right]^2 \left[h_x^2\right] \quad (30)$$

Note that the mass unbalance parameters (h_i) are the total magnitudes of the mass unbalance vectors of each RGG whose spin axis coincides with the (i^{th}) reference coordinate.

c. Error Variance Evaluation

The first step in evaluating the error variances is the evaluation of the "effective acceleration" variance defined in eq. (22). Previous estimates of the acceleration spectra on a "one-sided" basis yield the following values at one and three times the spin frequency.

$$2S_a(f_s) \cong 4.5 \times 10^{-9}\ g^2/Hz \quad (31)$$

$$2S_a(3f_s) \cong 8.9 \times 10^{-10}\ g^2/Hz \quad (32)$$

The "effective acceleration" variance, based on an equivalent bandwidth of $\Delta f_{eq} = 0.05$ Hz, is stated as eq. (33).

$$\sigma_a^2 \cong \left[\frac{4.5 \times 10^{-9} + 8.9 \times 10^{-10}}{2}\right]\left[.05\right] g^2 \cong \left[11.6 \times 10^{-6} g\right]^2 \quad (33)$$

The standard deviations of the gradient tensor elements will be evaluated assuming that all mass unbalance magnitudes are equal and that the

correlating mechanical phase angles are zero. This assumption yields the worst case, and the results are stated as eqs. (34) and (35).

$$\sigma_{ii} = \frac{1}{\sqrt{3}} \left[\frac{mgh\sigma_a}{\eta C} \right] \tag{34}$$

$$\sigma_{ij} = 1/2 \left[\frac{mgh\sigma_a}{\eta C} \right] \tag{35}$$

d. Summary and Conclusions

The RGG output error due to differential arm-mass-unbalance driven by translational acceleration was investigated in terms of the power spectra of the input accelerations and the filter process of the gradiometer. The results show that this RGG error variance is proportional to input acceleration spectral magnitudes at one and three times rotation frequency (as anticipated).

An "effective acceleration" variance was defined for this error source in terms of the acceleration spectral magnitudes at one and three times rotation frequency and of the equivalent bandwidth of the RGG signal process.

Analytical expressions were derived for the gradient tensor error variances, and it was shown that the trace element variances are functions of the phase differences of the mass unbalance vectors of the pairs of instruments whose outputs are used to compute the particular trace elements.

4. RGG Torques Due to Paramagnetic Materials

Most materials suitable for use in the construction of the RGG are paramagnetic and magnetic fields can introduce torques in these paramagnetic materials at the even harmonics of the rotation frequency. (The harmonics higher than the second will be rejected by the signal processor and will be disregarded in this analysis.)

If a paramagnetic bar is introduced into a uniform magnetic field magnetic poles will be induced in the bar and the bar will tend to align itself with that field. If it is assumed that all of the flux from the induced poles emanates from the end of the bar then estimates can be made of the induced torque on the bar. This is an oversimplification but it provides simple equations with practically acceptable accuracies for relatively long bars and the assumption will be used in this analysis.

a. Magnetic Fields and Poles

In the cgs electromagnetic system the force on a magnetic pole is

$$F = Hm \tag{1}$$

where:

F = force on pole in dynes

H = field strength in oersteds

m = pole strength in emu.

The flux emanating from a magnetic pole is

$$\phi = 4\pi m \text{(maxwells)} \ . \tag{2}$$

If a paramagnetic bar is introduced into a magnetic field the magnetic flux balance in the bar will be

$$\phi_b - \phi_o = 4\pi m \tag{3}$$

where:

ϕ_b = flux in the bar

ϕ_o = the flux in the volume occupied by the bar with the bar removed

$4\pi m$ = flux due to the induced poles in the bar.

Dividing (3) by the cross section area of the bar, A we obtain

$$\frac{\phi_b}{A} - \frac{\phi_o}{A} = \frac{4\pi m}{A} \quad . \tag{4}$$

where

$\phi_b/A \triangleq B_b$ = flux density in the bar

and

$\phi_o/A \triangleq B_o$ = flux density in free space

and

$B_o \triangleq$ H in the emu system.

Rewriting (4) using these definitions, we obtain

$$B_b = H + \frac{4\pi m}{A} \tag{5}$$

Thus, the magnetic flux density in the bar can be calculated if the field strength and the induced pole strength are known.

b. Magnetic Field Due to a Current Carrying Conductor

The magnetic field strength due to current flow in an infinitely long conductor is, at a distance x:

$$H = \frac{2I_{ab}}{x} \text{ oersteds} \tag{6a}$$

and the magnetic field gradient at this point is:

$$\frac{dH}{dx} = -\frac{2I_{ab}}{x^2} \text{ oersteds/cm} \tag{6b}$$

where:

I_{ab} = abamperes = 10 amperes practical

x = distance in centimeters

For short lengths of wire, the above calculations are accurate to a few percent if the length is 10 times the distance x.

c. Permeability and Susceptibility

These terms are used to describe the magnetic characteristics of materials. Permeability (μ) is defined in the emu system by (7)

$$\mu = \frac{B_b}{H} = 1 + \frac{4\pi m}{HA} \tag{7}$$

It is seen that the right hand side of (7) can be obtained by dividing (5) by H.

Susceptibility (χ) is defined by (8) for susceptibility per unit mass.

$$\chi = K/\rho \tag{8}$$

Susceptibility may also be defined on the basis of molecular weight (χ_m) or atomic weight (χ_a). This section will be based on the unit mass values commonly tabulated for metals.

In equation (8) ρ is the density and K is a constant defined

$$K = \frac{m}{HA}$$

Thus, equation (7) can be written

$$\mu = 1 + 4\pi K \tag{9a}$$

or

$$\mu = 1 + 4\pi\chi\rho \tag{9b}$$

The permeability and susceptibility of some common materials are shown in Table II from Refs. 1, 3, and 5.

d. Torque on a Bar Magnet

If a bar magnet length ℓ, with pole strengths +m and -m, is introduced into a uniform field of strength H at an angle θ to the field, we have from eq. (1) and the geometry

$$\text{Torque} = m\ell H \sin\theta. \tag{10}$$

TABLE II

Magnetic Properties of Pure Materials

	$\chi \times 10^6$	ρ	μ
Aluminum	+0.63	2.68	1.0000212
Beryllium	-1.0	1.85	0.9999767
Copper	-0.086	8.96	0.9999900
Tungsten	+0.28	19.3	1.0000675
Uranium	+2.6	19.1	1.000624
Elgiloy			1.00004
Air			1.00000036
Mercury	-0.18	13.6	0.999969
Crown Glass	-0.90	2.47	0.999972
Permalloy			100,000
Iron, technically pure			6,500
Cast iron			600

T724

e. Linear Magnetic Field Torque on a Paramagnetic Bar

It is seen from eq. (3)

$$\phi_b - \phi_o = 4\pi m. \tag{3}$$

that poles of strength $\pm m$ are induced in a bar when it is introduced into a field. From (7) for a field of H oersteds

$$\mu = 1 + \frac{4\pi m}{HA} \tag{7}$$

or

$$\mu = 1 + \frac{4\pi m\ell}{HA\ell} = 1 + \frac{4\pi m\ell}{H\ Vol}$$

or

$$H(\mu - 1) = \frac{4\pi m\ell}{Vol}$$

and

$$m\ell = \frac{(\mu-1)\ H\ Vol}{4\pi} \quad . \tag{11}$$

This "magnet" of pole strength m and length ℓ can be substituted into (10) and

$$\text{Torque} = \frac{(\mu-1)\ H^2\ Vol\ \sin\theta}{4\pi} \quad . \tag{12}$$

Two things have not been taken into account in the derivation of (12). These are: the demagnetizing effect and the reduced projected area of the ends of the bar when it is not parallel to the field. The reduced area coefficient is simply cos θ.

When the bar is introduced into the field the induced poles tend to counteract the initial field. Thus, the effective field H is

$$H = H' - NKH = H' - N\chi\rho H \tag{13}$$

where

H = effective field

H' = initial field in a vacuum

N = demagnetizing factor.

N varies from nearly zero for long thin rods to 4π for flat plates. For paramagnetic materials with mass susceptibilities in the ranges shown in Table II, we can say

$$H \approx H'$$

even if N is as large as 4π, its maximum value.

Thus, the final torque equation for a paramagnetic bar introduced into a magnetic field of strength H is

$$\text{Torque} = \frac{(\mu-1)\, H^2\, \text{Vol} \sin\theta \cos\theta}{4\pi} \tag{14}$$

or

$$\text{Torque} = \chi \rho H^2\, \text{Vol} \sin\theta \cos\theta \tag{15}$$

where

Torque = dyne cm
χ = emu units
ρ = grams/cc
H = field strength in oersteds
Vol = cubic cm of the bar

f. Forces on a Paramagnetic Mass in Nonuniform Field

The force on a homogenous mass M in a nonuniform magnetic field is derived by Williams (ref. 1):

$$f = \chi M H \frac{dH}{dx} \tag{16}$$

where

f = dynes

χ = emn

M = mass

H = oersteds

dH/dx = oersteds/cm .

The torque on an arm with a concentrated mass M/2 at each end and an arm length of 2r in a gradient field is

$$\text{Torque} = f_1 r_1 - f_2 r_2 = (f_1 - f_2)\, r \cos\theta$$

$$= \left(\chi \frac{M}{2} H_1 \frac{dH}{dx} - \chi \frac{M}{2} H_2 \frac{dH}{dx}\right) r \cos\theta$$

$$= \left(\chi \frac{M}{2} \frac{dH}{dx}\, r \cos\theta\right)\left(H_1 - H_2\right)$$

but

$$H_2 = H_1 - r \sin\theta \frac{dH}{dx} \text{ for constant } \frac{dH}{dx}$$

and

$$\text{Torque} = \left(\chi \frac{M}{2} \frac{dH}{dx}\, r \cos\theta\right)\left(H_1 - H_1 + r \sin\theta \frac{dH}{dx}\right)$$

$$= \chi \frac{M}{2} r^2 \left(\frac{dH}{dx}\right)^2 \sin\theta \cos\theta \qquad (18a)$$

This can be written from (9b) as:

$$\text{Torque} = \frac{(\mu-1)\, V_m}{8\pi}\, r^2 \left(\frac{dH}{dx}\right)^2 \qquad (18b)$$

where

μ = permeability of the end masses

V_m = volume of both end masses

r = radius to the center of the end masses

$\frac{dH}{dx}$ = oersteds/cm gradient

g. Summary of Magnetic Field Induced RCG Torques

Torques are introduced in the RGG due to formation of magnetic poles in the arms and end masses and by the magnetic field gradient acting on the end masses. The gradient torque on the arm itself is negligible compared to the torque due to the end masses. These torques are from eqs. (14) and (18)

$$\text{Torque} = \frac{(\mu_a - 1)\, H^2\, V_a}{4\pi} \sin\theta \cos\theta$$

$$+ \frac{(\mu_m - 1)\, V_m\, r^2}{8\pi} \left(\frac{dH}{dx}\right)^2 \sin\theta \cos\theta \qquad (19)$$

where:

μ_a = a composite value of permeability for the arm and end mass as a whole ≈ 1.00005

V_a = volume of arm and end masses $\simeq 160$

μ_m = permeability of the end masses ≈ 1.00007

r = radius from pivot to center of the end masses ≈ 5 cm

V_m = volume of end masses ≈ 80cc

Inserting the above approximate values the peak torque equation becomes

$$\text{Torque} = 3.1 \times 10^{-4} H^2 + 2.8 \times 10^{-3} \left(\frac{dH}{dx}\right)^2 \text{ d cm peak} \qquad (20)$$

h. Magnetic Fields and Gradients Expected

The magnetic field of the earth has a field strength of about 0.7 oersted and a maximum gradient of approximately 3.3×10^{-9} oersted/cm. The magnetic field of a long straight wire carrying one ampere is 0.02 oersted at 10 cm and the gradient at this point is 0.002 oersted. It is believed that all magnetic fields, except that due to the earth, can be kept below about 0.1 oersted and the gradients below 0.01 oersted/cm. Thus it is evident that only the earth's field is significant.

The RGG torque introduced by the earth's field could be as large as:

$$\text{Peak Torque} = 3.1 \times 10^{-4} \times (0.7)^2 + 2.8 \times 10^{-3} \times (0.01)^2$$

$$= 1.5 \times 10^{-4} \text{ dyne cm (due to earth's magnetic field)} \qquad (21)$$

The peak torque in the RGG due to a gravity gradient is

$$\text{Peak Torque} = \eta C \Gamma_{eq}/2$$

$$= 1.5 \times 10^{-5} \text{ d-cm/EU}$$

Thus the peak torque at the sensor resonant frequency due to the earths magnetic field will be approximately 10 EU. However, this is constant in direction and magnitude over distances of hundreds of miles except in areas with iron or nickel ore concentrations. Thus, the induced magnetic torques can be considered as a bias and compensated with trivial error.

i. Conclusions

The earth's magnetic field will introduce significant bias terms in the RGG gradient tensor outputs. However, these will be constant over long periods of time and over large distances and can be compensated with negligible error.

Torques due to nearby magnetic devices and current carrying conductors can be held to trivial values. Shielding of the RGG will not be necessary in general.

C. DESIGN CONCEPTS AND PARAMETERS

1. Selection of resonant frequency and Q for the RGG
2. RGG Sensor Electronics
3. Arm Mass Unbalance and Arm Inertia Unbalance Mechanical Adjustments
4. Vibrational Motion Environment Estimates
5. Preliminary Gradiometer Designs
6. Isoelasticity of Spherical Gimbal Support with Hydrostatic Bearing Pads
7. Spin Bearing Requirements
   a. Gradient Errors Due to Sum-Mode Mismatch
   b. Torque Variations with Eccentricity in Fluid Journal Bearing

c. Phase Error Due to Spin Bearing Disturbance Torque

d. Spin Bearing Procurement Specification

8. RGG Baseline Parameters

These sections treat many aspects of the RGG design and establish values for some of the parameters. Future design and analysis will be based on these parameters.

1. Selection of Resonant Frequency and Q for a RGG

a. Introduction

Inspection of the factors involved in the selection of resonant frequency (ω_o) and Q demonstrates that a single equation cannot be written that will provide a precise determination of the optimum values for these parameters. Instead each factor must be evaluated in terms of its effect on a complete gravity gradient measuring system and compromises made as required. The factors to be considered are:

(1) The thermal noise in the gravity gradient tensor elements has a specific limit.

(2) The transducer output signal level must be at least a few 10's of nanovolts per EU signal.

(3) For ease in fabricating low noise electronics the signal frequency should be above approximately 10 Hz.

(4) The signal phase shift uncertainty must not exceed 0.735 mv (0.0042 deg) total through the system.

(5) The sensor time constant ($\tau = 2Q/\omega_o$) cannot be allowed to be equal to the total allowed system time constant since some filtering must be provided for preamplifier noise.

(6) The frequency of the sensor must be high enough that the mechanical parts, particularly pivots, are not too flimsy to work with.

(7) The piezo-electric transducer output impedance must be reasonable, i. e. not too high.

(8) The ω_o selected should avoid any peaks in the environmental spectrum.

(9) The natural frequency must not be so high that the losses in the spin bearing become intolerable.

(10) The centrifugal acceleration on the arm mass balance adjustment tubes must not exceed approximately 50 g's.

b. Baseline Parameter Selection

After reviewing these factors it was decided to make a preliminary selection of the limiting sensor and system parameters and determine if this allowed a viable detailed baseline RGG sensor and system design. Accordingly the following parameter limits were established.

c. Preliminary Baseline Parameter Limits

σ_{ij} = 1/3 EU maximum RMS noise signal for each of the elements of the computed gravity gradient tensor

Q = 300 max. The Q of the sensor difference mode.

f_o = 35 Hz nominal undamped resonant frequency of the sensor in the difference mode.

τ_i = 10 sec, system (sensor plus filters) equivalent integration time defined by the AFCRL specification.

The rationale for the selection of each parameter is discussed in the various sections.

(1) Thermal Noise Considerations — It has recently been shown that the one sigma value of the noise output of the sensor, a demodulator-RC filter system and a RSS sine and cosine summing circuit is

$$\sigma_N = \frac{4}{\eta \sqrt{\tau_s \tau_i}} \sqrt{\frac{kT}{C_{zz}}} \qquad (1)$$

where:

τ_s = the sensor time constant $\left(\frac{2Q}{\omega_o}\right)$

τ_i = equivalent integration time of the sensor and the filter; ($\tau_i = \tau_s + \tau_f$) which is specified as 10 seconds for this system.

η = inertia efficiency of the sensor arms.

C_{zz} = polar moment of inertia of one sensor arm.

k = Boltzman constant

T = temperature ^oK ($290^oK = 17^oC$ assumed)

The above equation can also be written

$$\sigma_{ij} = \frac{1}{\eta \tau_i} \sqrt{\frac{2kT}{C_{zz}}} \sqrt{\frac{\omega_o \tau_i}{2Q}} \qquad (2)$$

and

$$\sigma_{ii} = \frac{2\sqrt{2}}{\eta 3 \tau_i} \sqrt{\frac{2kT}{C_{zz}}} \sqrt{\frac{\omega_o \tau_i}{2Q}}$$

where

σ_{ij} = one sigma value of thermal noise in the off diagonal elements of the gradient tensor. Specified in the preliminary parameters as 1/3 EU maximum.

σ_{ii} = one sigma noise in the trace elements.

Since σ_{ij} is slightly larger than σ_{ii} and if σ_{ij} is held to 1/3 EU, the system will be within the required limits on the other elements of the tensor.

The thermal noise analysis also shows that:

$$\sigma_N \equiv \sqrt{2}\,\sigma_s \equiv \sqrt{2}\,\sigma_c \equiv 2\sqrt{2}\,\sigma_{ij}$$

where:

σ_N = one sigma of the thermal noise in the root-sum-square sensor output.

σ_s = one sigma of the thermal noise in the sine channel.

σ_c = one sigma of the thermal noise in the cosine channel.

Thus, with a 1/3 EU system limit on σ_{ij} the limiting value of σ_N is 0.946 EU due to thermal noise.

The parameters in eq. (2) can be considered as follows. It is always a design goal to make the sensor inertia efficiency η as high as possible with practical values from 0.7 to 0.97. The required value for σ_N has just been shown to be 0.946. The sensor must be operated near 300°K and the integration time τ_i is specified by the AFCRL contract. Since ω_o and Q have been selected on a preliminary basis considering all of the pertinent factors the only remaining factor in eq. (2) is C_{zz}.

Evaluating $\sigma_{ij} = 1/3$ EU, in eq. (2) we find

$$\tau_i = 10 \text{ sec specified} = \tau_s + \tau_f$$

$$\tau_s = 2Q/\omega_o = 2.73 \text{ seconds}$$

$$\tau_f = 7.27 \text{ sec}$$

$$\eta^2 C_{zz} = 26,400 \text{ gram cm}^2 \ (2.64 \times 10^{-3} \text{ kg m}^2)$$

for

$$f_o = 35 \text{ Hz}$$

$$\omega_o = 220 \text{ rad/sec (actual 219.91)}$$

$$kT = 4 \times 10^{-14} \text{ ergs } (4 \times 10^{-21} \text{ joules})$$

$$T = 290^{\circ}\text{K } (17^{\circ}\text{C})$$

$$Q = 300$$

All of these values seem to be within practical design limits and the thernal noise consideration is satisfied.

(2) Signal Level Considerations — The signal level must be at least a few 10's of nanovolts/EU. Signal levels below 10 nanovolts at frequencies below 10 kHz are very difficult to work with. They are difficult to generate for test, difficult to shield and difficult to amplify linearly. In addition, the one EU signal level should be much higher than the preamplifier noise so that the preamplifier noise does not contribute significantly to the output signal noise. However, if the signal level exceeds a few hundred nv/EU little is gained by forcing the piezoelectric transducer design to attain the highest possible signal level since this level is limited to about 1000 nv/EU by other considerations. A signal level of about 1000 nv/EU requires about the same circuitry and the same care as a signal level of a few hundred nv/EU. A final reason for not attempting to obtain a very

large signal out of the piezoelectric material is that this would be a deviation from Hughes experience. Hughes has not studied or experimented with transducer characteristics at high signal levels.

The peak differential angle of the sensor, from page 380 of the AFCRL proposal, is

$$\theta_{peak} = \frac{Q}{\omega_o^2} \eta 3\Gamma \qquad (3)$$

Since the output signal is a linear function of differential angle (all other parameters remaining constant) it is apparent that the largest output voltage would be obtained by making Q large and ω_o small. However this statement does not allow establishing an optimum ratio for Q and ω_o or an optimum value for either one.

The peak signal strain energy in the sensor springs is from page 381 of the AFCRL proposal.

$$\epsilon_{peak\ mech} = \frac{C_{zz}}{4} \left(\frac{\eta Q}{\omega_o} 3\Gamma \right)^2 \qquad (4)$$

where

ϵ_p = peak mechanical energy stored in the sensor springs

η = inertia efficiency ratio = 0.861

ω_o = the undamped natural frequency of the sensor

3Γ = equivalent gravity gradient input = 10^{-9} sec^{-2} = 1 EU

C_{zz} = polar moment of inertia of one sensor arm
3.561×10^{-3} kg m^2

Q = mechanical Q of the sensor = 300

ω_o = sensor resonant frequency = 220 rad/sec

$$\epsilon_p \text{ mech} = 1.23 \times 10^{-21} \text{ joules (watt sec)/EU} \quad (5)$$

If 1.0 % of this mechanical energy is absorbed by the piezoelectric transducer, part of it is converted to electrical energy and this is determined by the bending coupling factor k_b. The relation for the transducer is

$$\epsilon_{\text{peak elect}} = \frac{k_b^2 \text{ peak mech}}{100}$$

where:

$$k_b^2 = \left(\frac{3}{4} k_{31}\right)^2$$

and k_{31}, one of the piezoelectric constants for the material being considered is

$$k_{31} \approx 0.34$$

Therefore

$$k_b^2 \approx 0.065$$

and

$$\epsilon_{\text{peak elect}} = 8 \times 10^{-25} \text{ joules}$$

The piezoelectric transducer acts as a capacitor and a reasonable value for the capacity is

$$C = 2 \text{ nF} \quad (6)$$

This provides a transducer output impedance of

$$X_C = -j\frac{1}{\omega_o C} = -j\ 2.27 \times 10^6 \text{ ohms}$$

which is satisfactory, see Section 7.*

The peak transducer output voltage will be

$$\epsilon_{peak} = \left(\frac{2\,\epsilon_{p\ elect}}{C}\right)^{1/2}$$

$$\epsilon_{peak} = 2.83 \times 10^{-8} = 28.3 \text{ nanovolts/EU}$$

This signal level is acceptable in a practical sensor design. In general, a higher percentage of the sensor energy would be stored in the transducer and a lower impedance could result. Thus the transducer output can be expected to be in the low hundreds of nanovolts per EU and have few megohms output impedance.

From the point of view of the signal level the preliminary design parameters are satisfactory.

(3) Signal Frequency Considerations — The sensor signal frequency must be above about 10 Hz to allow reasonable component size and values in the preamplifier. Up to perhaps 100 Hz, component sizes decrease inversely with increasing frequency. This consideration indicates that the frequency should be as high as possible. The preliminary specification for f_o = 35 Hz is a convenient working frequency and thus satisfies this requirement.

---

*AFCRL Proposal.

(4) Signal Phase Shift Considerations — It is shown on page 462 of the AFCRL proposal that the error introduced into the off diagonals off the gradient tensor by a phase error ϕ is given by

$$2\Gamma_{ij} \text{ error} = -3\Gamma \sin 2\phi$$

where

$$\Gamma = GM/R^3$$

ϕ = the total phase error of the sensor output with respect to the reference coordinate system

For the small phase angles involved this can be assumed to be linear and thus the phase accuracy required is the average accuracy over the specified 10-second integration time.

For small angles and for a sensor operating with its spin axis horizontal at the earth's surface

$$\Gamma_{ij} \text{ error} = \frac{3}{2}\frac{GM}{R^3}\Delta\phi$$

$$= 2250\Delta\phi \text{ EU}$$

If it is desired to limit Γ_{ij} error to 1/3 EU due to this cause then

$$\Delta\phi = 7.41 \times 10^{-5} \text{ radians} = 0.0042 \text{ degrees}$$

The sensor $\Delta\phi$ error is due to (1) gradiometer servo including the frequency reference; (2) sensor phase error due to a shift in its

natural frequency; (3) phase pick-off and electronics. If these are assumed to be statistically independent,then 0.00242 degrees, 1 sigma, can be allowed for each source. This is the error that will be tentatively allowed.

The phase error due to the servo and frequency reference or due to a change in sensor resonant frequency is shown on page 471 of the AFCRL proposal to be

$$\Delta\phi = \frac{360}{\pi} Q \frac{\omega}{\omega_o} \text{ degrees} \qquad (3)$$

where the $\Delta\omega$ may be either the shift in the servo and reference frequency or the shift in the sensor resonant frequency. Limiting the phase error due to each of these causes to 0.00242 degrees, the frequency control accuracy requirement becomes for a Q of 300

$$\frac{\Delta\omega}{\omega_o} = 7.1 \times 10^{-8}$$

The phase shift error is a linear function of the sensor Q and thus a low Q is desirable from this point of view. However, if Q is made small the thermal noise equation (1) shows that C_{zz} must be increased to compensate for any reduction in Q to maintain the same thermal noise limit. Increasing C_{zz} requires an increase in the physical size of the sensor and this is undesirable. The value of Q selected (300) provides a reasonable physical size and a manageable phase shift problem. Since frequency always enters the phase shift problem as the ratio $\Delta\omega/\omega_o$ the actual frequency selected is not important.

The basic frequency reference stability is not a problem. General radio frequency synthesizers are on hand that are good to one part in 10^9. A preliminary design for a digital servo that can

maintain the required accuracy has been made. This servo will be analyzed in detail and presented in the final report.

A preliminary analysis of the temperature sensitivity of the sensor resonant frequency has also been made and the required accuracy appears to be state of the art. This analysis will be completed and presented in the final report.

(5) Sensor Time Constant Considerations – The thermal noise equation for the sensor can be written as

$$\sigma_N = \frac{4}{\sqrt{\tau_s\,(\tau_s + \tau_f)}} \sqrt{\frac{kT}{\eta^2 C_{zz}}}$$

where:

τ_s = sensor time constant $\left(\frac{2Q}{\omega_o}\right)$

τ_f = filter time constant

$(\tau_s + \tau_f) = \tau_i$ = system integration time specified as 10 seconds

Consideration of this equation shows that the smallest value of σ_N results if τ_s is made equal to 10 seconds and the filter time constant is reduced to zero. If this were to be done it would have three adverse effects. These are:

- The sensor Q would have to be raised which would increase the signal phase shift problem.
- The ω_o would have to be lowered which would increase the electronic circuit problems and increase the size of the sensor mounted electronics.
- No filtering would be available for the noise introduced by the signal preamplifier.

The first two items have been discussed in detail in previous paragraphs and the assumed values for Q and ω_o have been deemed acceptable. The adequacy of the filtering after the preamplifier will now be examined.

Only the first stages of a low level – low frequency amplifier need be considered as noise sources since if these stages have a gain of 10 or more, the noise contribution of the following stages is negligible.

As shown in the section on RGG Sensor Electronics, the first stages of the amplifier to be used consist of two low-noise field effect transistors and a low-noise operational amplifier. The gain of this combination is 20 and the estimated noise will be 17 nanovolts per square root Hertz. The "square root Hertz" refers to the equivalent bandwidth of the data handling system. Since the preamplifier, amplifier, frequency converter and transmitter are all relatively wide bandwidth, the preamplifier noise bandwidth will be determined by the equivalent noise bandwidth of the output filter.

It is shown on pages 390 and 392 of the Hughes AFCRL proposal that equivalent noise bandwidth for a linear filter is

$$\Delta f_{noise} = \frac{1}{2\,\tau_f}$$

The previously selected parameters provide a $\tau_f = 7.27$ seconds and the root-mean-square amplifier noise will be

$$E_N \text{ amplifier} = 4.5 \text{ nanovolts rms}$$

If this 4.5 nanovolt amplifier noise signal is root-sum-squared with a signal of approximately 30 nv for one EU signal the 4.5 nv is seen to be negligible.

(6) Sensor Component Size and Rigidity Considerations – It is shown in two other sections of this report that the sum mode frequency (β) and the difference mode frequency (ω_o) are approximately:

$$\omega_o^2 = \frac{(2 K_o + K_1)}{C_{zz}}$$

$$\beta^2 = \frac{K_1}{C_{zz}} \left(1 + \frac{2 C_{zz}}{J_s}\right) = \frac{1.54 K_1}{C_{zz}}$$

where:

ω_o = difference mode frequency = 220 rad/sec

β = sum mode frequency

K_o = total torsional stiffness of the difference mode pivot system. Two pivots plus two transducers in the base line design

K_1 = torsional stiffness of each pair of end pivots. There are four "end pivots" in the base line design

C_{zz} = polar moment of inertia of an arm of the sensor = 3.561×10^{-3} kg m^2

J_s = polar moment of inertia of the sensor stator = 2.526×10^{-3} kg m^2.

The sum mode frequency should be lower than the difference mode frequency so that the end pivots act as torsional isolators and limit the arm inertia mismatch problem as shown in another section of this report. In order to demonstrate size and rigidity of parts it is reasonable to say that all six pivots will be made identical and that the transducers will store 20 percent of the peak system energy. These ratios may be modified slightly in a final design. With this assumption the equation for ω_o can be written

$$\omega_o^2 = \frac{7.5 K_p}{C_{zz}} \quad \text{and} \quad \beta^2 = \frac{3.08 K_p}{C_{zz}}$$

where K_p is the torsional stiffness of each individual pivot.

The torsional stiffness of a cylindrical pivot is

$$K_p = \frac{\pi G d^4}{32 \ell}$$

where:

G = the shear modulus, 4.5×10^{10} for beryllium copper

d = pivot diameter

ℓ = pivot length.

Combining the last two equations

$$\frac{d^4}{\ell} = \frac{32 \omega_o^2 C_{zz}}{7.5 \pi G}$$

If it is assumed that $\ell = 2d$, this becomes

$$d^3 = \frac{2.72 \omega_o^2 C_{zz}}{G} \text{ meters}^3$$

and

$$d = 2.15 \times 10^{-3} \text{ meters}$$

or

$$d = 0.0845 \text{ inches}$$

$$\ell = 0.169 \text{ inches}$$

It is reasonable to make pivots of this size with good control.

The cross-section area of each pivot will be

$$A = \frac{\pi}{4}(0.0845)^2 = 5.6 \times 10^{-3} \text{ in.}^2$$

Since only the end pivots support the load, then 4 pivots support two arms of 1.563 kg x 2.2 = 3.44 lb each. The shearing stress in each pivot will be at 1g.

$$S_s = \frac{2 \times 3.44}{4 \times 5.6 \times 10^{-3}} = 307 \text{ psi/g}$$

This is very safe loading in any expected environment.

Based on this same assumption that all of the pivots are identical and 20% of the difference mode sensor energy is stored in the piezoelectric transducer the sum mode frequency is

$$f_{sum} = \left(\frac{f_o^2 \times 3.08}{7.5}\right)^{1/2} = 22.4 \text{ Hz.}$$

This is a satisfactory sum mode frequency.

These computations demonstrate that the selected ω_o and Q allow safe and reasonable sensor pivot designs and a satisfactory sum mode frequency.

(7) Transducer Output Impedance Considerations – In the previous paragraph on signal level considerations it was shown that satisfactory signal levels were obtained if only 1 percent of the peak sensor energy was stored in the piezoelectric transducer and the transducer had an output capacity of 2 nF. In the final design it is

expected that approximately 20% of the peak system energy will be stored in the two transducers, 10% in each. With the higher energy available, the signal level can be raised above the previously calculated or the output capacity can be increased and the output impedance lowered. The final parameter balance will be determined by the design of the piezoelectric transducer.

It was previously shown that the 2 nanofarad output capacity gave an output impedance of 2.27×10^6 ohms. This is connected to the preamplifier input impedance of about 10^9 ohms shunted by a few picofarads input capacity. The phase shift and signal loss is negligible for this situation and will have even less effect in the final design.

The transducer output impedance is satisfactory using the selected sensor parameters.

(8) Environmental Considerations of ω_o Selection – The linear and angular vibration spectrum in any laboratory or vehicle will contain peaks at certain frequencies. These peaks are usually due to nearby rotary equipment operating at nearly constant speed. In the laboratory the peaks are largely due to 1725 RPM (28.8 Hz) induction motors driving compressors and pumps. In an airplane they occur at engine rotation speed.

The ω_o selected (35 Hz or 220 rad/sec) is well removed from the expected environmental peaks and is high enough that effective vibration isolation is relatively easy.

(9) Spin Bearing Loss Considerations – The sensor spin bearing drag is essentially a linear function of ω_o. The spin bearing specification allows the mean running torque to be as high as 5×10^4 dyne cm at 17.5 Hz (110 rad/sec). The power loss in the bearing under these conditions will be

$$W = \text{Torque} \times \omega_s = 0.55 \text{ watts}$$

This is considered to be an acceptable spin bearing loss.

(10) Upper Acceleration Limit – The upper acceleration limit that the arm mass balance adjustment devices can withstand without danger of malfunctioning is approximately 50 g's. Assuming that the balance devices can be located within 1.5 inches of the center of rotation then the acceleration is

$$g's = \frac{\omega_s^2 r}{980} \approx 50$$

Thus the selected sensor resonant frequency is satisfactory from the balance device acceleration limit point of view.

2. RGG Sensor Electronics

Electronic circuits have been designed to perform all of the signal and logic functions required at the sensor. These functions are divided into the following groups:

- Piezoelectric Transducer Amplifier and Telemetry Circuit
- Power Supply
- Balance and Gain Control Logic Circuit

Each function is described in detail in the following paragraphs and the schematic diagram is shown in Fig. 9.

a. Piezoelectric Transducer Amplifier and Telemetry Circuit

(1) Description – The voltage out of the piezoelectric transducer undergoes two stages of amplification by bandpass amplifiers A_1 and A_2, and drives the voltage-controlled oscillators (VCO). The VCO has a center frequency of 200 kHz and deviates ±100 kHz for the largest drive signals. The VCO output is buffered by Q_3 and drives the output telemetry capacitor.

Preamplifier – Amplifier A_1 and field-effect transistors Q_1 and Q_2 form a high-input-impedance operational amplifier with an open-loop gain of several million. Feedback elements R_1, C_1, R_2, and C_2 establish a closed-loop gain of 20 at 35 Hz with 6 dB per octave rolloffs above and below this frequency.

Changes in DC level of the input signal at P_1 by up to 1.2 volts are tolerated and matched by a corresponding change in the voltage of P_2. Constant-current diode D_1 ensures that changes in DC level do not affect the Q1 and Q_2 operating current. Transistor Q_4 provides 46 dB of power supply isolation for the preamplifier.

Post Amplifier – Field-effect transistor Q_5 is normally turned off. In this case, amplifier A_2, with feedback network C_3, R_3, R_4, has a gain of $R_4/30$ K at 35 Hz and a 6 dB per octave rolloff

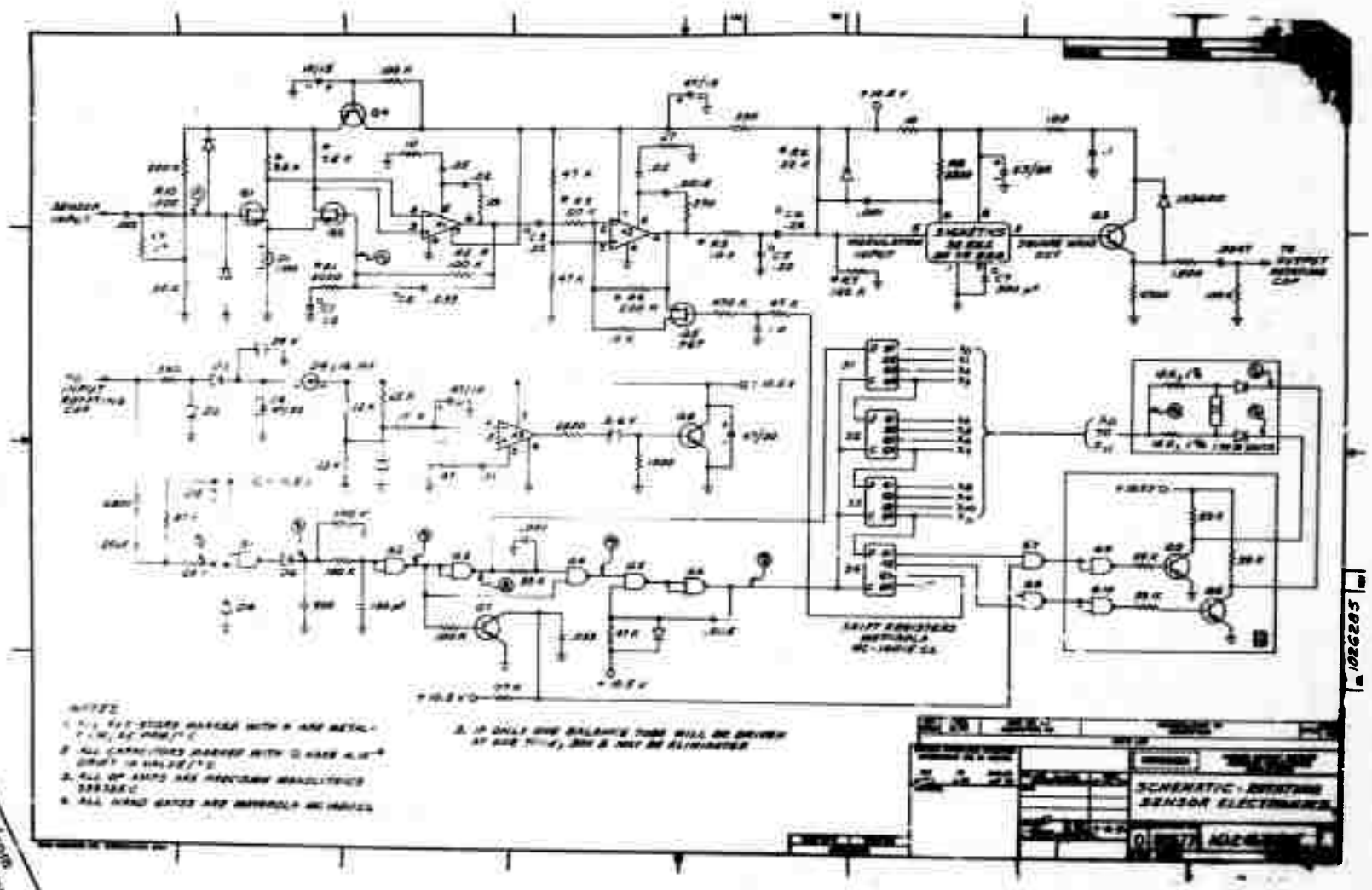

Fig. 9. Electronic Circuit Schematic Diagram.

below 35 Hz. R_4 is chosen to optimize the gain of the system so that the maximum expected input signal drives the VCO at its maximum frequency deviation, ±100 kHz. The amplifier also may be operated in a low-gain mode by turning on Q_5.

R_5, C_5, C_6, R_6, and R_7 re-establish an accurate DC level (9.2 volts) for the VCO input, and provide additional 6 dB per octave rolloffs above and below 35 Hz.

Voltage-Controlled Oscillators – VCO with timing resistor R_8 and timing capacitor C_7, produces a 200 kHz square wave when the drive voltage at pin 5 is at the center of its range, 9.2 volts. Deviations from this value of ±0.15 volt produce frequency deviations of ±20 kHz.

Emitter-follower Q_3 buffers the VCO output providing a 5 volt peak-to-peak 200 ±100 kHz square wave for the rotating plate of the output telemetry capacitor.

(2) Specifications – Noise is generated in the preamplifier primarily by transistors Q_1 and Q_2, resistors R_1, R_9, and R_{10}, and amplifier A_1. The equivalent input noise voltage per root Hz, en, is given by

$$\epsilon n^2 = 4kT\,R_1 + 4kT\,R_{10} + 4kT\,R_9\left(\frac{X_G^2}{R_9^2}\right) + 2\,\epsilon_Q^2, + \epsilon_{A_1}^2\left(y^2_{FQ}/R_{11}^2\right)$$

X_G = Reactance of piezoelectric sensor

ϵ_Q = Equivalent gate noise voltage per root Hz of Q_1 and Q_2

ϵ_{A1} = equivalent input noise voltage per root Hz of amplifier A_1.

y_{FQ} = transconductance of Q_1, Q_2.

For our devices,

$$X_G = 2.5 \times 10^6\ \Omega$$

$$\epsilon_Q = 6 \times 10^{-9}\ \text{volts}/\sqrt{\text{Hz}}$$

$$\epsilon_{A1} = 8 \times 10^{-9}\ \text{volts}/\sqrt{\text{Hz}}$$

$$y_{FQ} = 1400\ \Omega$$

$$R_{11} = 7500\ \Omega$$

$$R_9 = 10^9\ \Omega$$

$$R_1 = 5000\ \Omega$$

$$R_{10} = 1000\ \Omega$$

and therefore $\epsilon_n = 17\ \text{nv}/\sqrt{\text{Hz}}$. This corresponds to 0.1 EU for a sensor with 45 nv per EU using a 7.27 second output filter integration time.

Gain and Phase - Shift Drift — Since the open loop voltage gains of A_1 and A_2 are greater than 10^6, gain drift and phase drift in the preamp and post amp will only be due to changes in value of the feedback-loop and network capacitors and resistors, R_1, C_1, R_2, C_2, C_3, R_3, R_4, R_5, C_5, C_6, R_6, and R_7. Since these feedback networks have Q's near unity, the percent phase drift and percent gain drift are

roughly equal to the sum of the percent drifts in values of these capacitors and resistors. Metal film resistors are available with drifts in value less than 25 parts per million per degree Centigrade (ppm/^{o}C). Capacitors (such as metalized film) are available with drifts less than 25 ppm/^{o}C and with leakage resistance greater than $5 \times 10^{10}\ \Omega$.

In an environment temperature-controlled to 1^{o}C, the phase and gain of the preamp and post amp. will drift less than 0.5 milliradian and 0.05 percent respectively.

The frequency drift of the VCO is about 100 ppm/^{o}C. The FM gain drift will be less than one-fourth this value since our peak excursions are one-fourth the total oscillator range. This will add another 0.0025 percent gain drift to the system.

Linearity – Because of the high open-loop gains of amplifiers A_1 and A_2, and the high quality of available feedback elements, non-linearity will arise primarily in the voltage-controlled oscillator, VCO. For excursions of ±20 kHz about 200 kHz, the voltage-to-frequency non-linearity is about 0.2%. The FM detector outside the gradiometer will be a phase-locked loop using an identical VCO as reference oscillator. This should reduce the overall voltage-to-frequency-to-voltage non-linearity to less than 0.05%.

b. Power Supply

Power for the sensor electronics is brought in continuously by a rotating power-input capacitor. The outside fixed plate is driven with 80 volts rms at 500 kHz. The inner rotating plate charges storage capacitor C_8 through rectifiers D_2 and D_3.

The total power supply current is 16 milliampere. To supply this current, the power-input capacitors must be 100 to 300 pf. This will charge capacitor C_8 to 24 volts DC. Current diode D_6 and the 24-volt zener clamp on C_8 create a 16 ma supply to Q_7 that is nearly independent of variations in the capacitors of the power-input capacitor. A_3 and Q_7 form a shunt regulator with an impedance of less than $10^{-3}\Omega$. Since the parallel resistance of D_6 is greater than $10^{5}\Omega$, the supply

voltage will vary less than 10^{-8}% for a one % variation in capacitance of the power-input capacitor. Use of the shunt regulator rather than a series regulator keeps changing circuit current requirements from affecting the reaction force applied to the power-input capacitor.

c. Balance and Gain-Control Logic Circuit

(1) Description – Sixteen binary bits of information are held by the sensor electronics package. These bits control the operation of the balance tubes and adjust the sensor amplifier gain. The user may supply a new set of sixteen bits at any time by telemetering them in serially on the 500 kHz power supply input.

Each successive bit is entered by briefly interrupting the 500 kHz power. A 100 μsec interruption is a logical one and 300 μsec interruption is a logical zero. Successive binary bits are shifted down a sixteen-bit shift register. After sixteen new bits are supplied, these are available on the sixteen shift-register parallel outputs.

The first twelve bits select one of twelve balance tubes and bits thirteen and fourteen select the polarity of the current (or no current at all) supplied to the selected tube. Bit fifteen, if set, lowers the gain of the sensor amplifier by turning on Q_5.

(2) Logic Elements – The elements G and S are of a new Motorola family of low-power MOS logic. They consume only ten nanowatts per package and operate well on 10 volts. The logic levels are roughly 10 volts for logic one and roughly ground for logic zero. The outputs will sink or source several milliamperes.

(3) Control Logic – When 500 kHz power is supplied, point P_3 (at the input to G_1) oscillates between ground and 10.5 volts. The output of word gate G_1 also oscillates, and through D6 charges P4 to 10 volts.

When the 500 kHz is interrupted, point P_3 stays at 10.5 volts, the output of G_1 stays at ground, and P_4 goes to ground. Thus, a negative pulse occurs at P_4 when the 500 kHz is interrupted.

Inverter G_2 and G_3 converts this to a positive pulse at P_5 and again a negative pulse at P_6.

Nand gate G_4 outputs a logical one (±10 volts) except for the brief interval (30 μsec) following a positive transition of P_5. The 30 μsec-pulse initiates the 200 μsec one-shot multivibrator formed by G_5 and G_6. The trailing edge of the one-shot output at P_8 clocks the edge-clocked shift registers S_1, S_2, S_3, and S_4. These shift registers are connected in series as one 16 bit serial-in, parallel out shift register. The input is at line PD.

The shift register is clocked 200 μsec after each interruption of the 500 kHz supply. If the interruption is greater than 200 μsec, P_6 is at logical zero (ground) when it is clocked into the shift register (through line PD). If the interruption was less than 200 μsec, P_6 has returned to one when it is clocked into the shift register.

(4) Balance Driver – A balance tube is driven by setting its bit (1 through 12) to one. The direction of current flow is selected by setting either bit 13 or bit 14 to one. This sets point P_9 for that tube at 10 volts, and sets point P_{10} or P_{11} to ground. One milliampere then flows through the tube in the direction selected by bits 13 and 14. If bits 13 and 14 are both zero, then P_{10} and P_{11} are both at 10.5 volts and no current flows.

Since the outputs of G_7 and G_8 will not saturate when sinking two milliamperes, if more than one balance tube is to be driven at one time, the current amplifiers in box B must be included.

Transistor Q_7 and word gates G_7 and G_8 interrupt balance-tube current for 12 millisec after each bit is entered. This suppresses all the current while the sixteen new bits are entered. These are entered at a 2 kHz rate (500 μsec between bits).

3. Sensor Arm Mass-Unbalance and Inertia-Unbalance Mechanical Adjustment

It is the purpose of this section to estimate the limits to which sensor arm mass and inertia unbalance can be adjusted and the stability limits of that adjustment.

a. Mechanical Mass Balance Adjustment

Experience has shown that a 0.25 gram, 80 pitch, screw can be manually adjusted to within ±1/10 turn. This provides an incremental mass balance adjustment of

$$(\Delta mh) = 8 \times 10^{-4} \text{ gram cm.}$$

If the nonrotating sensor is vibrated at $2\omega_s$ $(=\omega_c)$ the output signal in terms of equivalent gravity gradient is

$$\Gamma_{(\Delta mh)} = \frac{Ag(\Delta mh)}{\eta C} \cos(\omega_o t + \alpha)$$

where:

A = peak acceleration in "g"

g = gravity

Δmh = magnitude of the sensor mass unbalance vector

ηC = sensor arm inertia efficiency x arm polar inertia = 3.066×10^4 gm cm^2

ω_o = 220 rad/sec

α = phase angle

If the nonrotating sensor has a residual mass unbalance of 8×10^{-4} gm cm and it is vibrated at 5×10^{-3} g the sensor output will be

$$\Gamma_{(\Delta mh)} = 129 \cos(\omega_o t + \alpha) \quad \text{(EU)}$$

This is an easily readable signal and thus the manual adjustment of mass unbalance can be made as proposed.

b. Balance Tube Mass Unbalance Adjustment

Each of the mercury filled balance tubes has a total range of 1.4×10^{-3} gm cm. If the gap is initially centered the adjustment range will be $\pm 7 \times 10^{-4}$ gm cm. It is proposed to use 8 balance tubes in each direction on each arm giving a balance range with the mercury tubes of*

$$\Delta mh = \pm 56 \times 10^{-4} \text{ gm cm/arm/axis, available}$$

The mechanical mass unbalance adjustment is well within the range of the balance tube system and assembly of the sensor can be completed and final balance accomplished on the rotating sensor. The balance tube gap position can be adjusted to a small fraction of a millimeter on a rotating sensor by the electronic circuits discussed in another part of this report.

It will be shown in a subsequent paragraph of this section that the arm mass unbalance allowed is

$$(\Delta mh) = 4 \times 10^{-4} \text{ gm cm maximum allowed.}$$

This resolution is easily obtainable by the balance tubes.

The mass unbalance adjustment signal for a rotating sensor can be calculated from the equations on page 337 of the AFCRL proposal after the equations are corrected as shown below.

$$\Gamma_{accel} = \frac{Ag(\Delta mh)}{2\eta C} \cos(2\omega_s t + \beta)$$

when vibrated at ω_s.

*Since it is desired to place the mass center of the arm at the center of rotation of the sensor the concept of simply matching the two arm unbalances and thus reducing (Δmh) to zero can not be used.

If we assume that we would like to balance to 10% of the maximum desired unbalance, and further assume that we can vibrate the table at 5×10^{-3}g, then

$$A = 5 \times 10^{-3} g$$

$$(\Delta mh) = 4 \times 10^{-5}$$

$$\eta C = 3.066 \times 10^{4}$$

$$\Gamma_{accel} = 3.2 \cos (2\omega_s t + \beta) \quad \text{EU}$$

This is a good working level signal.

c. Inertia-Unbalance Mechanical Adjustment

It is shown in paragraph 7a of this section entitled "Gradient Errors Due to Sum-Mode Mismatch" that the sum-mode mismatch coefficient is defined by the equation

$$k_\beta \frac{K_1}{I_1} \triangleq \frac{A_1}{I_1} - \frac{A_2}{I_2} = \frac{D_1 S + K_1}{I_1} - \frac{D_2 S + K_2}{I_2}$$

where:

$k\beta$ = sum-mode mismatch coefficient

K_1 = end pivot stiffness for arm 1

D_1 = end pivot damping for arm 1

K_2 = end pivot stiffness for arm 2

D_2 = end pivot damping for arm 2

I_1 = polar inertia of arm 1

I_2 = polar inertia of arm 2

If the damping is assumed to be zero and K_1 equal to K_2 then

$$k_\beta \approx \frac{I_2 - I_1}{I_2} = \frac{\Delta I}{I}$$

where:

ΔI = the difference in the polar moment of inertia of the two arms

I = the nominal polar inertia of either arm

The polar moment of inertia of two small screws each of mass m_s, each at a distance r_s from the center of rotation is

$$I_{screws} = 2 m_s r_s^2$$

the differential inertia for a shift of each screw a distance dr_s is

$$dI_s = 4 m_s r_s dr_s$$

and for small motions

$$\Delta I_s = 4 r_s (m_s \Delta r_s)$$

If the same 0.25 gm - 80 pitch balance screws are assumed to be placed at a radius of 2 cm and rotated 1/10 turn, then for the arms with a polar moment of inertia of 35,610 gm cm^2

$$k_\beta = \frac{\Delta I_s}{I} = \frac{4 \times 2 \times 0.25}{80 \times 10 \times 35,610}$$

$$= 0.7 \times 10^{-7}$$

It is shown in the previously referenced section of this report that a $k_\beta = 10^{-6}$ is desired in this sensor to limit the $2\omega_s$ torque from the bearing from coupling into the sensor and to limit signal overloading due to torques at the spin frequency, ω_s. We can achieve an inertia unbalance adjustment to 1/10 that required without the use of the balance tubes.

It is also shown in the previously referenced section that if a torque T_d is applied to the sensor rotor at the frequency ω_o a gradient error signal appears at the sensor output due to the arm inertia mismatch. The peak magnitude of this error is

$$\Gamma_\epsilon \left(\frac{I_1}{B - A}\right)\left(\frac{T_d}{I_c + 2I_1}\right)\left(\frac{\beta_o^2}{\omega_o^2 - \beta_o^2}\right) k_\beta$$

This can also be written

$$\Gamma_\epsilon = \left(\frac{k_\beta}{\eta}\right)\left(\frac{T_d}{I_c}\right) \frac{\beta_o^2 / \left(1 + \frac{2I_1}{I_c}\right)}{\omega_o^2 - \beta_o^2}$$

or since T_d/I_c is the angular acceleration of the rotor case α,

$$\Gamma_\epsilon = \left(\frac{k_\beta \alpha}{\eta}\right) \frac{\beta_o^2 / \left(1 - \frac{2I_1}{I_c}\right)}{\omega_o^2 - \beta_o^2}$$

where:

Γ_ϵ = sensor output error in EU

k_β = sum-mode mismatch factor $\Delta I/I$, 10^{-6}

ω_o = sensor difference mode frequency

β_o = sensor sum-mode frequency

η = sensor arm inertia efficiency, 0.861

I_1 = polar moment of inertia of one sensor arm, 35610 gm cm^2

I_c = rotor case polar moment of inertia not including the arms, 132700 gm cm^2

α = angular acceleration of the rotor case

If it is assumed that the sensor, nonrotating, is oscillated on a test fixture so that accelerometers 1.5 feet from the center have an output of 5×10^{-3} g at a frequency of ω_o then the angular acceleration at the center of the test fixture will be

$$\alpha = \frac{Ag}{R} = 0.107 \text{ rad/sec}^2$$

Notice that the same drivers and accelerometers are assumed that were proposed for the mass unbalance tests.

If it is further assumed that $\omega_o/\beta_o = 2$, which is near the design value, the output signal will be

$$\Gamma_\epsilon = 27.6 \text{ EU}$$

This is a substantial signal and the sensor can easily be adjusted to $k_\beta = 10^{-7}$ as previously suggested.

d. Mass — Unbalance Limits Based on Linear Vibration Estimates

Theoretically, the only vibration frequencies that introduce $2\omega_s$ torques due to arm mass unbalance of the RGG are those at ω_s and $3\omega_s$.

The RGG errors due to differential arm-mass-unbalance are derived in detail in another section of this report. Using this analysis and the best current estimates of the vibration power spectral density (PSD) stable platform we find

$$\text{PSD at } 17.5 \text{ Hz} = 4.5 \times 10^{-9} \text{ g}^2/\text{Hz}$$

$$\text{PSD at } 52.5 \text{ Hz} = 8.9 \times 10^{-10} \text{ g}^2/\text{Hz}$$

Based on our contractually specified integration time of 10 seconds the equivalent noise bandwidth is 0.05 Hz. Substituting these into the reference equation 33, the standard deviation of the acceleration is

$$\sigma_{\text{accel}} = 1.16 \times 10^{-5} \text{ g}$$

This vibration level estimate is quite low and we believe the RGG sensor should operate in a more severe environment. We estimate that the vibrational power spectral density could be as much as 10 times as high as the values shown and thus the acceleration could be

$$\sigma_{\text{accel possible}} = 3.68 \times 10^{-5} \text{ g}$$

The reference shows in equations 34 and 35 that the gradient tensor error terms due to arm mass are, with specific but reasonable assumptions:

$$\sigma_{ij} = \frac{\sigma_a \, g(\Delta mh)}{2\eta C}$$

$$\sigma_{ii} = \frac{\sigma_a \, g(\Delta mh)}{\sqrt{3}\eta C}$$

Assuming a mass unbalance term of $(\Delta mh) = 4 \times 10^{-4}$ gm cm; $\eta C = 30$, 660 gm cm^2; and the hypothesized worst case vibration environment the tensor error terms are:

$$\sigma_{ij} = 0.235 \text{ EU}$$

$$\sigma_{ii} = 0.272 \text{ EU}$$

Thus a (Δmh) mass unbalance of 4×10^{-4} gm cm in the worst case hypothesized environment with the RGG mounted on the specified vibration isolation system produces an acceptable uncertainty level.

e. Arm Mass Balance Stability Expected

The arm mass balance can be expected to change slightly due to temperature shifts, temperature cycling, temperature gradients, and creep. It has been shown that the mass unbalance can be adjusted to values well below the design limit of 4×10^{-4} gm cm. The following paragraphs discuss the problems of maintaining the unbalance to this limit.

If the halves of the arms grow unsymmetrically and differ by 10^{-6} inches the unbalance would be

$$(\Delta mh) = 20 \times 10^{-4} \text{ gm cm}$$

Thus, the balance tubes can accommodate only 1.4 microinches differential arm growth. The importance of material stabilization before assembly is obvious.

Little is known about material creep in the fraction of microinch region, but we would not expect such stability over periods of more than a few days. Also with each cool-down and warm-up we can expect shifts of this magnitude. Thus, we can expect to do a mass unbalance trim on each warm-up.

It should be recognized that it is quite unlikely that we can mass balance the sensor by vibrating when it is nonrotating and have this same mass unbalance when rotating to better than about $\pm 4 \times 10^{-4}$ gm cm.

One guide to the type of mass stability that we can expect can be derived from the characteristics of the Autonetics G-9 gyro. This gyro has a rather large free rotor on a spherical air bearing. The rotor is beryllium with a high density ring. In addition, one copper cup and one manganin cup are attached to the rotor. This rotor is at least comparable to the RGG rotor. Autonetics quotes the axial mass unbalance repeatability of this gyro as 0.01°/hr/g. Other data are

$$I = 1650 \text{ gm cm}^2$$

$$H = 2.5 \times 10^6 \text{ gm cm}^2/\text{sec}$$

$$k \approx .2 \text{ cm (estimated)}$$

$$\text{mass} = I/k^2 = 1650/4 \approx 400 \text{ gms}$$

$$\text{Unbalance torque} = H \times \text{drift rate}$$

$$= 0.125 \text{ dcm}$$

$$= 1.25 \times 10^{-4} \text{ gm cm in a one g field}$$

The mass unbalance ration will be approximately a linear function of mass for a device of this type so we can expect about 4 times the unbalance they expect. That is, the mass unbalance stability we can expect in our sensor comparing it to the Autonetics G-9 gyro is

$$5 \times 10^{-4} \text{gm cm}$$

Thus we seem to have reasonable expectations for the RGG.

Another comparison was made with a Bell Aerosystems gyro. This is also a relatively large gyro. In addition to the inertia wheel the Bell gyro has a spin motor stator on the sensitive element. Bell quotes 0.05°/hr/g shifts from warm-up to warm-up but states that the gyro will not exceed 0.003°/hr/g from its initial value in any one warm-up. Thus Bell has high initial shifts but expects excellent stability for each warm-up.

Another calculation that is important in the mass unbalance stability estimation is that due to the effects of temperature gradients. The effective length of the arms is approximately 5 inches. The total cross section is approximately 0.5 x 2.125 in. sq. The thermal expansion coefficient for aluminum is approximately 20×10^{-6} cm/cm/$^{\circ}$C and its thermal conductivity is 0.37 cal/cm$^{\circ}$C sec. The thermal resistance of the arm is

$$R_{th} = \frac{\rho \ell}{A} = 1.2^{\circ}\text{C/watt}$$

If there is a uniform temperature gradient along the arm the mass unbalance due to a 1°C difference will be that due to the average temperature of one half the arm being $1/2^{\circ}$C hotter than the other half. The hot half will expand and shift 1/2 the mass of the arm to produce an unbalance of

$$\Delta mh = \frac{\ell}{2} \frac{m}{2}$$

$$= 800 \times 10^{-4} \text{ gm cm}$$

If we wish to limit this mass shift to 2×10^{-4} gram cm then the temperature difference between the two ends must not exceed

$$\Delta T = 0.0025^{\circ}C$$

Since the thermal resistance is $1.2^{\circ}C$/watt this limits the power flow through the arm to

$$P \approx 0.002 \text{ W}$$

We can expect the power flow into the balance tubes ($\sim$0.008 W) to cause a small thermal mass unbalance transient.

f. Conclusion

It has been shown that the arm mass and inertia unbalance can be adjusted to acceptable values for the worst case expected environment. It is shown that similar devices in similar environments maintain mass unbalance shifts to the limits required by the RGG. Thus the RGG is expected to meet its accuracy specification in the expected environment.

4. Vibrational Motion Environment Estimates

Estimates of both the translational and angular vibration environment are necessary for determining design parameters of both the RGG sensor and the VIALS (Vibration Isolation, Alignment and Leveling System).

As stated in our proposal, we have selected the airborne application as being the most critical. The choice has been somewhat arbitrary, however it is felt that the vehicle motion environment for the airborne application is generally likely to be as severe as for a surface ship or a submarine. Differences between each vehicle's environment may exist as regards the specific details such as the frequency distribution of vibrational power.

The RGG sensor is sensitive to specific narrow-band frequencies of translational vibration which are related to its design rotational speed. The sensor speed can be varied somewhat to avoid operation at or near large resonant peaks in a particular vehicle's vibration spectrum. The sensor is also sensitive to any and all frequencies of angular vibration normal to its spin axis and is independent of its design rotational speed. However, the angular vibration transmitted to the sensor via its angular isolation system is somewhat unrelated to the vehicle's environment. The purpose of the VIALS is to provide attitude stabilization and to isolate angular rate inputs to the sensor. Its own design characteristics are as dominant in determining the angular vibration inputs as is the vehicle's exact angular rate power spectrum.

We have attempted to obtain motion environment data for submarines and ships and as yet have not been able to obtain such data. We have, therefore, proceeded to generate design requirements for the sensor and VIALS based on vibration data for the KC-135 aircraft. It is felt that this approach, while partially one of expediency, is probably conservative and will result in a sensor and VIALS design which will certainly typify designs for other vehicle applications. Our goal has been and will continue to be one of providing a design suitable to any application. Realizing that any design must be tailored to some extent to its particular application, we will have the flexibility to vary the sensor spin speed to accommodate different vibration spectrums. In addition, the VIALS system's ability to provide appropriately low levels of angular vibration is to some extent independent of the environment. As additional vibrational motion data for other vehicles becomes available, it will be compared to our KC-135 data and the system's ability to accommodate such other environments will be determined.

a. KC-135 Vibration Data

Several references have been used to glean the necessary translational and angular vibration spectral data. They are:

(1) "Summary of Power Spectral Results — KC-135 AF55-3118 Flight Fatigue Program," Boeing Co. Report D6-7102, June 1962.

(2) "Environmental Vibration Measurements on Components of the AN/ASQ-92 Subsystem on the KC-135 Airplane" Boeing Co. Report T6-3604, August 1966.

(3) "KC-135 Power Spectral Vertical Gust Load Analysis," Volume I, Boeing Co. Report D6-18252 July, 1966 (AFFDL TR-66-57).

(4) "Measurements of the Motions of a Large Swept-Wing Airplane in Rough Air" by R. H. Rhyne, NACA TN4310 September 1958.

The data of reference (2) above was used to obtain both translational and angular vibration data in the range of frequencies above 20 Hz. This report documents results of a flight test evaluation of a camera mount subsystem for the reconnaissance airplane. The flight condition was a level flight at M = 0.80 and 35,000 ft altitude. The test was conducted "during a photographic flight condition considered typical by flight crews" according to the report.

The data of reference (1) above was used to obtain the translational vibration power spectrum in the 0 to 10 Hz range. Since the purpose of these tests was to measure flight fatigue properties of the aircraft, severe flight conditions were sought for the tests. The r.m.s. gust velocities for the tests from which our data is taken was 5.38 ft/sec. Hence the power spectral densities were scaled down, per the techniques described in the foregoing reference (4), to simulate a 2.0 ft/sec r.m.s. gust velocity. The 2 ft/sec r.m.s. gust velocity is classified as a "mild turbulence" condition which should typify flight conditions for airborne gravimetry. This scaled down translational vibration data was also used to generate angular vibration data in the 0 to 10 Hz frequency range. This was done by making use of the aircraft's mass and aerodynamic properties of reference (3) above and techniques of reference (4) above to transform aircraft c.g. normal acceleration into aircraft pitch rate data.

Generally, the high frequency data (< 20 Hz) showed similar angular and translational data for all three (x, y, z) axes. Only aircraft normal (vertical) translational acceleration data was available

from reference (1) above. It is normal to expect that aircraft lateral and longitudinal translational accelerations in the lower frequency range will be no more severe than normal acceleration. Similarly, low frequency yaw and roll motion would be expected to be no more severe than pitch motion for an autopilot-controlled large aircraft such as the KC-135. Hence, for purposes of gradiometer and VIALS design, we have assumed the same vibrational power spectrums for all three angular and translational axes. This assumption is also justified because the gradiometer must perform in any spin-axis orientation.

The translational and angular vibration power spectrums from references (1) and (2) above were plotted and the spectrums for frequencies between 10 and 20 Hz, for which no data was available from the references, were approximated by fitting smooth curves to the overall data. The resultant data are shown as the solid lines of Figs. 10 and 11.

b. Inertial Platform Base Motion Spectra

Having established estimates for the vehicle motion environment, estimates were also needed for the vibration levels at the base of the inertial platform. As per our September 1971 proposal, a passive vibration isolation mount is envisioned to serve primarily the purpose of attenuating the translational vehicle vibration and secondarily to attempt to isolate angular vibrations into the inertial platform. Preliminary estimates of vibration attenuation performance of the base motion isolation system were made. The resulting translational and angular vibration power spectra occurring at the mounting base of the inertial platform are shown as dashed lines on Fig. 10 and Fig. 11. Note that at the sensor critical frequencies, its spin frequency (17.5 Hz) (ω_s and $3\omega_s$ are the sensor critical frequencies as regards its error caused by arm mass unbalance) the vibration power level is attenuated by approximately 2.5 orders of magnitude. Due to mass unbalance coupling (i.e. center of mass of base motion isolation

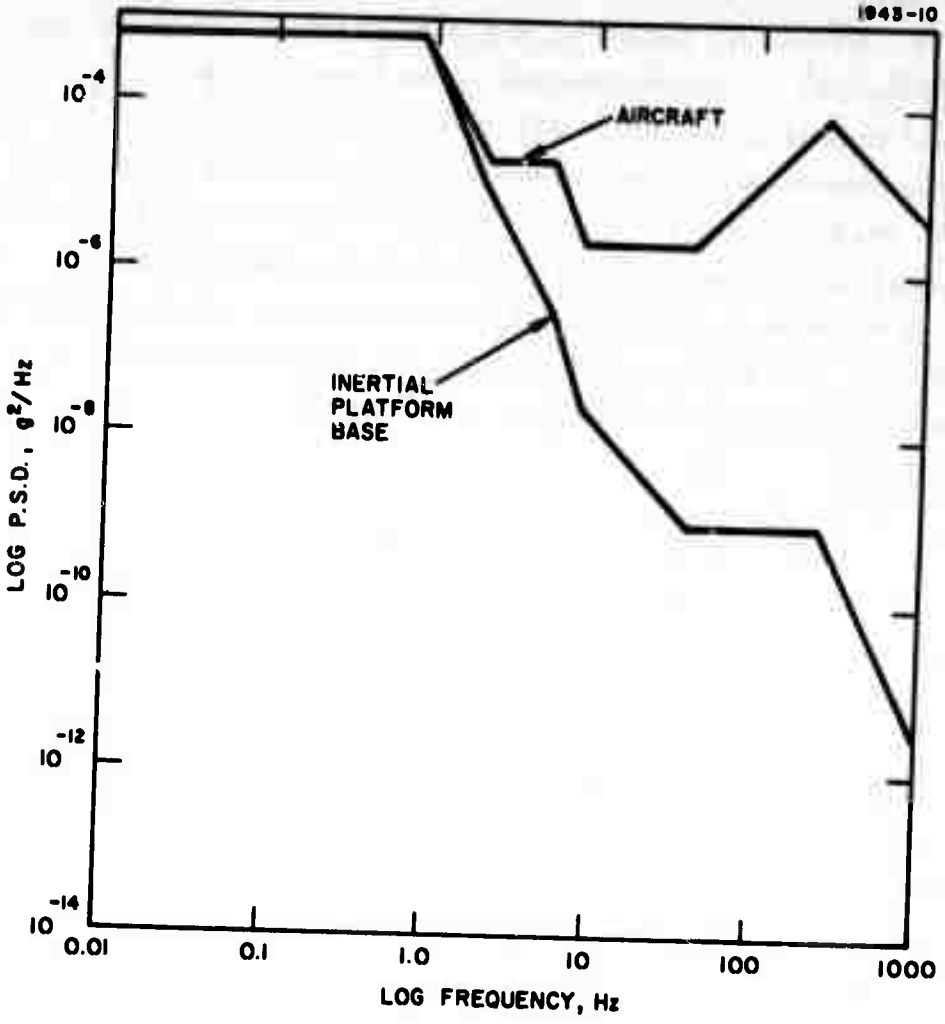

Fig. 10. Acceleration-Power Spectra.

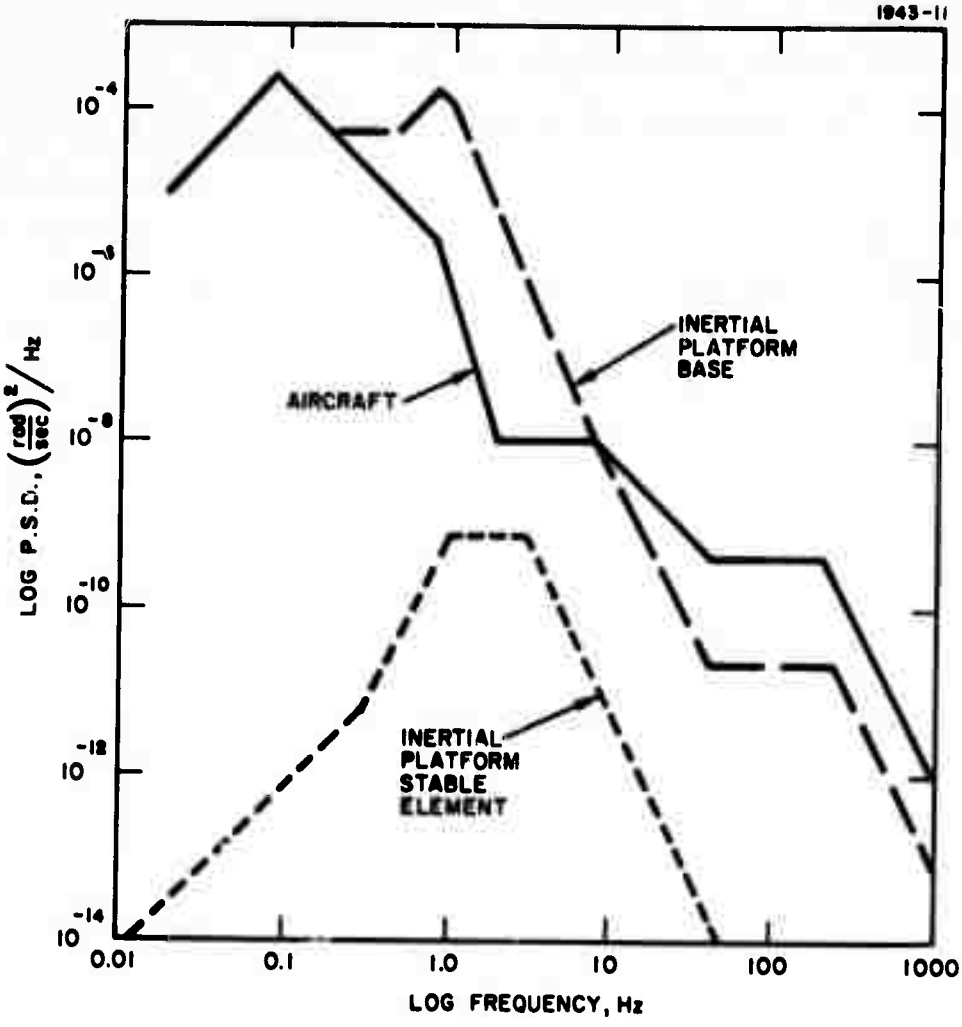

Fig. 11. Angular Rate Power Spectrum.

system's payload not coincident with its elastic spring center) the angular rate power at the inertial platform base is slightly above the aircraft power levels up to 8 Hz, however at the higher frequencies, angular rate power is attenuated. This result is not considered to create a serious problem since the region of amplification is within the servo bandwidth of the inertial platform.

c. Inertial Platform Stable Element Motion Spectra

Estimates of the vibration environment of the platform stable element are also required. For a first preliminary estimate, the translational vibration spectra for the stable element has been assumed to be the same as for the base. Obviously, this is not precisely true since the platform gimbal structure will have vibration resonances which will alter the base spectra somewhat. Any such resonances will have to be controlled by specifying appropriate vibration transmission characteristics of the inertial platform.

A preliminary estimate of the angular vibration spectra of the stable element has been made. Several sources of angular rate excitation were investigated. These included angular disturbance torques caused by:

(1) Gimbal mass unbalance

(2) RGG Sensor case mass unbalance

(3) Friction torque disturbance.

Our estimates for both of items 1 and 2 above resulted in negligible angular rate contribution. However, the friction torque disturbance did prove to be a problem.

First, there is no known simple analytical method for determining the angular transfer function between base and stable element angular rate power spectra. This is due to the stick-slip nonlinearity characteristic associated with the conventional ball bearing supported platform gimbals. We have, for a preliminary estimate, used a simplified method which isolates this non-linearity outside the platform's servo stabilization loop, which is not exact. Other methods of analyzing this problem exist but are very time consuming and expensive

since they all would involve setting-up special computer simulations. The results of our simplified analysis are shown as the dotted line in Fig. 11. The accuracy of this result is not known but it is probably somewhat unconservative. It is interesting to note that if the RGG sensor were hard mounted to the platform stable element, the resulting rotational field error, based on our simplified estimate, would be only 2.5 EU.

d. Additional Angular Isolation Needed

Based on the above simplified analysis, it is obvious that additional angular isolation is needed to meet the overall specified accuracy of 1 EU. There are two basic approaches to providing such additional angular isolation. One would involve providing an additional stage of isolation between the platform stabilized element and the sensor. Several configurations of systems which could perform such a function are described elsewhere in this report. The second approach would be to improve upon the isolation performance of the gimbaled inertial platform. The above simplified estimates were based on ball type gimbal bearings, whose payload capability was assumed to be 200 lbs and whose friction torque level was 10 inch-ounces. If the friction torque were reduced by utilizing hydrostatic gas gimbal bearings, it appears that a suitable reduction in friction could be achieved which would provide adequate performance.

5. Preliminary Gradiometer Designs

Prior to and during the preparation of our September 1971 proposal, much consideration was given to configuring a gradiometer which would provide for isolation of angular vibrations from the rotating sensor arm pair, thus providing a reduction of the inherent rotational field errors of the gradiometer. The need for such isolation had been anticipated at that time. Our analyses of the vehicle motion

environment in Section III-C-4 demonstrates the desirability of providing such isolation. After considering many alternative schemes for supporting the rotating arm pair in such a way as to provide adequate angular vibration isolation, we recommended the neutrally buoyant rotating sphere in our September 1971 proposal. However, practical details of the design had not been studied in depth.

Realizing that many of the other alternate schemes also appeared practical and potentially feasible, we first decided to study some of the important design details of the neutrally buoyant rotating sphere to ascertain if it was truly a practical and feasible mechanization approach. The study of such details, e.g., ease of manufacturing and assembly, centering of the sphere, signal and power routing, etc. resulted in a preliminary design of the configuration. These design details, including sketches of the system are summarized at the end of this section as configuration "A" (Fig. 12). Briefly, it became apparent that this configuration, although feasible to build, would have some very difficult assembly and fluid filling problems. Also, although our brief computer simulation results indicated it would provide what appeared to be adequate angular isolation, we were reticent to fully accept these results since there is general lack of understanding of the behavior of rotating fluids. For the above reasons, we then considered other alternatives and prepared similar preliminary designs for two additional sensor/angular isolation configurations. These two configurations, "B" and "C" (Figs. 13 and 14), have a common concept which differs from configuration "A". In configuration "A", the sensor spherical "float" rotates and thereby the angular isolation occurs in the spinning frame. As such, the long time average angular orientation of the sensor arms is maintained in precise alignment with the sensor spin bearing via the self aligning characteristics of the system. That is, the sensor float is designed to have its axis of maximum moment of inertia aligned along the torsional axis of the sensor arms.

As such, the gyroscopic and viscous torques of this system cause the sensor arms to rotate about this preferred axis.

In configurations "B" and "C", the sensor arms and case rotate in the spin bearing and the angular isolation is provided by supporting the spin bearing stator on a two degree-of-freedom mounting system. Thus, the angular isolation occurs in the non-spinning frame. Gyroscopic torques still tend to provide angular stabilization but the system has nutation instabilities and is subject to mass unbalance and other disturbance error torques. Thus, some form of angular restraint is necessary to provide the required long term angular stabilization.

In configuration "B", the two-axis suspension is provided by a ring gimbal very similar to that of a two degree-of-freedom gyro. Both flexural pivots and journal-type hydrostatic gas bearings were considered for the gimbal bearings. It was found, however, that flexural pivots were not appropriate. This was because the torsional spring rate had to be so low, to accomplish the required angular isolation, that pivots could not be designed to support the load. Sketches depicting configuration "B" are shown at the end of this section.

In configuration "C", the two-axis suspension is provided by a set of four spherical-segment hydrostatic gas bearing thrust pads. The pads are located at the surface of a spherical housing encasing the sensor and spin bearing and positioned at the corners of a circumscribed equilateral tetrahedron. This suspension provides an isoelastic support for the sensor. The suspension is restrained to have only two rotational degrees of freedom about axes normal to the sensor spin-axis by a system of restraint wires as depicted in the sketches of configuration "C" at the end of this section.

A comparision chart, shown in Table III, summarizes the various tradeoffs considered in comparing these preliminary designs. For purposes of program continuity and organization, we have continually carried along a particular sensor configuration as the baseline to provide a common ground for analysis and design of the various sensor

TABLE III

Candidate Configuration Comparison

Table I — Candidate Configuration Comparison

Criteria	Configuration "A" Rotating Liquid-Floated Sphere	Configuration "B" 2-Axis Air Bearing Gimbal	Configuration "C" Restrained Tetrahedron Air Pads
1. Angular isolation capability	- Adequate. Difficult to analyze performance due to uncertainty in the behavior of rotating fluids.	- More than adequate. Lends itself to straightforward analyses. May require servo control.	- More than adequate. Lends itself to straightforward analysis. May require servo control.
2. Angular alignment capability	- Angular phase error about spin-axis might require use of pick-off and torque to control phase error. - Angular alignment about axis normal to spin-axis inherently automatic, however, alignment dependent upon case mass balance. (See case mass balance.)	- Angular alignment about spin-axis accurate and straightforward. - Angular alignment about axis normal to spin-axis would possibly require servo control.	- Angular alignment about spin-axis accurate and straightforward. - Angular alignment about axis normal to spin-axis would probably require servo control.
3. Need for Servo Control	- May need servo to control phase error. Implementation of pickoff and torquer for servo straightforward, however control electronics and power supply would be difficult because of power and signals would have to be transmitted to the rotating members.	- May be necessary. Implementation of pickoffs and torquers for servo would be straightforward.	- May be necessary. Implementation of pickoffs and torquers possible but not as straightforward as "B"
4. Sensor Can Mass Balance	- Mass balance of float difficult because: 1. Float would have to be suspended in temperature-controlled fluid. 2. Dynamic balance of float to bring principal axes into coincidence with sensor torsional axis difficult (No known technique has yet been established). 3. Required expansion bellows causes C.G. shifts.	- Rotor static and dynamic mass balance straightforward.	- Rotor static and dynamic mass balance straightforward.
5. Overall Size	- Upper limit of density of practical flotation fluids of 1.6 grams/cc forces float size to larger package than necessary to house sensor.	- Smaller than "A" but slightly larger than "C" due to larger size required for suitably stiff gimbal ring and gimbal air bearings.	- Smallest

TABLE III

Candidate Configuration Comparison (Continued)

Table 1 – Candidate Configuration Comparison (Continued)

Criteria	Configuration "A" Rotating Liquid-Floated Sphere	Configuration "B" 2-Axis Air Bearing Gimbal	Configuration "C" Restrained Tetrahedron Air Pads
6. Piece-put fabrication	- Layer number of precision piece parts, however generally straightforward.	- High precision required on gimbal air bearings.	- High precision required on stator spherical surfaces.
7. Assembly	- Extreme difficulty of assembly: 1. Delicate handling required to assemble centering spring to float and housing, requiring temperature control of fluid and extreme care to avoid breakage of spring. 2. Sealing of both float and rotating housing required. 3. Nuisance of handling flotation fluid.	- Straightforward assembly.	- Straightforward assembly.
8. Relative Cost	- Hardware cost highest because of mass balance and assembly difficulties.	- Hardware cost similar to "C", except possibly higher due to precision machining and assembly tolerances on gimbal bearings.	- Lowest hardware cost. Compliant surface air pads can be cast in place and therefore require precision machining of one spherical surface.

T725

subsystems and serve as a basis for comparison of alternative configurations. At the inception of the program the baseline was configuration "A". As we studied other configurations, it became apparent that configuration "C" was preferred and it was tentatively adopted as the baseline. At the time of changing from "A" to "C", it was thought that "C" could provide the necessary angular isolation while maintaining the required spin-axis alignment by using only passive spring and viscous restraints. We have since performed further analyses on configuration "C" and found that an active servo control system will be required. These analyses are not yet completed or documented. The specific mechanization which the servo control system must take is still under study. Thus, the selection of a baseline configuration must await complete knowledge as to the various tradeoff considerations.

Some thought has been given to the design of the sensor arms, support pivots, and transducer mounting. Detail studies and analyses are now in progress, but are not yet sufficiently complete to state a firm recommended design. A design similar to the one illustrated in the configuration "C" sketch is now under consideration.

a. Neutrally Bouyant Sphere Rotating Gravity Gradiometer

Notes for Preliminary Sketch (General): Almost entirely 6061 aluminum. Stress relieved before final machining. Most screws and balance weights brass which has almost the same coefficient of expansion as aluminum.

(1) Alternate screws and taper pins. Approximately 24 around outer case. Approximately 6 around air bearing.

(2) O-rings. Used as temporary seal only.

(3) Brass balance screws. Their coefficient of thermal expansion almost identical to aluminum and can get adequately low magnetic susceptibility. Will not gall with aluminum.

(4) Spanner nuts each end. Note that lower one provides a gimbal tilt stop that just matches the pivot to float clearance at top. Select top nut for balance. Proper seals not yet provided at these points.

(5) Outer case of float. 6061 aluminum.

(6) Flex leads — 4 required.
(Pivot = Gnd); 1 + Battery; 1 - Battery; 1 Signal; 1 Logic.

(7) Bellows. Can only install at one end. Bellows shown is not adequate.

(8) Spanner nut.

(9) Insulator if needed or desired.

(10) Beryllium copper pivot with aluminum or brass extender. Extender keeps float control centered as temperature varies. This may not be necessary. Pivot itself can be shortened. This will help reduce suspension point shift as temperature varies.

(11) Air bearing rotors.

(12) Flotation fluid. Carbon tetrachloride in present design but there are a number of other possibilities.

(13) May have to change slightly so that we have a half sphere as a cup for half flotation during assembly. Have not provided a good seal yet at this point.

(14) Central plate and central post. 6061 aluminum of course. Make these first and assemble and balance arms and add internal guts to these. Will want to make a handling fixture. The central plate can have large holes, bosses, posts, etc, as required. Internal structure not yet designed.

(15) Fill port with non-locking taper plug. Held in place by spanner nut with hole to accomodate extractor post of plug.

(16) Non-locking taper, centers and levels pivot post.

(17) Batteries. 12 — 0.225 ampere hour, 1.3 volts/cell. Nickel-cadmium. Must be provided with case fixed magnetic shield.

(18) Battery carrier. Visualize batteries epoxy set in an aluminum ring.

(19) Power input capacitor plates.

(20) Stand-off insulators for 19.

(21) Exhaust air deflector attached to main frame.

(22) Air bearing stators attached to main frame.

(23) Backup motor stator iron. Overlaps statur stack to act as magnetic shield.

(24) Motor stator. TranCore T, 0.007 in. thick. Should be able to buy standard punching.

(25) Magnetic leakage shield.

(26) Motor stator mount attached to main case.

(27) Epoxy seals

(28) Float angle pickoff.

(29) Pivot nut with Allen Wrench socket.

b. Neutrally Bouyant Sphere Rotating Gravity Gradiometer

Preliminary design data:

(1) Float

Material		6061 aluminum
Outside Diameter	(6.50 in.)	16.51×10^{-2} m
Inside Diameter	(6.00 in.)	15.24×10^{-2} m
Displaced Vol	(2356 cc)	2.356×10^{-3} m^3
Average density	(1.6 gm/cc)	1.6×10^{-9} kg/m^3
Mass (3770 gms)		3.7 kg

	Polar Inertia	(1.02×10^5 gm cm^2)	1.02×10^{-2} kg/m^2
	Diameter Inertia	(8.0×10^4 gm cm^2)	8.00×10^{-3} kg/m^2
(2)	Arms		
	Mass (Mallory 1000 & Al)	(700 gms)	0.7 kg
	Inertia	(20,000 gm cm^2)	2.0×10^{-3} kg/m^2
	Inertia Efficiency		0.7_r
	Peak Torque, 1 EU Field		7.0×10^{-13} Nm
	Balance Screws		Brass
(3)	Central Pivot		
	Material		Beryllium Copper
	Length, Active	(0.100 in.)	
	Diameter	(0.010 in.)	
	K_t, Torsional St Stiffness	($7.2 \times 10^-$ dcm/rad)	7.2×10^{-3} Nm/rad
	K_b, Bending Stiffness	(9.4×10^4 dcm/rad	9.4×10^{-3} Nm/rad
	Stress when Lifting Float	(106,000 psi)	
	Torsional Freedom	(2.39 deg)	±0.0417 rad
	Bending Freedom	(2.39 deg)	±0.0417 rad
	Max Tension Stress Bend	(34,400 psi)	
	Max Shear Stress Torsion	(~12,000 psi)	
	Hang-Off at 20°/hr Input Rate	(0.61 deg)	0.010 rad

(4) Fluid

Carbon Tetrachloride (tentative selection)

Density, 20°C	(1.6 gms/cc)	1.6×10^{-9} kg/m^3
Viscosity, μ	(0.009 poise)	9.0×10^{-4} Nsec/m^3

Germanium Tetrachloride

Density	(1.84 gms/cc)	1.84×10^{-9} kg/m^3
Viscosity, μ		

Damping Gap, h

Physical	(0.025 in.)	6.35×10^{-4} m
Effective, 10 Hz		2.7×10^{-4} m
Effective, 20 Hz		1.9×10^{-4} m
Effective, 40 Hz		1.35×10^{-4} m

Damping Coefficient

Low Frequency	(5,950 dcm sec)	5.95×10^{-4} Nm sec
10 Hz	(8.340 dcm sec)	8.34×10^{-4} Nm sec
20 Hz	(11,800 dcm sec)	11.80×10^{-4} Nm sec
40 Hz	(16,680 dcm sec)	16.68×10^{-4} Nm sec
Volume of Fluid	(55 cc)	5.5×10^{-6} m^3
Coefficient of Expansion	(1.2×10^{-3} °C)	
Net Volume Change $\Delta T = (124 - 70)$ $= 54°F$ $= 30°C$	(1.8 cc)	1.8×10^{-6} m^3

(5) Natural Frequencies and Damping Ratios

Torsional Undamped	(0.135 Hz)	0.85 rad/sec
Bending Undamped	(0.172 Hz)	1.08 rad/sec
Damping Ratio Torsion	ζ	0.024 (low frequency)
Damping Ratio Bending	ζ	0.034 (low frequency)

(6) Spin Motor Estimates

Excitation Frequency		180 Hz
Number of Poles		12
Synchronous Speed		30 RPS
Stator and Rotor Material		Tran-Core T (.007")
Mass of Iron	(1.83 lbs)	0.828 kg
Mass of Copper	(0.60 lbs)	0.414 kg
Power During Run Up		20 watts
Power During Operation		10 watts
Locked Rotor Torque	(3.0 in.-oz)	2.12×10^{-3} Nm
Running Torque	(0.5 in.-oz)	3.54×10^{-4} Nm

c. **Basic Data For Baseline Configuration**

(1) Mass and Inertia Characteristics of Arms, Rotor, and Stator

	Wt gms	I_{xx} gm-cm^2	I_{yy} gm-cm^2	I_{zz} gm-cm^2
Arm No. 1	1563	4,990	35,610	35,600
Arm No. 2	1563	35,610	4,990	35,600
Rotor (all except arms)	2750	103,400	103,400	132,700
Total Rotor	5876	144,000	144,000	203,900
Stator	3766	289,200	289,200	252,600
Total Rotor plus Stator	9642	433,200	433,200	456,500

Rotor plus Stator Mass Unbalance ≈ 1 gram-cm

Spin Frequency = 17.5 Hz = 110 rad/sec

On-Axis Spring Restraint of Air Pad "Gimbal" - Such that 20°/hr transport and earth's rate produces no more than 1/4 degree.
($K = 2 \times 10^5$ dyne-cm/rad = $H\Omega/\theta$)

Damping Coefficient of Air Pads = 500 dyne-cm-sec

Inertial Platform Friction = 10 in-ozs

Inertial Platform Mass and Inertia Properties

		Radius of Gyration
Payload (incl. stable element)	200#	8"
Middle Gimbal	40#	10"
Outer Gimbal	60#	12"
Core (50 lbs plus top half of isolation mount 50 lbs)	100#	14"

Mass unbalance aim $\frac{T_f}{W} = \frac{10 \text{ in-ozs}}{16 \times 400 \text{ ozs}} = 0.00156$ in

Base Motion Isolation System

Spring arm of mount = 17.5"
Damping ratio for translation = 0.4
Damping ratio for rotation = 1.0
Mass unbalance arm = 0.025 ft = 0.3 in

Sensor Parameters

Difference mode resonant frequency = 35 Hz
Difference mode Q = 300

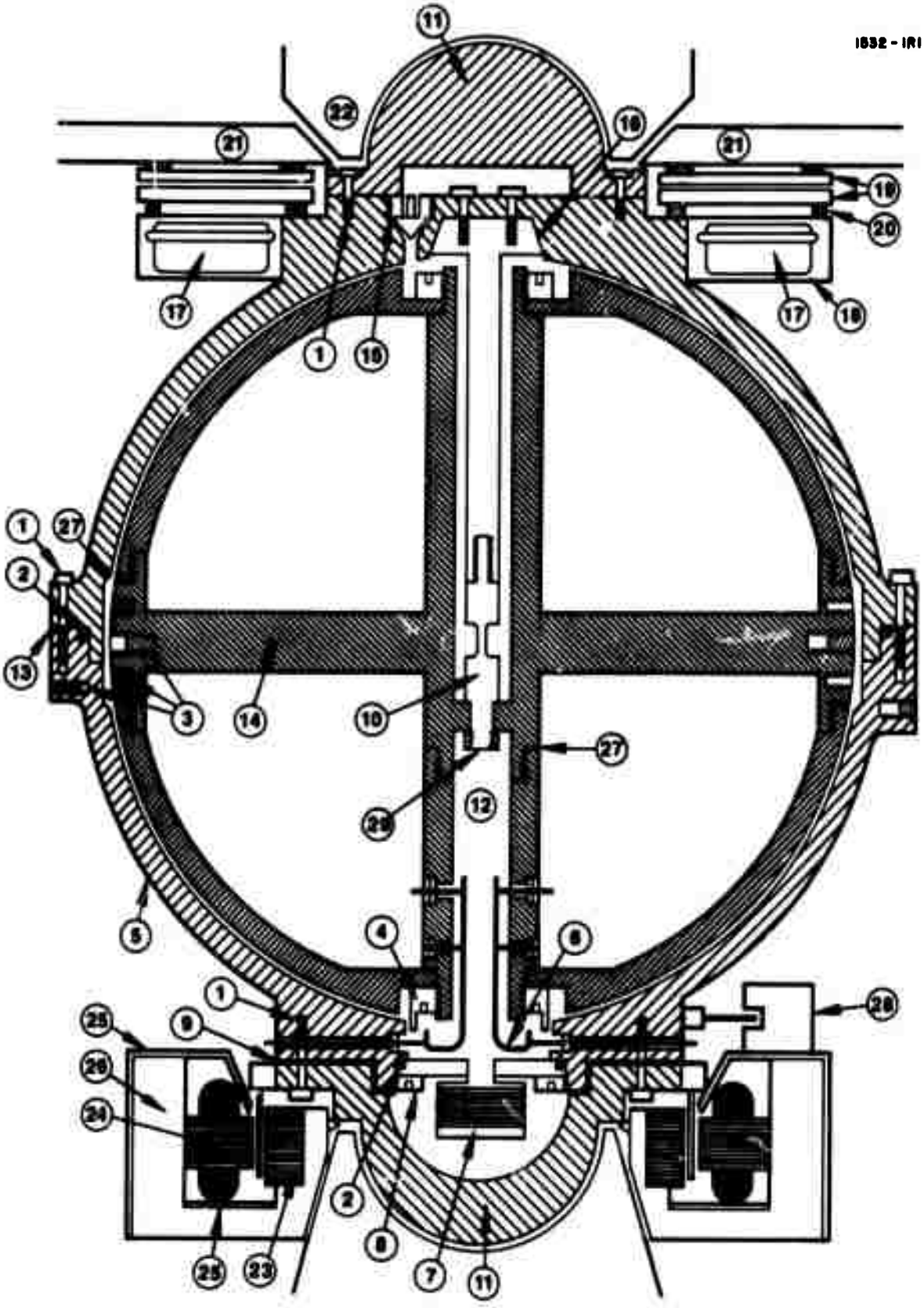

Fig. 12. Configuration "A".

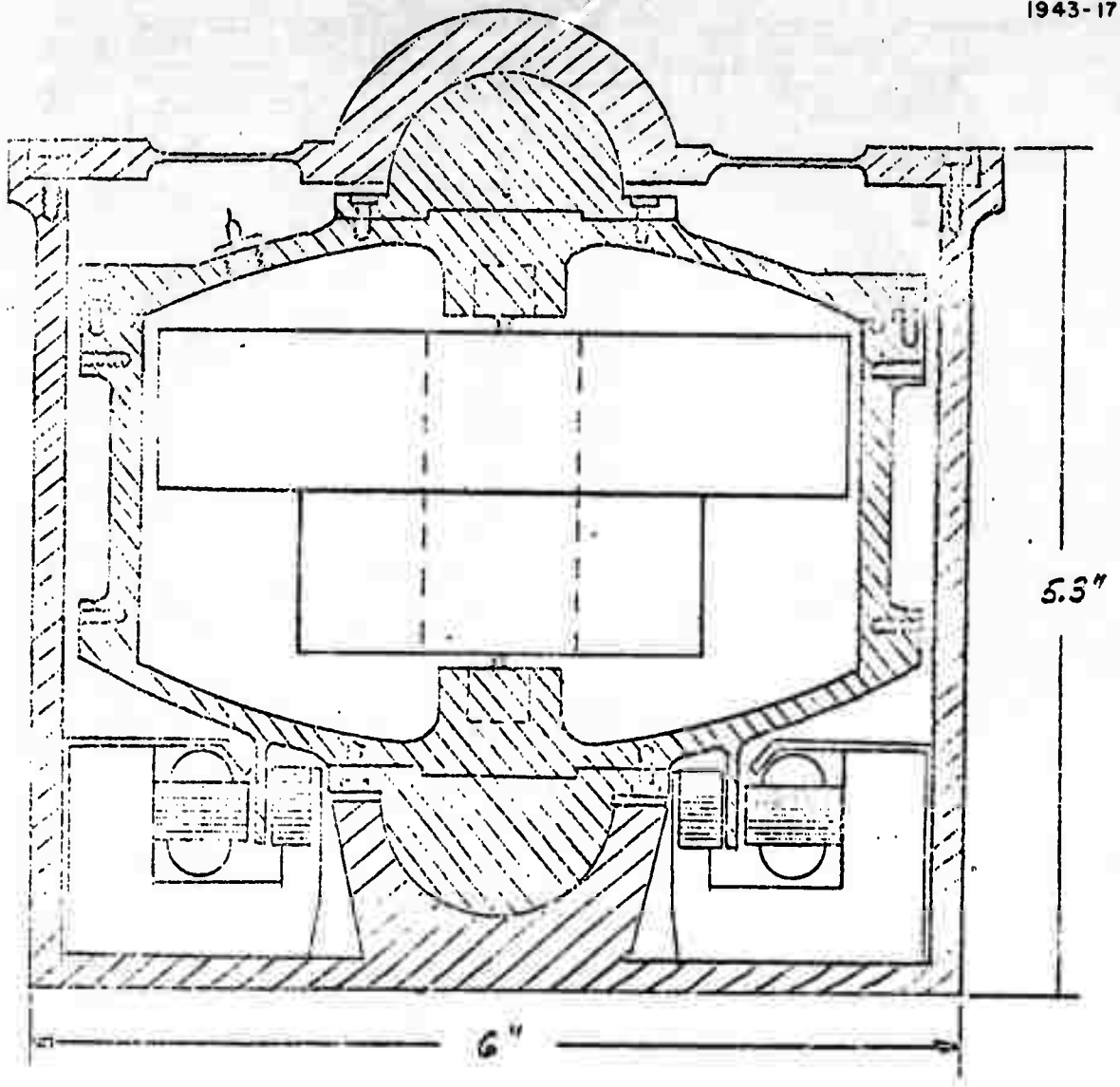

Fig. 13. Configuration "B".

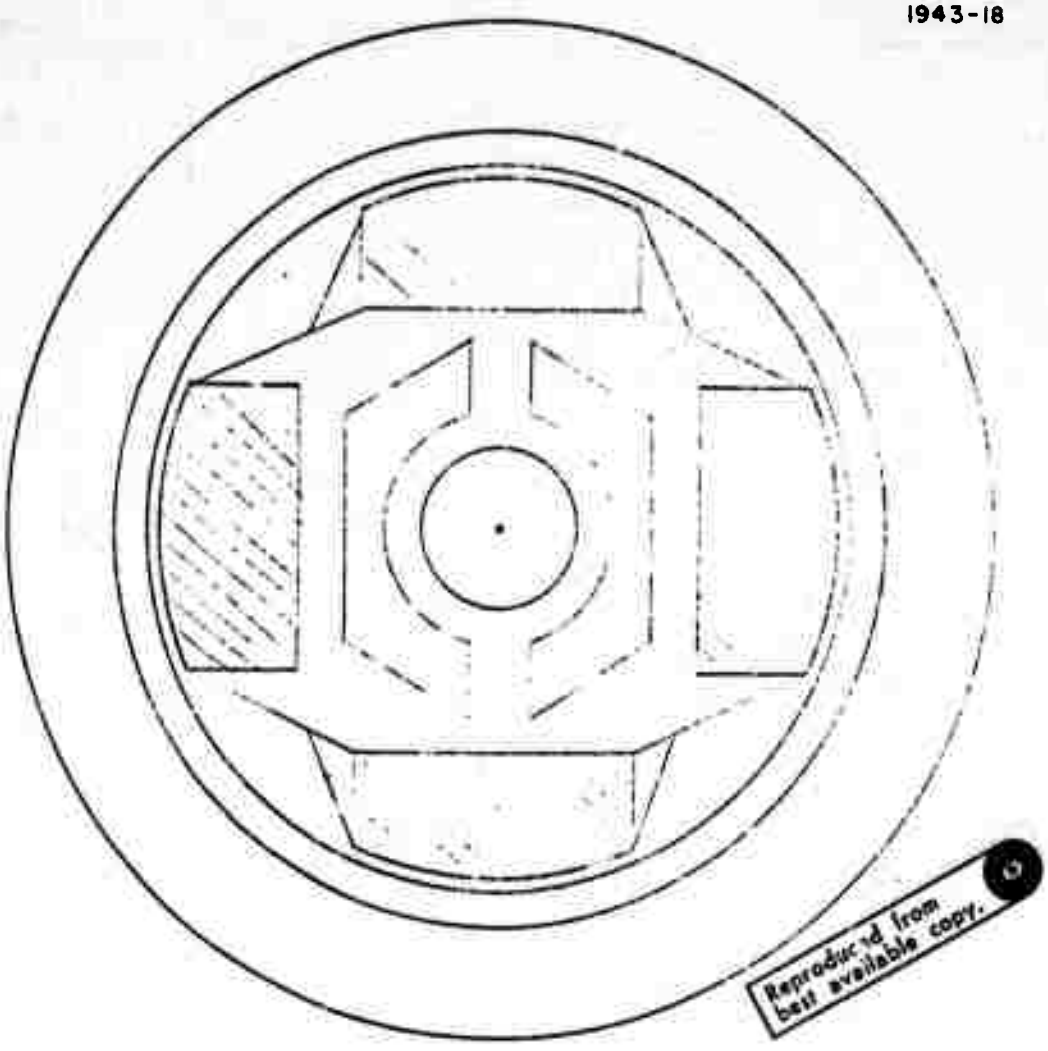

Fig. 13. Sheet 2 of 4.

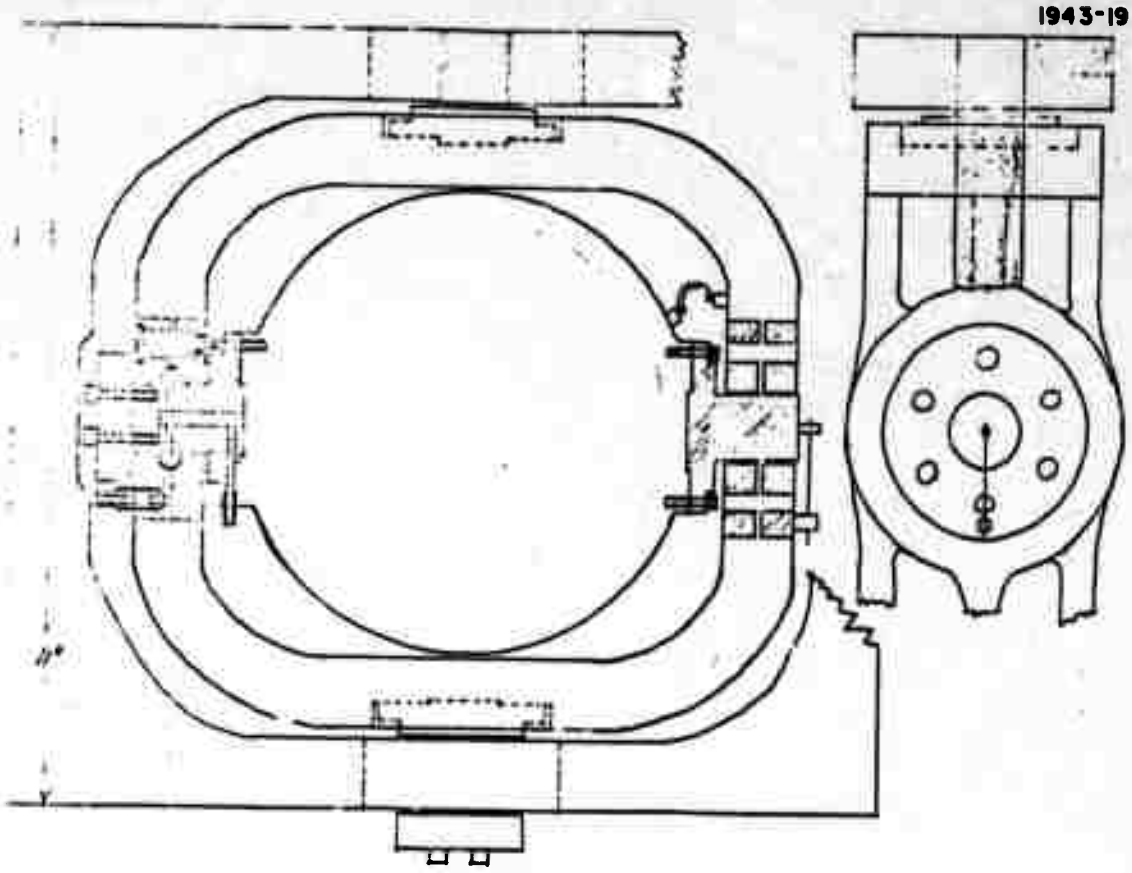

Fig. 13. Sheet 3 of 4.

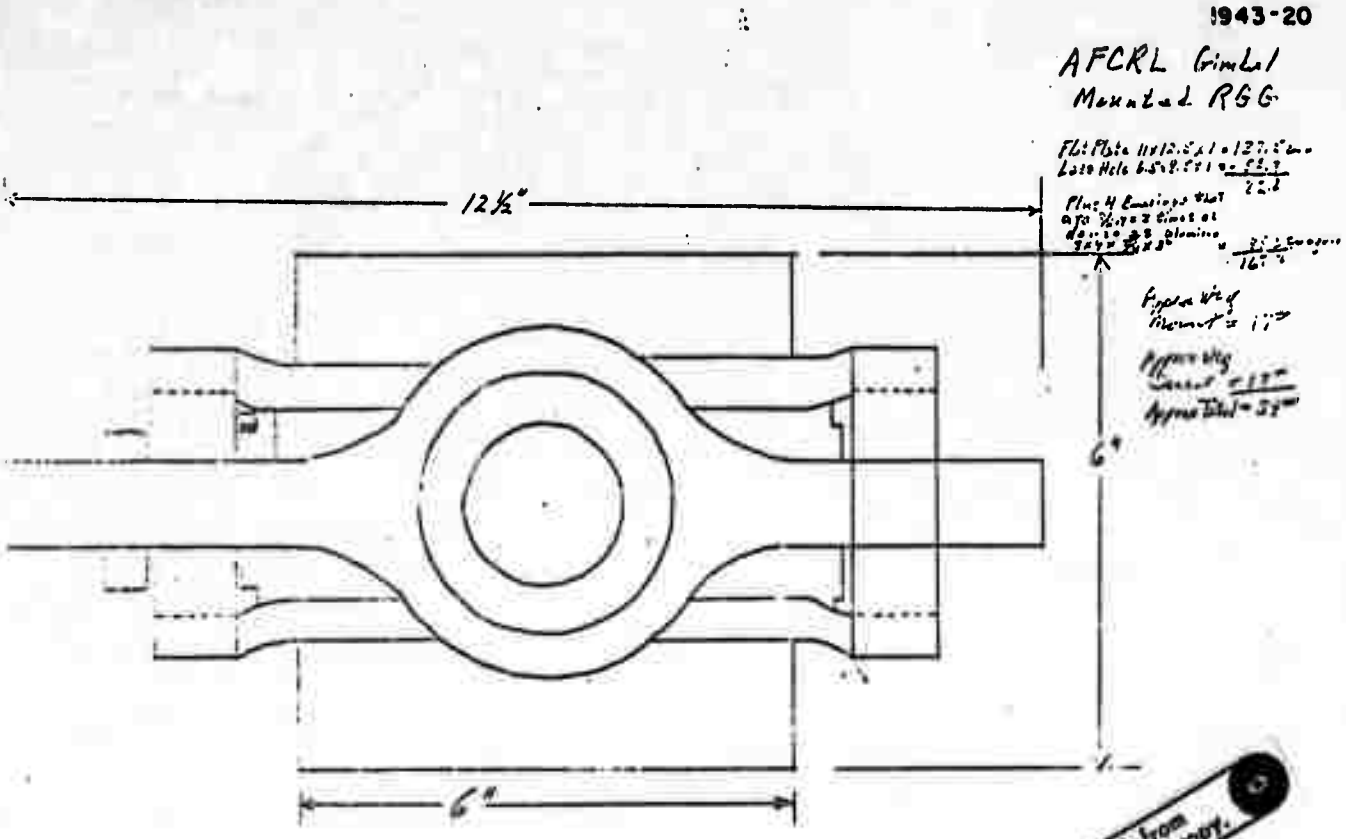

Fig. 13. Sheet 4 of 4.

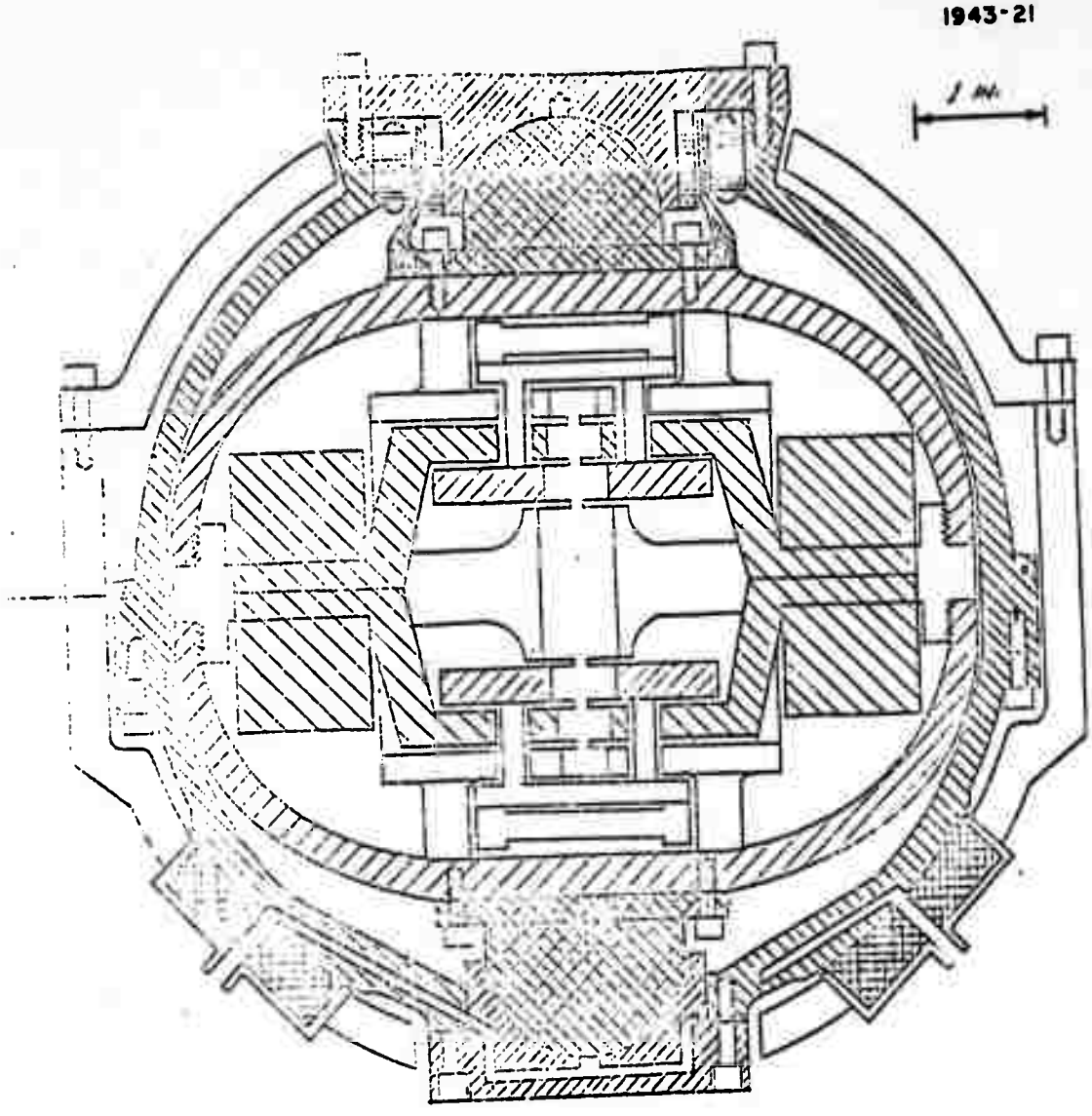

Fig. 14. Configuration "C".

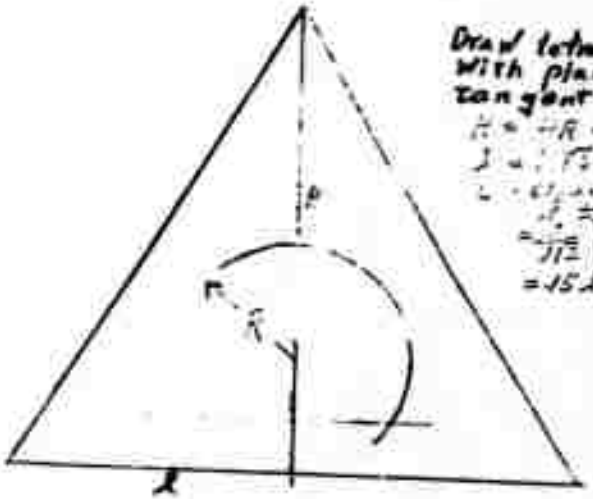

$A = 4R^2\pi$

$V = \frac{4}{3}\pi R^3 = 4.19R^3 = 2.45D^3$

Volume of ball $= \frac{4}{3}\pi R^3\left(1 - \frac{1}{15}\right)$

$= 15R^3$

Cut off corners of tetrahedron tangent to Sphere. Add 4 air ports

Rotate about 2 axes

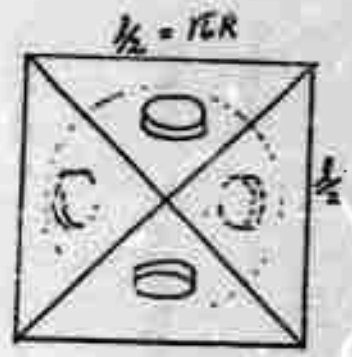

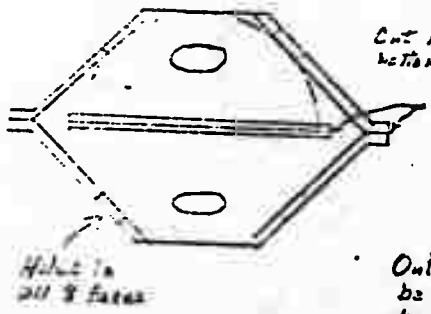

Cut off top and bottom of pyramids.

Parting line for Outer Case and Sunser Spherical Case.

Holes in all 8 faces

Outer Case can also be made spherical to save a little weight and if more convenient.

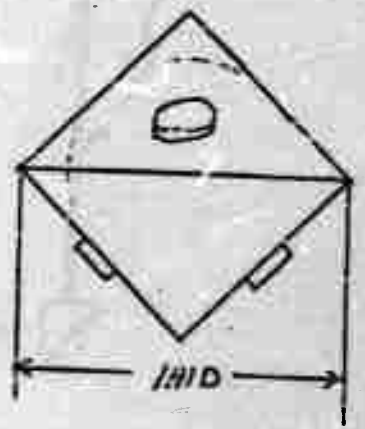

Fig. 14. Sheet 2 of 3.

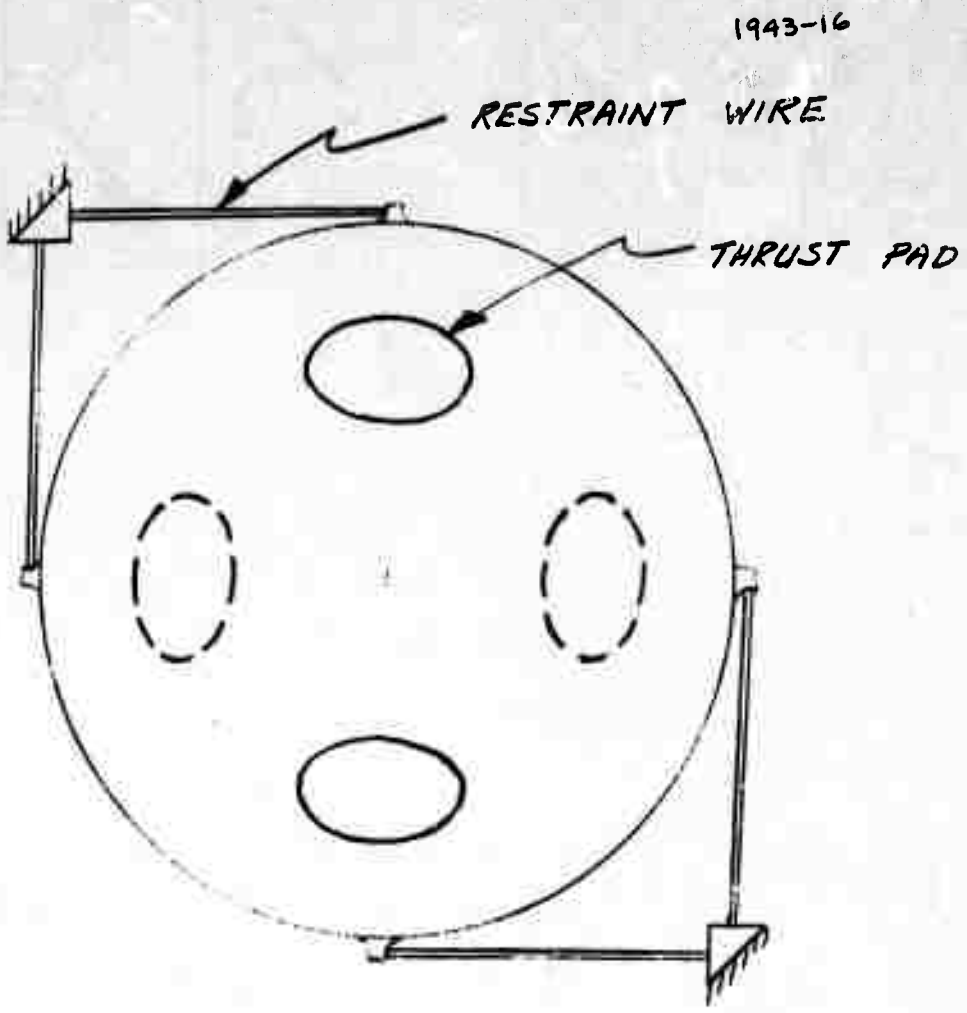

RESTRAINT SYSTEM SCHEMATIC
FOR TETRAHEDRON AIR PAD SENSOR
(CONFIGURATION "C")

Fig. 14. Sheet 3 of 3.

6. Isoelasticity of Spherical Gimbal Support With Hydrostatic Bearing Pads

One possible configuration of the prototype moving-base gravity gradiometer employs a set of four pressurized hydrostatic bearing pads, arranged on the surface of a sphere, to support the gradiometer stator with two degrees of angular freedom for angular rate isolation from the base to which the gradiometer case is mounted. It is desired that the hydrostatic support system be isoelastic under linear acceleration.

It is the purpose of this analysis to show that a particular spherical configuration of four hydrostatic bearing pads will provide isoelastic support. The four pads will be found to be located at the corners of an equilateral tetrahedron inscribed within the sphere.

Consider a pair of initially concentric spheres of radius R and $R - h_o$, with centers at the origin of coordinates, where $h_o \ll R$.

Now let the inner sphere undergo a displacement:

$$\overline{\delta} = \overline{i}\,\delta_x + \overline{j}\,\delta_y + \overline{k}\,\delta_z$$

Then the change in clearance, Δh_p, between the spheres, at any point $P(R, \theta, \phi)$ on the outer sphere, will be given by the negative projection of $\overline{\delta}$ on the radius vector to the point P.

$$\Delta h_p = -\overline{l}_r \cdot \overline{\delta} = -(\gamma_{px}\,\delta_x + \gamma_{py}\,\delta_y + \gamma_{pz}\,\delta_z)$$

Where the γ_{pi} are the direction cosines of the point, P, with respect to the coordinate axes.

If we now assume that a hydrostatic bearing pad centered at any point P produces a radial (i. e., normal to the sphere surface) restoring force, F_p, directly proportional to the change in clearance at P, then:

$$\overline{F}_p = -\overline{l}_r\,K\,\Delta h_p$$

Resolving this radial force along the coordinate axes:

$$\overline{F}_p = - K\Delta h_p \left(\overline{i}\, \gamma_{px} + \overline{j}\, \gamma_{py} + \overline{k}\, \gamma_{pz}\right)$$

Substituting for Δh_p from above and writing the result in matrix form:

$$\begin{pmatrix} F_{px} \\ F_{py} \\ F_{pz} \end{pmatrix} = K \begin{pmatrix} \gamma_{px}^2 & \gamma_{px}\gamma_{py} & \gamma_{px}\gamma_{pz} \\ \gamma_{py}\gamma_{px} & \gamma_{py}^2 & \gamma_{py}\gamma_{pz} \\ \gamma_{pz}\gamma_{px} & \gamma_{pz}\gamma_{py} & \gamma_{pz}^2 \end{pmatrix} \begin{pmatrix} \delta_x \\ \delta_y \\ \delta_z \end{pmatrix}$$

We now have an expression for the force due to a single pad in terms of its direction cosines. This may be written as:

$$F_{pi} = K \sum_j \gamma_{pi}\, \gamma_{pj}\, \delta_j$$

Then, for a system of N pads, at arbitrary locations:

$$F_i = \sum_p^N F_{pi} = K \sum_p^N \sum_j \gamma_{pi}\, \gamma_{pj}\, \delta_j = K \sum_j \left(\sum_p^N \gamma_{pi}\, \gamma_{pj} \right) \delta_j$$

Where the p and j summations have been interchanged. We can now define a set of matrix elements:

$$a_{ij} \triangleq \frac{1}{k} \sum_p^N \gamma_{pi}\, \gamma_{pj}$$

Such that:

$$F_i = \sum_p^N F_{pi} = Kk \sum_j a_{ij}\,\delta_j$$

or:

$$\begin{pmatrix} F_x \\ F_y \\ F_z \end{pmatrix} = Kk \begin{pmatrix} a_{11} & a_{12} & a_{13} \\ a_{21} & a_{22} & a_{23} \\ a_{31} & a_{32} & a_{33} \end{pmatrix} \begin{pmatrix} \delta_x \\ \delta_y \\ \delta_z \end{pmatrix}$$

for the resultant force of N pads. The a_{ij} are the direction cosines of the force vector with respect to the displacement. The isoelasticity condition requires that the force vector be in the direction of the displacement. That is, for isoelasticity,

$$\overline{F} = Kk\,\overline{\delta}$$

which requires that:

$$\begin{pmatrix} a_{11} & a_{12} & a_{13} \\ a_{21} & a_{22} & a_{23} \\ a_{31} & a_{32} & a_{33} \end{pmatrix} = \begin{pmatrix} 1 & 0 & 0 \\ 0 & 1 & 0 \\ 0 & 0 & 1 \end{pmatrix}$$

or

$$a_{ij} \triangleq \frac{1}{k} \sum_{p}^{N} \gamma_{pi}\, \gamma_{pj} = \delta_{ij} = \begin{cases} 1 \text{ for } i = j \\ 0 \text{ for } i \neq j \end{cases}$$

where δ_{ij} is the kronecker delta.

Now consider the specific configuration of four pads on the surface of a sphere of radius, R, such that the direction cosines of the points, P, are as shown below:

Pad	γ_{px}	γ_{py}	γ_{pz}
1	sin ψ	cos ψ	0
2	sin ψ	-cos ψ	0
3	-sin ψ	0	cos ψ
4	-sin ψ	0	-cos ψ

As shown in the sketch below, the four points are at the corners of an inscribed tetrahedron but the value of ψ is as yet unspecified.

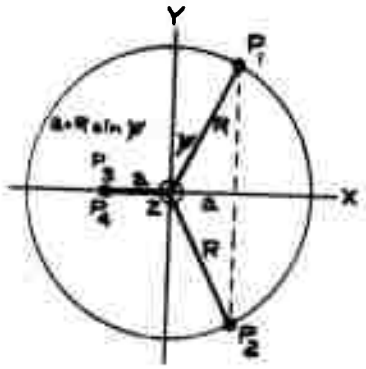

Forming the indicated products and summing over p in the expression:

$$a_{ij} = \frac{1}{k} \sum_{p}^{N} \gamma_{pi}\, \gamma_{pj}$$

The a-matrix becomes:

$$\begin{pmatrix} a_{11} & a_{12} & a_{13} \\ a_{21} & a_{22} & a_{23} \\ a_{31} & a_{32} & a_{33} \end{pmatrix} = \begin{pmatrix} \frac{4}{k}\sin^2\psi & 0 & 0 \\ 0 & \frac{2}{k}\cos^2\psi & 0 \\ 0 & 0 & \frac{2}{k}\cos^2\psi \end{pmatrix}$$

The matrix is diagonal as a result of a fortuitous choice of coordinates. The requirements of the isoelasticity condition, then, are satisfied identically if, and only if:

$$\frac{4}{k}\sin^2\psi = \frac{2}{k}\cos^2\psi = 1$$

or:

$$4\sin^2\psi = 2\cos^2\psi = k$$

From which:

$$\tan^2\psi = \frac{1}{2}$$

$$\tan\psi = \frac{1}{\sqrt{2}} \quad (= \sin 45^\circ)$$

$$\sin\psi = \frac{1}{\sqrt{3}} \quad (= \tan 30^\circ)$$

$$\cos\psi = \sqrt{\frac{2}{3}}$$

and:

$$k = \frac{4}{3}$$

$$\psi \cong 35^\circ\ 16'$$

The resultant restoring force becomes:

$$\overline{F} = \frac{4}{3} K \overline{\delta}$$

It can easily be shown by simple trigonometry (see preceding sketch) that the value of ψ found to be required for isoelasticity is identically equal to that required for the tetrahedron to be equilateral.

It can be shown that an orthogonal set of six pads is also isoelastic under the same conditions. It is interesting to note that, if the orthogonal set is cut by a symmetry plane, such that three of the six pads are on each side of the plane, and such that each of the six radius vectors forms an angle, θ, with the symmetry plane, then the value of θ will be identical to the value of ψ found above for the tetrahedral set (i. e., 35^{o}, 16'). For this six-pad set, the force is given by:

$$\overline{F}_6 = 2 K \overline{\delta}$$

The above results can be extended to show that any set of 2η pads (where η is any integer greater than or equal to 2), with proper symmetry about a symmetry plane, and with each radius vector forming an angle ψ ($=35^{o}$ 16') with the symmetry plane, will be isoelastic. It can further be shown that the resultant force for any such system will be given by:

$$\overline{F} = \frac{\eta}{3} K \overline{\delta}$$

In the limit, as $\eta \rightarrow \infty$, the system would become a pair of rings of radius R cos ψ and separated by a distance 2R sin ψ.

7. Spin Bearing Requirements

Three of the following subsections analyze the gravity gradient errors that could be introduced by the sensor spin bearing. The fourth subsection is the spin bearing specification that is based on the analysis, practical adjustment limits and the expected environment.

a. Gradient Errors Due to Sum-Mode Mismatch

In the rotating gravity gradiometer the arms may rotate in either of two fundamental modes: (1) the sum mode, in which the arms move together relative to the sensor case; and (2) the difference mode, in which the arms rotate relative to each other. It is the difference mode which is excited by the external gravity gradient and which generates an output signal.

In an ideal sensor, spin axis disturbance torques excite only the sum mode and produce no spurious output signal. However, to the extent that imperfection exists in the matching of the sum-mode inertia-spring constants of the arms (sum-mode mismatch), spin axis disturbance torques will excite the difference mode, resulting in a gradient measurement error.

The equations of motion are written as:

$$I_1 S^2 \theta_1 + (D_o S + K_o)(\theta_1 - \theta_2) + (D_1 S + K_1)(\theta_1 - \theta_c) = (B-A)\Gamma_{ij}$$

$$I_2 S^2 \theta_2 + (D_o S + K_o)(\theta_2 - \theta_1) + (D_2 S + K_2)(\theta_2 - \theta_c) = (A-B)\Gamma_{ij}$$

$$I_c S^2 \theta_c + (D_1 S + K_1)(\theta_c - \theta_1) + (D_2 S + K_2)(\theta_c - \theta_2) = T_d$$

for arm 1, arm 2 and the sensor case, c, respectively. D_o, K_o refer to the difference mode pivot and D_1, K_1 and D_2, K_2 refer to the two sum mode pivots. A, B are the arm transverse inertias, Γ_{ij} the gradient input and T_d the spin-axis disturbance torque acting on the sensor case.

Defining:

$$A_o \triangleq D_o S + K_o; \quad A_1 \triangleq D_1 S + K_1; \quad A_2 \triangleq D_2 S + K_2$$

and writing the equations in matrix form:

$$\begin{bmatrix} (I_1 S^2 + A_o + A_1) & -A_o & -A_1 \\ -A_o & (I_2 S^2 + A_o + A_2) & -A_2 \\ -A_1 & -A_2 & (I_c S^2 + A_1 + A_2) \end{bmatrix} \begin{bmatrix} \theta_1 \\ \theta_2 \\ \theta_3 \end{bmatrix} = \begin{bmatrix} (B-A)\,\Gamma_{ij} \\ (A-B)\,\Gamma_{ij} \\ T_d \end{bmatrix}$$

These equations are solved for

$$\Delta\theta = \theta_1 - \theta_2$$

and the result is:

$$\Delta\theta = \frac{\frac{2(B-A)\Gamma_{ij}}{I_1}\left[S^2 + \frac{\beta_o}{Q_\beta} S + \beta_o^2\right] + \frac{T_d}{I_c}\left[\frac{A_1}{I_1} - \frac{A_2}{I_2}\right]}{\left[S^2 + \frac{\omega_o}{Q} S + \omega_o^2\right]\left[S^2 + \frac{\beta_o}{Q_\beta} S + \beta_o^2\right]}$$

where

$$\beta_o^2 \triangleq \frac{K_1}{I_1}\left(1 + \frac{2I_1}{I_c}\right)$$

$$\omega_o^2 \triangleq \frac{K_1}{I_1}\left(1 + \frac{2K_o}{K_1}\right)$$

β_o = sum mode frequency

ω_o = difference mode frequency

Q_β = sum mode Q

Q = difference mode Q

The normalized equivalent gradient output in the presence of disturbance torque, $T_d(S)$, is then

$$(2\hat{\Gamma}_{ij}) = \frac{\frac{\omega_o^2}{Q}}{S^2 + \frac{\omega_o}{Q} S + \omega_o^2} \left[2\Gamma_{ij} + \frac{\left(\frac{I_1}{B-A}\right)\left(\frac{T_d}{I_c}\right)\left(\frac{A_1}{I_1} - \frac{A_2}{I_2}\right)}{S^2 + \frac{\beta_o}{Q_\beta} S + \beta_o^2} \right]$$

and the equivalent gradient output due to spin axis disturbance torque and sum mode mismatch alone is

$$\Gamma_o = \frac{\frac{\omega_o^2}{Q}\left(\frac{I_1}{B-A}\right)\left(\frac{T_d}{I_c}\right)\left(\frac{A_1}{I_1} - \frac{A_2}{I_2}\right)}{\left(S^2 + \frac{\omega_o}{Q} S + \omega_o^2\right)\left(S^2 + \frac{\beta_o}{Q_\beta} S + \beta_o^2\right)}$$

Defining

$$\frac{A_1}{I_1} - \frac{A_2}{I_2} \triangleq k_\beta \frac{K_1}{I_1} = k_\beta \beta_o^2 \left(\frac{I_c}{I_c + 2I_1}\right)$$

$k_\beta \triangleq$ sum mode mismatch coefficient

$$\Gamma_o = \frac{\left(\frac{I_1}{B-A}\right)\left(\frac{T_d}{I_c + 2I_1}\right)\left(\frac{k_\beta \beta_o^2 \omega_o^2}{Q}\right)}{\left(S^2 + \frac{\omega_o}{Q} S + \omega_o^2\right)\left(S^2 + \frac{\beta_o}{Q_\beta} S + \beta_o^2\right)}$$

This expression gives the frequency response of the sensor output signal to spin axis disturbance torques in terms of an equivalent gradient amplitude. Only that portion of the output within the narrow pass band

at the difference mode frequency, ω_o, is interpreted as gradient error. To find the gradient error amplitude due to disturbance torque at the difference mode frequency we evaluate $\left|\Gamma_o\right|$ at $S = j\omega_o$.

$$\Gamma_\epsilon = \left|\Gamma_o(S = j\omega_o)\right|$$

$$\Gamma_\epsilon = \left(\frac{I_1}{B-A}\right)\left(\frac{T_d}{I_c + 2I_1}\right)\left(\frac{k_\beta \beta_o^2}{\omega_o^2 - \beta_o^2}\right)$$

where $Q_\beta \gg 1$ has been assumed. This value of Γ_ϵ differs from previously published values by the factor $(I_1/B-A)$. Representative parameter values for the baseline sensor are:

$I_1 = 35,600$ gm-cm^2

$A = 4,990$ gm-cm^2

$B = 35,610$ gm-cm^2

$I_c = 132,700$ gm-cm^2

$\omega_o = 220$ rad/sec

$\beta_o = 110$ rad/sec

$k_\beta = 10^{-6}$

for which

$$\Gamma_\epsilon = \frac{T_d}{525} \quad \text{E.U.}$$

where T_d is in dyne-cm.

Then, in order to limit sum-mode mismatch errors to less than 0.1 EU, spin axis disturbance torque uncertainties should be held to less than 50 dyne-cm, at the difference mode frequency.

Since the sensor response characteristic also has a high-Q peak at the sum mode frequency, it is necessary to consider limits on spin-axis disturbance torque at the sum mode frequency. The response at the sum mode frequency is:

$$\Gamma_\beta = \left|\Gamma_o(S = j\beta_o)\right|$$

$$\Gamma_\beta = \left(\frac{I_1}{B\text{-}A}\right)\left(\frac{T_d}{I_c + 2I_1}\right)\left(\frac{Q_\beta}{Q}\right)\frac{k_\beta\,\omega_o^2}{\omega_o^2 - \beta_o^2}$$

Then the two response amplitudes are in the ratio

$$\frac{\frac{\Gamma_\beta}{T_d}}{\frac{\Gamma_\epsilon}{T_d}} = \frac{Q_\beta}{Q}\left(\frac{\omega_o}{\beta_o}\right)^2$$

For representative values:

$$Q = 300$$

$$Q_\beta = 1000$$

$$\frac{\Gamma_\beta}{\Gamma_\epsilon} = 13.3$$

for a given disturbance torque amplitude.

Or

$$\Gamma_\beta = \frac{T_d}{40} \quad \text{E.U.}$$

If we wish to limit the output at the sum mode frequency to the equivalent of 25 EU due to sum-mode mismatch, then we can allow up to 1000 dyne-cm disturbance torques at the sum mode frequency.

b. Torque Variation With Eccentricity in a Fluid Journal Bearings

In any spin bearing now being considered for the rotating gravity gradiometer, a thin fluid film (liquid or gas) will exist between the bearing surfaces and this fluid film will produce a viscous drag torque on the rotor. Furthermore, this drag torque will, in general, vary with the load applied to the bearing. Clearly, spin axis torque variations can result in gradiometer measurement errors. It is the purpose of this analysis to define the viscous torque variation with bearing eccentricity ratio. For convenience a cylindrical journal bearing is assumed of sufficient length, L, that end effects may be neglected.

For any Newtonian fluid the shear stress on unit surface is proportional to the velocity gradient normal to the surface

$$\frac{dF}{dA} = \mu \frac{dU}{dz}$$

where the constant of proportionality is the viscosity, μ. The viscous torque, dT, on an element of surface, dA, of a journal of radius, R, is

$$dT = \mu R \left.\frac{dU}{dr}\right|_R dA$$

where $\left.\frac{dU}{dr}\right|_R$ is the velocity gradient at r = R. When the lubricant film thickness, h, is very much less than R, the velocity gradient is approximately

$$\frac{dU}{dr} \cong \frac{U}{h} = \frac{R\Omega}{h} \qquad (h \ll R)$$

where Ω is the journal spin velocity.

Then

$$dT = \frac{\mu R^3 L \Omega}{h} \, d\theta$$

When the journal is displaced from its concentric position,

$$h = h_o (1 + \epsilon \cos \theta)$$

where ϵ is the eccentricity ratio,

$$dT = \frac{\mu R^3 L \Omega}{h_o} \cdot \frac{d\theta}{1 + \epsilon \cos \theta}$$

and the total torque on the journal is

$$T = \frac{\mu R^3 L \Omega}{h_o} \int_o^{2\pi} \frac{d\theta}{1 + \epsilon \cos \theta}$$

$$T = \frac{2\pi \mu R^3 L \Omega}{h_o \sqrt{1 - \epsilon^2}}$$

and, if we write the torque at zero eccentricity as

$$T_o = \frac{2\pi \mu R^3 L \Omega}{h_o}$$

then

$$T = \frac{T_o}{\sqrt{1 - \epsilon^2}}$$

For small eccentricities

$$T = T_o\left(1 + \frac{1}{2}\epsilon^2\right) \qquad \text{approx. for } \epsilon \to 0$$

which shows that, for a periodic variation in eccentricity, $\epsilon = \epsilon_o \sin \omega t$, the change is torque

$$\Delta T = T - T_o = \frac{\epsilon_o^2}{4}\ (1 - \cos 2\omega t)$$

consists of a constant term plus a double-frequency term.

Returning to

$$T = \frac{T_o}{\sqrt{1-\epsilon^2}}$$

we have

$$\frac{dT}{d\epsilon} = \frac{T_o \epsilon}{(1-\epsilon^2)^{3/2}}$$

and, letting a = acceleration,

$$\frac{dT}{da} = \frac{dT}{d\epsilon}\,\frac{d\epsilon}{da} = \frac{T_o \epsilon}{(1-\epsilon^2)^{3/2}}\,\frac{d\epsilon}{da}$$

where $d\epsilon/da$ is in the form of a compliance. For the present discussion we may assume a constant compliance

$$\frac{d\epsilon}{da} = k = \text{constant}$$

$$\epsilon = ka$$

Then

$$\frac{dT}{da} = \frac{T_o k^2 a}{(1-k^2 a^2)^{3/2}}$$

and we see that the sensitivity of bearing torque to changes in acceleration is a function of the total acceleration. Current representative values of parameters in the above equation are:

$$T_o = 10^4 \text{ dyne-cm}$$

$$k = 0.2 \text{ per g}$$

$$a = 1 \text{ g}$$

which gives:

$$\frac{dT}{da} = 425 \text{ dyne-cm/g}$$

as the sensitivity to changes in acceleration when operating in a nominal 1 g field. Gradiometer measurement errors, resulting from spin axis torque variations, are discussed elsewhere in this report.

c. Phase Errors Due to Spin Bearing Disturbance Torques

The speed control servo of the rotating gravity gradiometer really serves two basic functions -- (1) It maintains the sensor spin velocity, ω_s, at precisely one-half the tuned resonant frequency, ω_o, of the sensor difference mode (velocity servo) and (2) it maintains a precisely constant mechanical phase angle, ϕ, between the rotor and the rotating measurement coordinate reference frame (position servo). These two functions are, of course, related by the fact that, by definition:

$$\omega_s \triangleq \frac{d\phi}{dt}$$

Spin bearing disturbance torques can produce speed control servo errors which result in gradiometer measurement errors by introducing errors in the orientation of the rotating sensor coordinate reference frame relative to the measurement coordinate reference frame. Because of the high "Q" of the difference mode resonance the error due to spin velocity error is by far the dominant one of the two above.

The slope of the sensor signal phase at resonance is given by:

$$\left.\frac{d\theta}{d\omega}\right|_{\omega_o} = -\frac{2Q}{\omega_o}$$

where

θ = signal phase angle

ω_o = difference mode frequency

Q = difference mode Q

or, in terms of spin frequency, ω_s:

$$\frac{d\theta}{d\omega_s} = -\frac{2\Omega}{\omega_s}$$

For this analysis the speed control servo transfer function is assumed to be given by

$$\phi(S) = \frac{S+3a}{(S+a)^3}\,\frac{T_d}{J}$$

where

ϕ = servo phase error

α = servo corner frequency

T_d = disturbance torque

J = rotor polar inertia

then, from above

$$\frac{d\theta}{dt} = \frac{d\theta}{d\omega_s}\,\frac{d\omega_s}{dt} = \frac{d\theta}{d\omega_s}\,\frac{d^2\phi}{dt^2} = -\frac{2\Omega}{\omega_s}\,\frac{d^2\phi}{dt^2}$$

and

$$\theta = \frac{2\Omega}{\omega_s}\,\frac{d\phi}{dt}$$

or

$$\theta(S) = -\frac{2Q}{\omega_s} S\phi(S)$$

$$\theta(S) = -\frac{2Q}{J\omega_s} \frac{S(S+3a)}{(S+a)^3} T_d$$

If we assume a step input disturbance torque, T_d

$$\theta(S) = -\frac{2QT_d}{J\omega_s} \frac{S+3a}{(S+a)^3}$$

and in the time domain

$$\theta(t) = -\frac{2QT_d}{J\omega_s} te^{-at}(1+at)$$

Because of the integration function inherent in the gradiometer filter process, we are interested not in the instantaneous value of θ but in the mean value, $\overline{\theta}$, over the integration interval, τ. For the worst case, where the step input occurs at $t = 0$ and remains through τ,

$$\overline{\theta} = \frac{1}{\tau}\int_o^\tau \theta(t)dt = -\frac{2QT_d}{J\omega_s\tau}\int_o^\tau t(1+at)\,e^{-at}dt$$

$$\overline{\theta} = -\frac{6QT_d}{J\omega_s\tau a^2}\left[1 - \left(1 + a\tau + \frac{a^2\tau^2}{3}\right)e^{-a\tau}\right]$$

For representative values,

$$a = 10 \text{ rad/sec}, \quad \tau = 10 \text{ sec}$$

this reduces to

$$\bar{\theta} = -\frac{6QT_d}{J\omega_s \tau a^2}$$

and with

$$Q = 300$$

$$J = 2 \times 10^5 \text{ gm-cm}^2$$

$$\omega_s = 110 \text{ rad/sec}$$

$$\bar{\theta} = 8.2 \times 10^{-8} T_d \text{ rad}$$

$$= 4.7 \times 10^{-6} T_d \text{ deg}$$

If we wish to restrict $\bar{\theta}$ to a maximum value of 0.0013 degrees, which corresponds to 0.1 E. U. maximum gradient error in the earth's field, then T_d must be limited to less than 280 dyne-cm.

d. Spin Bearing Specification

The spin bearing specification appears on the following pages.

PROCUREMENT SPECIFICATION

for

SPIN BEARINGS FOR HUGHES PROTOTYPE ROTATING GRAVITY GRADIOMETER

REVISION A

Date: 1 August 1972

No. AR-772

Approved by:

C. B. Ames

P. M. LaHue

A. Robinson

D. W. Rouse

Hughes Research Laboratories
3011 Malibu Canyon Road
Malibu, California 90265

TABLE OF CONTENTS

REVISION A		Page
1.0	Scope	4
2.0	Applicable Documents	4
3.0	Requirements	5
3.1	Conflicting Requirements	5
3.2	Materials, Parts and Processes	5
3.3	Gravity Gradiometer Description	5
3.3.1	Sensor Physical Parameters	6
3.4	Spin Bearing Performance Requirements	6
3.4.1	Second Harmonic Torque Ripple	7
3.4.1.1	Deterministic Torque Oscillation	
3.4.1.2	Random Torque Variations	
3.4.2	Torque Oscillations at Other Frequencies	8
3.4.3	Bearing Torque	8
3.4.4	Spin Bearing Load Capacity	8
3.4.5	Spin Bearing Compliance	9
3.4.6	Rotor Vibration	9
3.4.7	External Energy Requirements	9
3.4.8	Spin-Axis Alignment Reference	10
3.5	Environmental Conditions	10
3.5.1	Operating Performance Condition	10
3.5.2	Operating Standby Condition	10
3.5.3	Non-Operating Condition	10
3.6	Reliability Objectives	11
4.0	Quality Assurance Provisions	11
Figure 3.3	Rotating Gravity Gradiometer Baseline Configuration	12
Figure 3.5.3	Acceleration Spectra	13
Table 3.5	Environmental Conditions	14

REVISION A

The following listed paragraphs have been revised from the orginal specification AR-772 dated 5 July 1972.

3.2 Materials, Parts and Processes
3.4 Spin Bearing Performance Requirements
3.4.3 Bearing Torque
3.4.6 Rotor Vibration
3.4.7 External Energy Requirements
3.4.9 Electrical Insulation
3.5 Environmental Conditions
3.6 Reliability Objectives

Table 3.5 Environmental Conditions
3.5.1 Operating Performance Condition
3.5.3 Non-Operating

PROCUREMENT SPECIFICATION
FOR
SPIN BEARINGS
FOR
PROTOTYPE ROTATING GRAVITY GRADIOMETER

1.0 SCOPE

This specification covers the requirements for a spin-axis support bearing for a prototype moving-base rotating gravity gradiometer, which may be herein referred to as the "sensor." The sensor constitutes the basic sensing element in a system designed to precisely measure gradients of the gravitational field from a moving vehicle. The requirements and environmental conditions associated with the sensor necessitate that the spin bearing perform its function with great precision as well as being rugged, reliable and reproducible.

2.0 APPLICABLE DOCUMENTS

The following documents in their latest issue at contract date form a part of this specification to the extent specified herein.

Specifications –

3.0 REQUIREMENTS

3.1 Conflicting Requirements – Any conflicting requirements arising between this specification and any specifications or drawings listed herein shall be referred in writing, to the Hughes Research Laboratories (HRL) for interpretation and clarification.

3.1.1 Request for Deviation – Any deviation from the requirements specified herein shall be considered a deviation and shall not be allowed except by written authorization from HRL.

3.2 Materials, Parts and Processes – Materials, parts and processes used in the design, fabrication and assembly of the products covered by the specification shall be in accordance with sound and proven engineering and manufacturing practices. The manufacturer's selection shall assure the highest uniform quality and conditions of the product, suitable for the intended use. The bearing parts and their fasteners shall have a magnetic permeability not greater than 1.010 cgs units.

3.3 Gravity Gradiometer Description – A conceptual design sketch of the baseline configuration Rotating Gravity Gradiometer is attached as Fig. 3.3. The basic gravity gradient sensor consists of a crossed pair of mass quadrupoles coupled by a torsional spring and enclosed in a sealed, evacuated case. This case is then rotated at a spin frequency which is adjusted to precisely one half the inertia-spring resonant frequency of the coupled mass quadrupoles. The spinning system is enclosed within a nominally spherical shell which is, in turn, suspended within its mounting frame with two degrees of angular freedom for base motion isolation. The baseline sketch shows a hydrostatic gas spin bearing with pressurized gas supplied through hydrostatic gas gimbal bearings. The preferred configurations of both spin and gimbal bearings, however, are yet to be finalized.

3.3.1 Sensor Physical Parameters – Preliminary design estimates of various sensor physical parameters, which influence spin bearing selection and detailed design, are as follows:

Rotor Mass	7000 gms
Rotor Polar Inertia	2.5×10^5 gm-cm^2
Rotor Transverse Inertia	2.0×10^5 gm-cm^2
Rotor Shell Diameter	15.5 cm
Stator shell Diameter	18 cm
Stator Mass	5000 gms
Stator Polar Inertia	3.0×10^5 gm-cm^2
Stator Transverse Inertia	3.5×10^5 gm-cm^2
Rotor Spin Speed	1050 rpm
Motor Specifications	
Two-Phase Servo Drag-Cup	
Locked Rotor Torque	5×10^5 dyne-cm (max)
Running Torque	5×10^4 dyne-cm (max)

3.4 Spin Bearing Performance Requirements – Gravity gradient sensor performance requirements impose specific performance requirements on the sensor spin bearing.

The sensor spin bearing shall be capable of meeting the performance requirements set forth herein when supporting the rotor mass and moment of inertia load specified in paragraph 3.3.1 and rotating at the spin speed specified in paragraph 3.3.1 while the sensor is operating under the environmental conditions defined in paragraph 3.5.1 after the bearing is thermally stabilized. The required thermal stabilization time shall not exceed the following limits.

Beginning Soak Temperature	Stabilization Time
40°F	3 Hrs [1 Hr]
70°F	2 Hrs [1/2 Hr]
140 ±10°F	5 Min [1/2 Min]

The spin bearing shall be capable of meeting these performance requirements following exposure to the conditions set forth in paragraph 3.5.2 or 3.5.3.

In addition, the spin bearing shall meet these performance requirements throughout a 10,000 hour operating life with a minimum of 500 rotor start-stop cycles. Furthermore, the bearing shall meet the performance requirements at any time during a minimum one year period following assembly into the sensor.

In addition to the values assigned to the performance requirements, desire goals are indicated by values in brackets [ ] .

3.4.1 Second Harmonic Torque Ripple – Torque oscillations about the spin axis in a narrow frequency band centered at twice the spin frequency ($2\omega_s$) may cause significant errors in the sensor output. To the extent that these torque oscillations are deterministic, they can be compensated, however, the random portion of these torque oscillations cannot. The deterministic portion is made up of oscillation occurring at exactly $2\omega_s$ and whose phase is precisely fixed relative to the mechanical phase of the spin bearing. It is required that the magnitude of the deterministic torque oscillation not exceed the values specified in paragraph 3.4.1.1. Random torque variations are characterized by variations in both amplitude and phase relative to the above defined deterministic torque oscillation. As a consequence, the allowable random torque variations must be specified in terms of the magnitude of two mutually orthogonal components. It is required that the standard deviation of the magnitude of either of these orthogonal components within a narrow frequency band centered at $2\omega_s$ not exceed the value specified in paragraph 3.4.1.2.

3.4.1.1 Deterministic Torque Oscillation – The deterministic value of the torque oscillation shall be defined as the average

value over a ten (10) hour operation following thermal stabilization. This value shall not exceed 1000 dyne-cm. In addition the mean value of the deterministic torque oscillation when averaged over the first hour of operation following thermal stabilization shall not differ from the ten (10)-hour mean value by more than 50 dyne-cm.

3.4.1.2 Random Torque Variation – The standard deviation of either orthogonal component of the random torque variation within a 0.1 Hz wide frequency band centered at $2\omega_s$ shall not exceed 50 dyne-cm over a ten (10) hour operation following thermal stabilization.

3.4.2 Torque Oscillations at Other Frequencies – The root-mean-square value of spin-axis torque oscillations within any 0.1 Hz wide frequency band outside the band specified in paragraph 3.4.1.2 shall not exceed 500 dyne-cm [50 dyne-cm].

3.4.3 Bearing Torque

a. Mean running torque shall not exceed 5×10^4 dyne-cm [2×10^4] when the mean applied load is 15 lbs.

b. Running torque sensitivity to variation in applied load shall not exceed 300 dyne-cm/pound [10] when the mean applied load is 15 lbs.

c. Bearing torque shall not exceed 1×10^5 dyne-cm while starting or during acceleration to the specified spin speed with a mean load of 15 lbs.

3.4.4 Spin Bearing Load Capacity

a. Axial and radial load capacities shall not be less than 50 pounds [200].

b. Torsional load capacity shall not be less than 50 in-pounds [100].

3.4.5 Spin Bearing Compliance

a. Axial and radial compliances shall not exceed 5×10^{-11} cm/dyne [10^{-11}].

b. Axial and radial compliances shall not differ by more than 20 percent [10].

c. Torsional compliance shall not exceed 10^{-12} rad/dyne-cm.

3.4.6 Rotor Vibration

a. The integrated power spectrum of bearing-induced rotor translational acceleration shall not exceed 0.01 cm/sec^2 rms [0.001] in the frequency range $1/2\,\omega_s$ to $4\,\omega_s$. Outside this frequency range, the power spectral density shall not exceed 1.0 cm^2/sec^4/Hz [0.01].

b. The integrated power spectrum of bearing-induced rotor angular rate, normal to the spin axis, shall not exceed 5×10^{-11} sec^{-2} [10^{-11}].

3.4.7 External Energy Requirements — If an external energy supply is required to provide bearing support, the following limits shall apply:

a. For a hydrostatic gas bearing;

(1) Inlet pressure shall not exceed 100 psig.

(2) Total volume flow rate shall not exceed 1.0 standard cubic feet per minute.

b. For an electrically actuated bearing;

(1) Voltage shall not exceed 100 volts.

(2) Current shall not exceed 1.0 amp.

(3) Power shall not exceed 0.5 watt per pound of load.

3.4.8 Spin-Axis Alignment Reference – A spin-axis alignment reference shall be provided which permits location of the spin reference axis to an accuracy of one mrad.

3.4.9 Electrical Insulation – Though not an absolute requirement, it is highly desirable that –[It shall be possible to electrically insulate each of the bearing components from its mechanical mounts. The insulation resistance shall not be less than 5 megohms at 500 volts and 60 Hz].

3.5 Environmental Conditions – During the specified life requirements of paragraph 3.4, and while the spin bearing is supporting the mass and moment of inertia rotor load specified in paragraph 3.3.1, the spin bearing may be subjected to the following environmental conditions. These conditions are summarized in Table 3.5.

3.5.1 Operating Performance Condition – This condition represents the most extreme environments under which the bearing is required to operate and meet the specified performance of paragraph 3.4. When subjected to the environments of this condition, the bearing will be energized (if applicable) and rotating at the specified spin speed.

3.5.2 Operating Standby Condition – This condition represents the most extreme environments under which the bearing is required to operate and survive without damage. When subjected to the environments of this condition, the bearing will be energized (if applicable) and may be either not rotating or rotating at speeds up to 5,000 rpm.

3.5.3 Non-Operating Condition – This condition represents the most extreme environments to which the bearing may be subjected while in a non-operating state. It must survive these environments without damage. The non-operating state is defined as not rotating and not energized (if applicable). A rotation locking device may be employed if necessary.

3.6 Reliability Objectives – The sensor spin bearing shall have a reliability objective of 0.995 when operated under the environmental conditions set forth in paragraph 3.5.1 at any time during 10,000 hours of operation.

4.0 QUALITY ASSURANCE PROVISIONS

Assurance that the sensor spin bearing meets the performance requirements set forth in paragraph 3.4 will be provided by means of (a) the Vendors Quality Control Program; (b) an adequate Testing Program; and (c) a Reliability Verification Program.

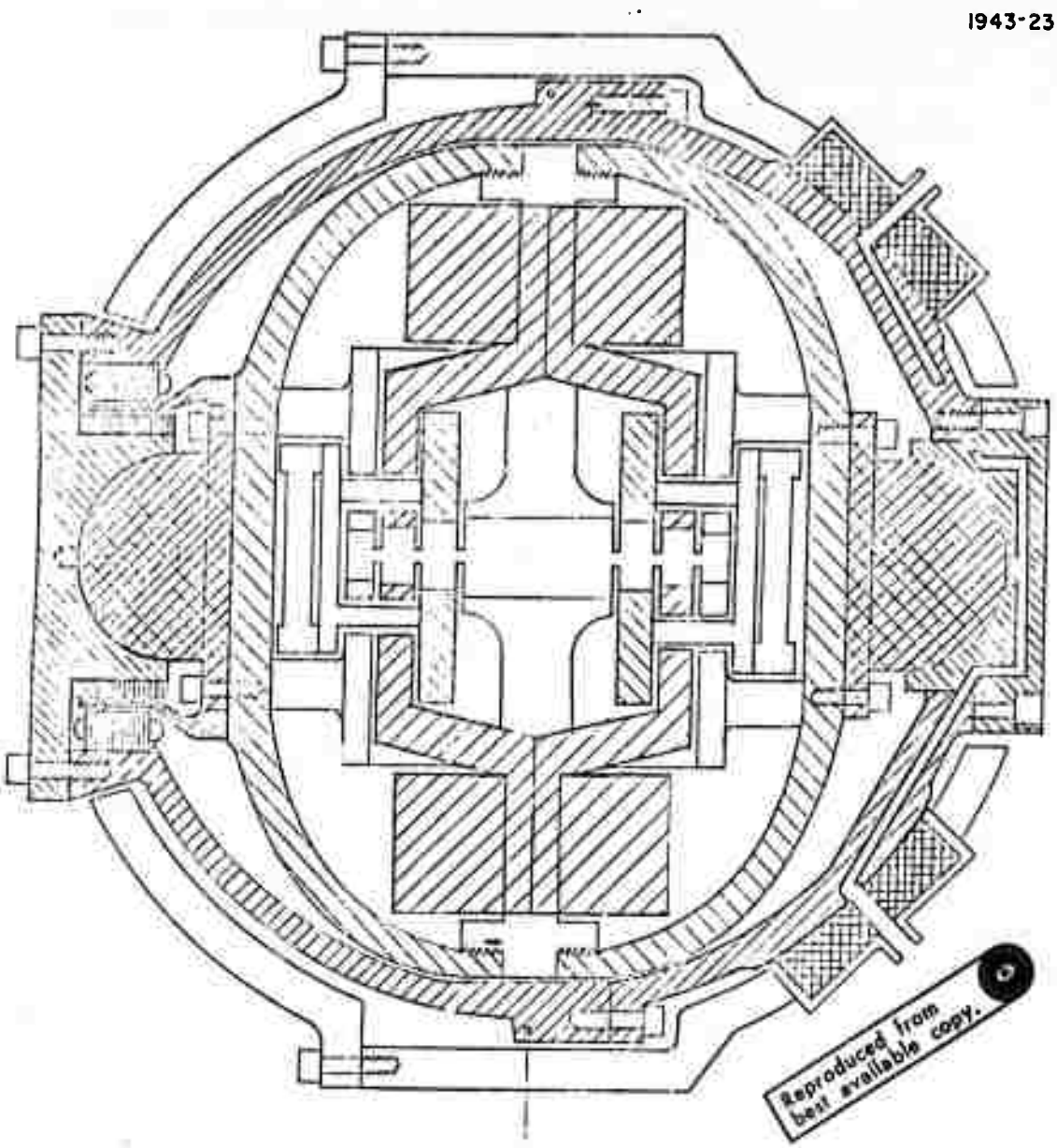

Fig. 3.3. Conceptual Design Sketch For Rotating Gravity Gradiometer.

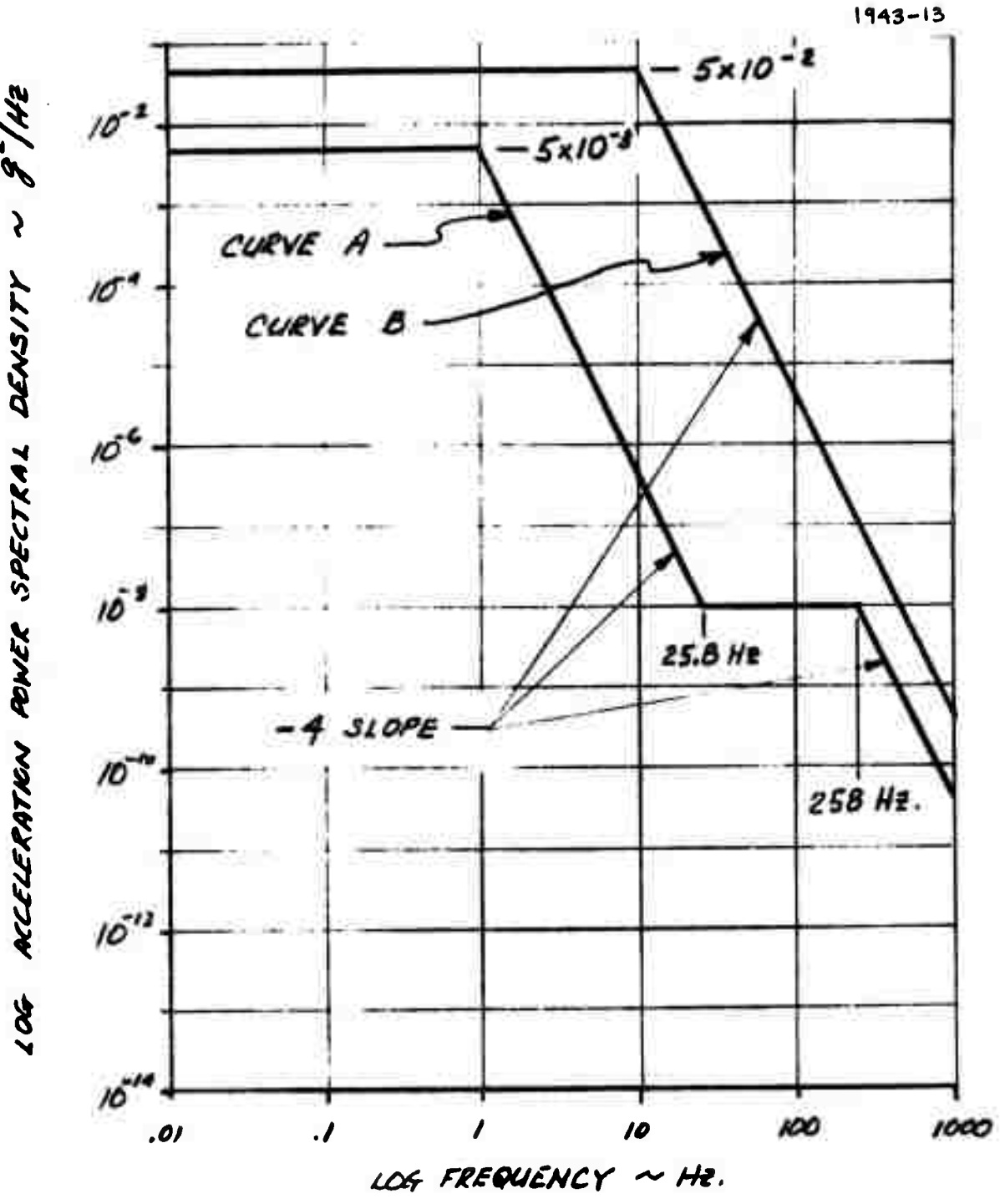

Fig. 3.5.3. Acceleration Spectra.

Table 3.5. Environmental Conditions

Environment	Operating		Non-Operating
	3.5.1 Operating Performance Condition: (Rotating at specified spin speed and energized, if applicable)	3.5.2 Operating Standby Condition: (Rotating 0 to 5,000 rpm, and energized, if applicable)	(Not rotating, not energized if applicable)
1. Temperature	Ambient air and structure temperature surrounding the bearing shall be controlled to a set point of 140° ±10°F within ±0.5°F. If a gas bearing is used, the supply gas temperature will be maintained at ____°F ± ____°F. Vendor to specify set point and limit.	Ambient air and structure temperature surrounding the bearing between 40°F to 130°F. If a gas bearing is used, the supply gas temperature may vary from 40°F to 130°F.	Ambient temperature between -30°F to +200°F.
2. Humidity	Ambient air 10% to 80% R.H. at temperatures specified above. If a gas bearing is used, the relative humidity of the supply gas may be controlled, if necessary. Vendor to specify.	Ambient air 10% to 95% R.H. at temperatures specified above. If a gas bearing is used, the supply gas humidity may vary from 10 to 95% at supply pressure whose temperature is between 40°F to 130°F.	Ambient air 10% to 95% at temperatures specified above.
3. Pressure Altitude	0 - 10,000 ft.	40,000 ft max.	40,000 ft max.
4. Mechanical Shock	Negligible	Not to exceed 100 terminal sawtooth shocks at 50 g for 11 ms in any direction at temperatures and pressures specified above.	Not to exceed 100 terminal sawtooth shocks at 50 g for 11 ms in any direction at temperatures and pressures specified above.
5. Acceleration (D.C.)	Static acceleration not to exceed ±1.1 g in the vertical direction and ±0.1 g in the horizontal direction. Bearing spin-axis may be anywhere between a vertical to a horizontal orientation during simultaneous application of above specified acceleration levels.	Static total vector acceleration not to exceed 3 g's in any direction with respect to the bearing spin axis.	Static total vector acceleration not to exceed 20 g's in any direction with respect to the bearing spin-axis.
6. Vibration	Acceleration power spectral density not to exceed the levels shown in curve A of Fig. 3.5.3.	Acceleration power spectral density not to exceed the levels shown in curve B of Fig. 3.5.3.	Acceleration power spectral density not to exceed ten times the levels shown in curve B of Fig. 3.5.3.

T726

8. RGG Baseline Parameters

The following parameters define the characteristics of the Moving Base Rotating Gravity Gradiometer as of 31 July 1972. All of these are subject to minor adjustments in the final design and a few may have to be changed significantly as the analysis progresses.

a. System Parameters

(1)	Spin frequency, f_s	17.5 Hz
	ω_s	110 rad/sec
(2)	Sensor difference mode resonant frequency, f_o	35 Hz
	ω_o	220 rad/sec
(3)	Sensor sum mode resonant frequency β_o	142 rad/sec
(4)	System integration time, τ_i	10 sec
	a. Sensor integration time, τ_s	2.73 sec
	b. Filter integration time, τ_f	7.27 sec
(5)	Sensor Q	300
(6)	Inertia efficiency of each arm, η	0.861
(7)	Polar inertia of each arm, C or I_1	35,610 gm-cm^2
(8)	Peak signal energy stored in sensor, ϵ_p	1.23×10^{-21} joules/EU
(9)	Peak arm torque, T_p	1.53×10^{-5} dcm/EU

b. Rotor Parameters

(1) Materials

- Sensor arms — 6061 Al
- Sensor masses — Mallory 1000
- Sensor pivots — Be-Cu
- Rotor frame — 6061 Al
- Rotor end bells — 6061 Al
- Spin bearing — not specified
- Balance screws — 6061 Al and Be-Cu

(2) Rotor Data:

	Mass gms	I_{xx}	I_{yy}	I_{zz}
		gm cm^2		
Arm No. 1	1,563	4,990	35,600	35,610
Arm No. 2	1,563	35,600	4,990	35,610
Rotor (except arms)	2,750	103,400	103,400	132,700
Total Rotor	5,876	143,990	143,990	203,920
Stator	3,766	289,200	289,200	252,600
Rotor and Stator	9,642	433,190	433,190	452,500

c. Design Limits

(1) Temperature

- Operating control point — $130^{\circ}F$
- Operating control range — $\pm 0.005^{\circ}F$

(2) Arm mass unbalance, Δmh — $\pm 4 \times 10^{-4}$ gm cm

- Balance tube adjustment range available — $\pm 28 \times 10^{-4}$ gm cm

(3)	Arm inertia unbalance ratio, k_β	10^{-6}
(4)	Maximum signal provision	±10,000 EU
(5)	Signal level (not firm)	20 to 200 nv/EU
(6)	Peak signal energy stored in transducer - percent of total	10 to 20%

D. MATERIALS SELECTION

1. Material Characteristics

2. Paramagnetic and Diamagnetic Material Tests

These sections provide the background upon which the materials are selected for construction of the RGG.

1. Material Characteristics (Preliminary)

a. General

Materials used in the construction of rotating gravity gradiometers (RGG) should have the following characteristics:

Dimensional stability

Linear and stable thermal coefficients

Isotropic

High anelastic limit (high strength)

High density and low density selection

High mechanical Q (low damping)

Low magnetic susceptibility (nonferromagnetic)

Workability

High and low thermal and electrical conductivity selection.

A review of Table IV Ref. (4), (5) and (6) demonstrates that no materials have all of the desired characteristics when examined minutely and, furthermore, data or analysis on some of the characteristics are not readily available. Many of the parameters of many of the materials have not been studied in depth. Parameters of high purity materials can not be extrapolated to commercial pure grades and various alloys. Table IV Ref. (5) in particular demonstrates that almost all metals creep with age, stress and temperature cycles. That they are all anisotropic; the temperature coefficients vary with stress, alloy and operating temperature; and the elastic limit is largely dependent on the accuracy of the measuring equipment.

In view of this situation the best RGG design will result if all materials are viewed (on the microscopic scale) as ferromagnetic "silly putty" until they are proven otherwise in a commercially available or high purity grade. The situation is not actually as bad as it

might at first appear since instrument designers have long been concerned with basic material parameters. Some materials and processes have been tested extensively and most of these are included in Table IV, Ref. 4.

Table IV provides a summary of many of the characteristics of several materials. Since some of the data was obtained from several sources the data are not always completely consistent. However, the data are believed to be representative and usable for RGG design. The tabulations "Dimensional Stability Tests" and "Anelastic Limit σ_A" require comment.

Dimensional stability test data was taken from Table IV Ref. (4). The notation: RT_{store}-1 mo-3 mo-12 mo and $160^{\circ}F_{store}$-1 mo-3 mo-12 mo refer to the changes in the strain in a 4 inch long sample when stored at room temperature and at $160^{\circ}F$. The measured strains are reported to the nearest 5 μm/m. Unfortunately, it is not completely clear whether the 12 mo figure represents the change from the initial value or the change from the 3 mo value. However, a study of the data on many materials indicates that the quoted value is the change from the initial value. Note that a dash in the data indicates an absence of data and not a zero change.

The temperature cycling tests associated with the Dimensional Stability heading represent 10 cycles between $70^{\circ}F$ and $-95^{\circ}F$ with a 30 minute holding period at $-95^{\circ}F$. The changes marked with * are for 10 times from +200 to $-100^{\circ}F$.

The term "anelastic limit" is taken from Table IV Ref. (13) and the meaning is illustrated in Fig. 15. A sequence of stress strain curves are run to increasingly higher stresses. The first curve that shows an open loop, but no residual strain is called the elastic limit. The first loop that shows a residual plastic strain of 10^{-6} m/m is called the anelastic limit. The anelastic elastic limit is synonymous with "Precision Elastic Limit (PEL)," "Microyield Strength (MYS)" and "Micro Offset Yield Stress (MOYS)" if the same residual plastic deformation base is used in all cases. Considerable care is required in the interpretation of data since various authors are not consistent.

TABLE IV

Properties of Materials (Sheet 1 of 3)

Material and Specification	Composition per Specification %	Recommended Mechanical and Thermal Treatment for Maximum Dimensional Stability	Dimensional Stability Tests with Recommended Treatment $\mu m/m$ Change RT store -1mo- 1mo- 12mo 140°F store -1mo- 1mo- 12mo Temp Cycle 10X, -65°F	Magnetic Susceptibility/ Unit Mass (emu) $\chi \times 10^6$ Permeability (emu) = Relative Perm (siu) = $\mu = 1+4\pi\chi\rho$	Density $D = kg/m^3$ (ρ = gm/cm^3)	Thermal Coefficient of Expansion $\mu m/m/°C$ Average 0-50°C	Electrical Restivity μ ohm-cm Thermal Coef. Elect. Resistive at 20°C	Thermal Conductivity Cal / Cm x °C x Sec
6061 Alum QQ-A-250/11d (Plate) T-651	Mg 1.0 Si 0.6 Nominal Cu 0.25 (a) Cr 0.25	Start with T-451 temperature Machine light cuts (a) After finish cut, overage (2) 24 hrs at 400°F. Temp Cycle	(a)(4) RT -15 -15 — 160 +5 +5 — TC -20	(+0.63) (11) 1.000021 (11) ±0.000005	2,700 (2.70)	23.4	(4.0) Above is an average	0.37 at 20°C
Beryllium MIL-B-21551 Vacuum Hot Pressed Block	Be 97.4 Min BeO 3.0 Max + Impurities	4 hrs - 400°F after finish machining Temp Cycle	(4) RT 0 0 — 160 — -4 — TC -20	(-1.0) 0.999977	1,850 (1.85)	11.6 (a)	(4-6) 0.025	0.35
Beryllium-Copper QQ-C-530b Copper Alloy No. 17A	Cu 97.9 Be 1.9 Nominal NiorCr 0.2 (a)	Start with 1/4 hard material Machine light cuts. After finish cuts, overage. (6) 4 hrs - 650°F. Temp Cycle	RT 0 0 — 160 — -5 — TC -5 (a)(4)	(-0.62) 0.999936	8,200 (8.2)	16.6	(5.7 - 7.8) Above is an average	0.25
Elgiloy	Co 40 Be 0.04 Cr 20 C 0.15 Ni 15 Fe Balance Mo 7 Mg 2 (12)	After finish machine 5 hrs - 980°F (9)		(+0.39) (9) 1.00004	8,300 (8.3)	12.7	(360) Above is an average	0.03
310 Stainless ASTM A276 & A314	Cr 25 Ni 20 C 0.25 Max Fe Bal	Start with material - Quench Annealed: Water quench after 1/2 hr, 1950°F. After finish machine stress relieve 20 hrs - 750°F + 20 - 200°F and air cool	RT — — 5 160 — — 10 TC 20	(+20) ~1.002	7,880 (7.88)	16.8	(73) Above is an average	0.033
Mallory 1000	Cu 4 Ni 6 W 90	Stress relief 2 hrs - 600°F in air	No data available	(+0.33) ~1.00007 (a)	16,960 (16.96)	5.4 (b)	(12.45) Above is an average	0.225

a. See text for details
b. Over temperature range 20 - 400°C
4, 5, 6, etc. references page 3
( ) Indicates conventional units

TABLE IV

Properties of Materials (Sheet 2 of 3)

Material	Specific Heat J/kg/°C (cal/gm/°C)	Machine-ability	Hardness R = Rockwell Bhn = Brinell M = Mho V = Vickers	Modulus of Elasticity			Poissons Ratio υ $Y_G = \frac{Y_T}{2(1+Y)}$	Thermal Coefficient Modulus of Elast.		UTS Ultimate Tensil Strength 10^{-3} psi / % Elongation	Yield Point 0.2% Offset 10^{-3} psi
				Tension	Compression	Shear		T&C $(\Delta Y/Y)/°C \times 10^6$	Shear $(\Delta Y_G/Y_G)/°C \times 10^6$		
				$Y_T = N/m^2 \times 10^{-10}$ ($E_T = lb/in^2 \times 10^{-6}$)	$Y_C = N/m^2 \times 10^{-10}$ ($E_C = lb/in^2 \times 10^{-6}$)	$Y_G = N/m^2 \times 10^{-10}$ ($G = lb/in^2 \times 10^{-6}$)					
Aluminum 6061	(0.23)	Fair	Bhn = 95	6.8	7.0	2.7	0.33	-580	-580 est	(33)	(38)
				(9.9)	(10.1)	(3.8)				10	
Beryllium Be	(0.45)	Fair (a) Caution	R-B75-85	29.0	29.0	14.2	0.024 to 0.030	-140		(40)	(30)
				(40-44)	(40-44)	(20.3)				1	
Be-Cu Beryllium Copper	(0.1)	Fair	R-C37	11.7	11.7	4.5	~0.33	-350	-330	(175)	(165)
				(17)(6)	(17)(6)	(6.5)(6)				8	
Elgiloy		Fair	V-702	19.6	~19.6	7.7	Anisotropic due to cold work	-396	-130	(368)	(260)(c)
				(28.5)	(~28.5)	(11.2)				1	
310 Stainless	(0.12)	Fair	R-B85	20.6	~20.6	~8.2	0.32	-450	-450	(95)	(45)
				(30.0)	(~30.0)	(~12)					
Mallory 1000	(0.032)	Fair	R-C24-30	27.6		13.2	0.04			(94-112)	(75)
				(40)		(19.2)				6.0	

(c) 0.02% offset

TABLE IV

Properties of Materials (Sheet 3 of 3)

TABLE IV

Properties of Materials (Sheet 3 of 3)

Material	Fatigue Limit PSI x 10^{-3} Based on 5×10^8 Cycles, R. R. Moore Rotating Beam Test	Max Recom. Operating Temp For Max Stability	Mechanical Q / Damping	Corrosion Resistance	
Aluminum 6061	(2) (14)	(a) 73°C (165°F)	~5000 (10)	(2) Fair	
Beryllium		(a) 73 (165°F)	(a)		Commercial grade tabulated here. Higher Purity grades available but mostly a reduction in BeO. Mechanical properties highly dependent on flake orgrain size and processing.
Be-Cu	(~32)			Good Similar to Pure Copper	
Elgiloy	(~60)			(9) Excellent	(a) Available in small diameter rods and thin strips only.
310 Stainless				Excellent	
Mallory 1000	(~40)	(~300°F)	Reliability High	Excellent	Available up to 2-1/2" dia x 12" long 2-1/2 x 2-1/2 x 12

1. Aluminum Standards And Data 1970-71, The Aluminum Association, 750 3rd Ave, NY, NY Commercial: Specs, Composition, Forms, Tempers
2. Aluminum, Kent R. VanHorn Editor, 1967 American Metals Society, Metals Park, Ohio. 3 Vol. I-Properties, II-Design, III-Fabrication
3. The Beryllium Metal Handbook, 1967, General Astrometals Corp.
4. A Review of Dimensional Instability in Metals, DMIC Memorandum #189, 19 March 1964, Defense Materials Information Center, Battelle Memorial Institute, Columbus, Ohio.
5. Dimensional Instability - An Introduction, DMIC Memorandum #253, April 1971, Defense Materials Information Center, Battelle Memorial Institute, Columbus, Ohio, 43201
6. Metals Handbook, Vol. 1, Properties and Selection, 8th Ed. 1961, American Society for Metals, Metals Park, Ohio
7. Mechanical and Physical Properties of Austenitic Chromium-Nickel Stainless Steels, International Nickel Co, Inc. 1963, 1 New York Plaza, NY, NY, 10006
8. The Metal Beryllium, D. W. White Jr and J. E. Burke, Eds. American Society for Metals, 1955
9. Elgiloy Catalog and Specifications, Elgiloy Company, 853 Dundee Ave, Elgin Ill. 60120
10. Electromechanical Transducers and Wave Filters, W. P. Mason, 2nd Ed. 1948, D. VanNostrand Co, NY, NY
11. Magnetic Permeability of Commercial Aluminum Alloys, Personal Communication, W. C. Sleppy, Alcoa Research Laboratories, Merwin, Penn., 11 Jan 1972
12. How Temperature Affects Instrument Accuracy R. Gittis, Control Engineering, FP 70-78, April, 1955
13. Observations of Microplasticity, N. Brown, Advances In Materials Research, Vol. 2, John Wiley and Sons, (1968), NY, NY
14. High Density Metals, P. R. Mallory Co., Indianapolis, Ind. 1962
15. Tungsten, Smithells, Colin J., Chapmant Hall, 1952, 3rd Ed.
16. Copper-Metal, Alloys and Compounds; Butts, A, Ed; Amer. Chem. Soc. Monograph Series; Reinhold Publish Corp. NY, 1954

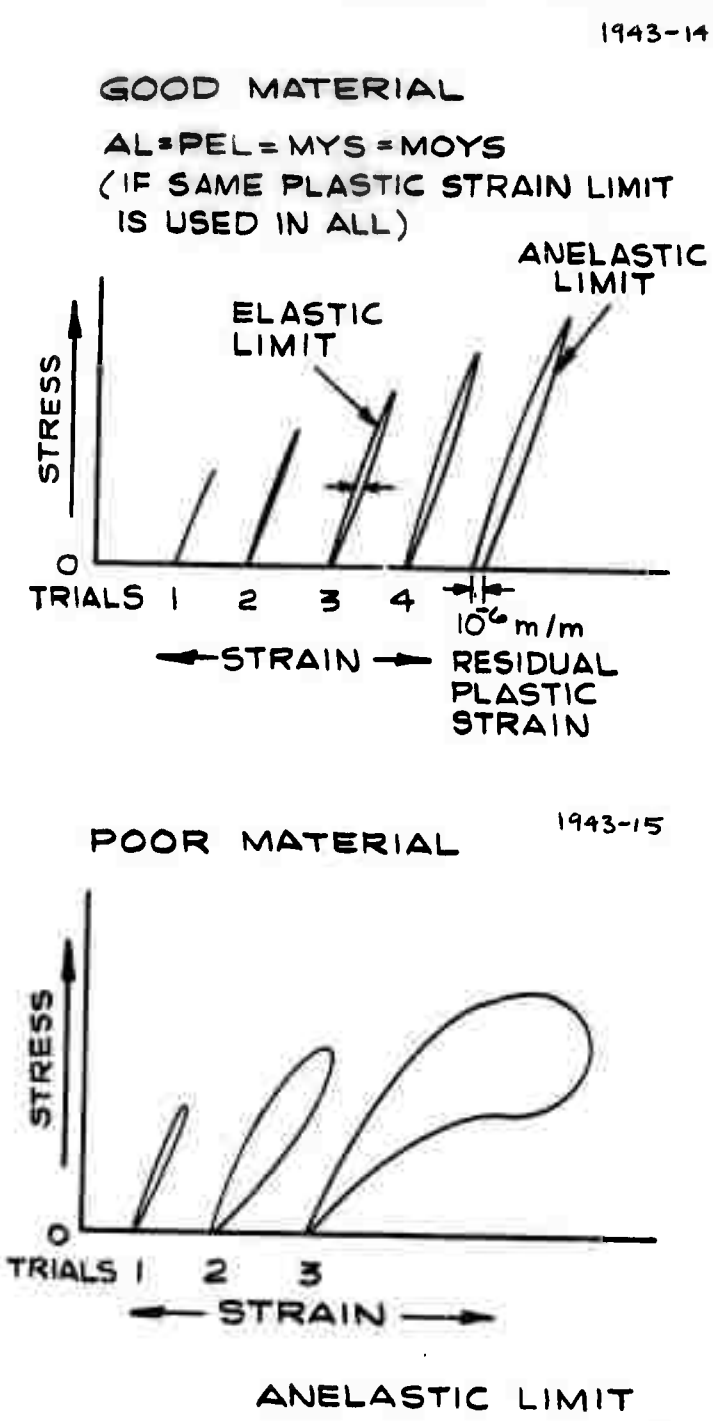

Fig. 15. Anelastic-Elastic Limit.

b. Comments and Notes on Various Materials and Processes

The following remarks and notes on various materials and processes have been obtained from a wide variety of sources and experiences. They should be considered in the selection of instrument materials.

Aluminum: Aluminum is a generally acceptable instrument material. Its greatest drawback is that it is usually rated only fair for dimensional stability.

Beryllium: Beryllium is a generally acceptable instrument material. Its drawbacks are a health hazard during machining and low mechanical Q.

Stainless Steel: Stainless steel is not acceptable if magnetic field sensitivity is a problem. 310 is the best (μ = 1.0018) and the permeability is not significantly increased by cold working.

Brass: Brass has been used in various types of instruments for years and is generally considered to be "nonmagnetic". Most brasses if made from pure element materials do have a permeability of 1.00001 or less. However, nearly 50% of all brass products are made from reclaimed scrap and thus the impurities are poorly controlled. Brass has little to recommend it as an instrument material except its easy availability. Its creep strength is poor, its stability is poor and government specifications do not provide good impurity control. Table IV Refs. (16) and (6) provide good insight to the magnetic properties. Beryllium copper should generally be used.

Uranium: Uranium is notorious for its anisotropic moduli and temperature coefficients. Investigate carefully if it is considered.

Tungsten Alloys: Tungsten has a great affinity for iron and its alloys are frequently slightly ferromagnetic. Tungsten alloys should have the highest possible purity and should be batch tested.

Ni-Span C: Ni-Span C is a material that has been especially developed to have a constant modulus of elasticity over a relatively wide temperature range. It has a significant magnetic permeability and is usable only in special cases in precision instruments.

Impurities in Alloys: Commercial and government alloy specifications are checked for the desired alloy element limits only. Impurities are not checked unless contamination is suspected. Thus commercial or government specification alloys may contain unknown impurities. In critical applications the most economical approach may be to purchase to the government specification and then have the batch checked for the impurity level.

Impurities on Alloys: Machine tool wear leaves significant traces of ferromagnetic impurities on the surface of otherwise paramagnetic or diamagnetic materials. In critical applications all finished parts should be given a preferential etch to remove this contamination.

Residual Stresses in Stock Material: Many metals are hardened and strengthened by severe cold working and/or by a solution heat treat and quench. If a large billet is cold reduced 75% by rolling into a bar, the residual stress near the surface may be twice that near the center. If the top half of the bar stock is milled away the finished piece will curl significantly immediately and continue to curl with time. The same type of creep can be produced by unequal stresses introduced by quenching during a solution heat treatment. The most stable parts are produced by symmetrical machining of the stock and by minor cold working (usually stretching) to equalize the thermal induced stresses.

Stability with Age and Temperature Cycles: Many metals are hardened and strengthened by precipitation of alloy elements into the base material crystalline structure. Precipitation hardening may be used alone after a solution heat treat (beryllium copper) or in addition to cold work and solution heat treat (2024 aluminum). The precipitation may occur at room temperature and unless artifically aged it can continue for years at room temperature. Precipitation for maximum hardness, ductility and strength usually occurs at a specific temperature and the material can be held at this optimum temperature for extended periods of time with little further change in characteristics. However, if the material is hardened at a temperature higher than optimum, the strength, hardness and ductility will at first increase as a function of treatment time, peak out and then decrease as a function

of time. This is called overaging. Experience has shown that overaged precipitation hardened materials are more stable with time and temperature cycling than those given an optimum strength heat treat.

c. Details on Selected Materials

The following paragraphs provide detailed information for the materials listed in Table IV.

(1) Aluminum:

Aluminum can be obtained in the following mill forms:

- Unalloyed ingot
- Casting alloy ingot
- Alloyed ingot
- Wrought alloys
  - Heat-treatable
  - Non-heat-treatable

Unalloyed aluminum is very difficult to machine and has low strength. It is not appropriate for precision instrument fabrication except possibly as an electrical conductor.

Casting alloys do not offer any superior characteristics for instrument manufacture and will not be considered further.

Alloy ingot is the base for the wrought alloy products. Except in unusual circumstances it would be more cost effective to purchase the wrought alloy form (sheet, rod, bars, etc.) directly.

The numerous wrought alloys of aluminum have been developed to obtain specific characteristics such as high strength, corrosion resistance, weldability and workability. Since most instruments do not require especially high strength or other unusual characteristics the parameters of chief concern are:

- Dimensional stability
- Elastic moduli stability

- Thermal expansion stability
- Low magnetic susceptibility
- High anelastic limit
- Workability.

The non-heat-treatable alloys attain their strength and workability by severe cold working. The resulting internal stresses can not be relieved by heat treatment and because of this they are not particularly dimensionally stable. These non-heat-treatable alloys are considered to be generally unsuitable for instrument manufacture.

The heat-treatable wrought alloys usually attain their best strength, workability and other characteristics by a combination of cold working and heat-treatment. Alloy AA-6061 requires little cold work and responds well to heat treatment. It has been selected as one of the best for precision instrument work.

The chemical composition limits for AA-6061 from Table IV Ref. (1) and Federal Specification QQ-A-250/11E (27 Aug 71) are:

Silicon	0.40-0.80
Iron	0.7
Copper	0.15-0.40
Manganese	0.15
Magnesium	0.80-120
Chromium	0.15-0.35
Zinc	0.25
Titanium	0.15
Other elements:	
Each	0.05
Total	0.15

Aluminum Remainder

Notes: Composition is in percent maximum unless a range is shown. Analysis is regularly made only for the elements for which specific limits are shown.

The best temper and stabilizing heat-treatment for 6061 has not yet been definitely established. However, the following should be near optimum. The material should be purchased in the T-451 temper. In this temper it has been solution heat treated at 985±10°F for 4 hours, quenched, stretched 1 to 3% and naturally aged (stored at room temperature). After finish machining it should be overaged by precipitation hardening at 400±10°F for 24 hours. The overaging will reduce the ultimate tensil strength and yield strength slightly below the maximum possible values but it will also improve the creep stability. The X51 in the temper designation designates the stretching to help equalize the cold work and quenching strains. Finally the part shall be temperature cycles 10 times from +200°F to -95°F with a holding period of not less than 10 minutes at each temperature.

The magnetic susceptibility of the aluminum alloys is nearly the same as that of pure aluminum. As shown on page 176, Vol I, of Table IV Ref. (2), some of the alloy materials reduce the susceptibility slightly while others increase it slightly. Iron, if not in excess of a few percent, combines with the aluminum to produce $FeAl_3$ which is paramagnetic to about the same extent as pure aluminum. Mr. W. C. Slepy of Alcoa Research Laboratories states in a private communication, "A typical U. S. Government magnetic property specification reads: "The magnetic permeability of the material is not to exceed 1.001 cgs units in a 30 orsted field." All of Alcoa's commercial alloys meet this specification quite easily; 6061, for example, has a magnetic permeability of 1.00002 cgs units. None of Alcoa's commercial alloys are ferromagnetic. They are weak paramagnetic materials whose permeabilities are in the range 1.00002 ± 0.000005 cgs units. Thus the only problem might be the accidental contamination of a batch or billet not tested. For extremely critical and high cost experiments

the most reasonable procedure would be to purchase Government specification material (which could be as high as 1.001) and have samples tested for iron and susceptibility.

The maximum operating temperature is based entirely on known stability at this temperature from their use in precision gyroscopes and accelerometers.

No actual data is available on the anelastic limit but it is in the neighborhood of 1,000 psi.

(2) Beryllium:

The characteristics of beryllium vary widely with the method of manufacture and purity. Table IV Refs. (3) and (8) provide many details. The most common impurity is beryllium oxide and its effect is not especially large. The material selected here is a medium grade material, readily available from several sources. Higher strength and higher purity are readily available. Nuclear purity grades are not necessary.

Beryllium dust is highly toxic and the effect is cumulative. Proper facilities for machining are imperative. Hand "dressing", fitting or scraping must not be done. However, the finished parts are perfectly safe to handle and assemble.

Actual numbers are not available but beryllium is known to have high internal damping. It is not useful as a spring material in a high "Q" system.

The recommended heat treatment and operating temperatures are based on the known characteristics from their use in precision gyroscopes and accelerometers.

The thermal coefficient of expansion quoted is for this particular grade and process. It varies rather widely with other purities and processes.

(3) Beryllium-Copper

Beryllium-copper is a strong stable material that is slightly diamagnetic and is easily worked. The percent composition from Table IV Ref. (6) and QQ-C-5306 is:

Beryllium	1.8 - 2.0
Cobalt	0.20 min.
Nickel plus cobalt plus iron	0.60 max.
Copper plus beryllium plus elements named	99.50 min.

Note: Analysis shall be made regularly only for the elements specifically mentioned.

Beryllium-copper is a precipitation hardened alloy. Alloy No. 172, as reived in the quarter hard condition, has been solution heat treated, sometimes called solution annealed, at 1450 ± 5°F for several hours, quenched and then cold worked to produce the desired quarter hard temper. After finish machining it must be further precipitation hardened to attain the desire ultimate properties. The standard heat treatment to attain the ultimate strength is from MIL-H-7199A, 2 hours at 600 ± 5°F. However, for maximum dimensional stability, overaging is desired and the specified treatment is 4 hours at 650 ± 5°F. This overaging will cause some reduction in ultimate tensile strength and some reduction in hardness but these are not serious drawbacks.

The magnetic susceptibility of the quarter hard precipitation hardened alloy is quoted in Table IV Ref. (6) as -0.62×10^{-6} cgs (emu) units. The magnetic effects of impurities on copper base alloys is discussed in considerable detail in Table IV Ref. (16). This reference indicates that as long as the iron content is less than 0.15 percent the susceptibility will be no greater than 1.5×10^{-6} cgs units. Thus, for critical applications each batch should be purchased to the government specifications and then tested for magnetic properties.

(4) Elgiloy:

Elgiloy was developed to provide a very strong, stable, nonmagnetic material for precision spring applications. It is manufactured and distributed by the Elgiloy Company, 853 Dundee Avenue, Egin, Ill. 60120. The composition and characteristics shown in Table IV were obtained from Specification No. 54-71A of the Elgiloy Company.

Elgiloy has one characteristic that limits its use in RGG applications. The stock sizes of the rod (wire) are limited to about 0.130 inches diameter, maximum. This limit is due to the severe cold working required to attain the desired properties. It can be obtained in strip up to four inches wide and a thickness of about 0.130 inches maximum.

(5) 310 Stainless Steel:

This stainless steel can be considered where minimum magnetic permeability is not necessary. Its permeability is approximately $\mu = 1.002$ and in different specification ranges from 1.0012 to 1.003. The permeability varies only slightly with cold working up to 50%.

The biggest uncertainty with 310 is that the permeability is not guaranteed by any specification located so far. One possible alternate is Carpenter No. 10 which has a guaranteed maximum $\mu = 1.005$ from the annealed condition up to 50% cold reduction.

(6) Mallory 1000:

This material has been developed by P. R. Mallory and Company, Inc. Its general characteristics are high density, high strength, nonmagnetic and corrosion resistant.

The data in Table IV were obtained from that table's Ref. (14). It is seen that except for the low thermal coefficient of expansion, which does not match that of aluminum, it is generally an excellent material for end masses.

A word on the magnetic characteristics is in order. P.R. Mallory states that the material is nonmagnetic but they could not even estimate its permeability or susceptibility. Table IV Ref. (15) discusses this Cu(4) - Ni(6) - W(90) alloy in some detail, but fails to mention its

susceptibility. However, P.R. Mallory states that the copper-nickel-tungsten forms a ternary that is Cu(4) - Ni(6) - W(18) in terms of the original composition. The remaining 72 percent tungsten is in the form of rounded grains of pure tungsten embedded in the ternary. There is no porosity and the alloy can be easily and accurately controlled. Table IV Ref. (16) shows that a copper nickel alloy of Cu(40) - Ni(6) has a susceptibility of approximately 2.8×10^{-6} cgs and iron contamination up to 0.15 percent has little effect. There is little reason to suspect that the addition of tungsten to this binary alloy would change its susceptibility or its ability to deactivate small amounts of iron. Thus, we could expect the permeability of Mallory 1000 to be nearly equal to that of pure tungsten.

Qualitative measurements were made on a sample of Mallory 1000 and it was found to have a permeability slightly greater than that of 6061 aluminum. Therefore, the permeability of Mallory 1000 was estimated to be 1.00007, slightly greater than that of pure tungsten.

2. Paramagnetic and Diamagnetic Material Tests

a. Introduction

Obtaining susceptibility or permeability data on paramagnetic and diamagnetic structural material is difficult and time consuming. The relatively few researchers who have the equipment to make such tests are interested in the theoretical aspects of magnetism and not in the permeability of commercial materials. Furthermore even if data is obtained on a commercially available material no one will guarantee the permeability of another similar commercial batch. However a number of commercial materials have very low permeabilities and are suitable for use in sensitive instruments if they are not accidently contaminated. A simple qualitative test for accidental ferromagnetic contamination of low permeability materials was desired.

b. Test Apparatus

A large horeshoe permanent was fitted with pole pieces to provide a gap approximately 0.6 inches long and a cross section near the center of about 0.125 square inches. The magnetic field in this gap was measured and found to be 2,000 oersteds near the center and 3,000 oersteds near the tips of the pole pieces. The average linear field was estimated to be 2,500 oersteds and the effective gradient 2,000 oersteds per centimeter.

Material samples were made 0.5 inches long and 0.125 inches in diameter. These samples were suspended in the magnetic field between the pole pieces by a very thin fiber, about 10 inches long, attached at the center of the sample so that the samples acted as a "compass" needle in the established field.

c. Material Test Results

A number of material samples were prepared and tested in the magnet gap. The speed and direction of the sample reaction to the magnetic field was used to estimate the sample susceptibility.

The following equations are from Subsection B-4, "RGG Torques Due to Paramagnetic Materials." The torque equation is corrected to account for the homogeneous sample.

$$\mu = 1 + 4\pi\chi\rho$$

$$\text{Torque} = \chi\rho \ \text{Vol} \sin\theta \cos\theta \left(H^2 + \frac{\ell^2}{32}\left(\frac{dH}{dx}\right)^2\right)$$

where:

μ = permeability

χ = susceptibility

ρ = density

Vol = volume of the sample, 2.5×10^{-2} cc

θ = the angle the sample makes with the field

H = magnetic field strength, 2500 oersteds

dH/dX = gradient of the field, 2000 oersteds/cm

ℓ = length of the sample, 1.27 cm

The peak torque for the field, gradient and sample size previously given is:

$$\text{Torque} = \chi\rho \times 0.322 \times 10^6 \text{ peak dyne cm}$$

The design susceptibilities and qualitative observations for several materials follow.

Substituting for I and t, k is found to be

$$k = 0.02\ d\ \text{cm/rad}$$

It should be possible to rotate the upper end of the suspension

$$\theta = \frac{T}{k} = \frac{1.65}{0.02} = 82\ \text{rad} = 13\ \text{revs.}$$

But the torques and the revolutions that the suspension can be rotated are not nearly this large.

d. Conclusions

The apparatus can distinguish paramagnetic, diamagnetic and slightly paramagnetic. This is all that is required to identify accidental contamination of material batches.

Material	$\chi \times 10^6$	ρ	Observation
Crown Glass	-0.90	2.47	Slightly diamagnetic
6061 Alum.	+0.63	2.70	Slightly paramagnetic
Be-Cu	-0.63	8.2	[a]Very slightly diamagnetic
Elgiloy	+0.39	8.3	Paramagnetic
310 Stainless	+20	7.9	Strongly paramagnetic
Malloy 1000	+0.33	17.0	Paramagnetic

[a]See following paragraphs

The theoretical peak torque for beryllium copper (Be-Cu) is

$$\text{Torque} = -0.63 \times 8.2 \times 0.322 = -1.65 \text{ dyne cm}$$

When the Be-Cu sample was first tested it would have been classified as "slightly paramagnetic." After etching to remove tool marks it was very slightly diamagnetic. It is not as strongly diamagnetic as the crown glass so it is probably slightly contaminated.

Some idea of the sensitivity of this test can be obtained by calculating the stiffness of the suspension fiber. The period of a torsional pendulum is

$$t = 2\pi\sqrt{I/k}$$

and the measured period was 15 sec. The moment of inertia of the cylindrical sample suspended at its center of gravity is

$$I = \frac{\pi r^2 \rho \ell}{4}\left(r^2 + \ell^2/3\right)$$

$$= 0.115 \text{ gram cm}^2$$

c. Material Test Results

A number of material samples were prepared and tested in the magnet gap. The speed and direction of the sample reaction to the magnetic field was used to estimate the sample susceptibility.

The following equations are from Subsection B-4, "RGG Torques Due to Paramagnetic Materials." The torque equation is corrected to account for the homogeneous sample.

$$\mu = 1 + 4\pi\chi\rho$$

$$\text{Torque} = \chi\rho \ \text{Vol} \sin\theta \cos 0 \left(H^2 + \frac{\ell^2}{32}\left(\frac{dH}{dx}\right)^2\right)$$

where:

μ = permeability

χ = susceptibility

ρ = density

Vol = volume of the sample, 2.5×10^{-2} cc

θ = the angle the sample makes with the field

H = magnetic field strength, 2500 oersteds

dH/dX = gradient of the field, 2000 oersteds/cm

ℓ = length of the sample, 1.27 cm

The peak torque for the field, gradient and sample size previously given is:

$$\text{Torque} = \chi\rho \times 0.322 \times 10^6 \text{ peak dyne cm}$$

The design susceptibilities and qualitative observations for several materials follow.

REFERENCES

1. S.R. Williams, Magnetic Phenomena, McGraw-Hill Book Company, 1931.

2. D.E. Gray, Editor, American Institute of Physics Handbook, Second Edition, McGraw-Hill Book Co., 1963.

3. E. Hallen, Electromagnetic Theory, Chapman & Hill, 1962.

4. L.B. Lobe, Fundamentals of Electricity and Magnetism, John Wiley and Sons, Inc., 1931.

5. Kent R. Van Horn, Editor, Aluminum-Properties, Physical Metallurgy and Phase Diagrams, American Society for Metals, Metals Park, Ohio, 1967.

6. H. Nyquist, "Thermal Agitation of Electrical Change in Conductors," Phys. Rev. V.32, p.110, 1928.

7. H.B. Callen and T.A. Welton, "Irreversibility and Generalized Noise," Phys. Rev. V.83, p.34, 1951.

8. D. Middleton, An Introduction to Statistical Communication Theory p.343, McGraw Hill, 1960.